國立臺灣大學電機資訊學院電子工程學研究所

博士論文

Graduate Institute of Electronics Engineering

College of Electrical Engineering and Computer Science

National Taiwan University

Doctoral Dissertation

壓電換能器之主動減振控制

Active Damping Control of Piezoelectric Transducers

鄭立誠

Li-Chen Cheng

指導教授：陳秋麟 博士

Advisor: Chern-Lin Chen, Ph.D.

中華民國 104 年 6 月

June, 2015

誌謝

謹以此書感謝我的父母、師長、以及求學路上所遇相知相惜之友。

中文摘要

本論文提出一主動減振控制方案，其適用於車用距離偵測系統之壓電換能器。近年來車用電子領域已日益受到重視。壓電換能器為此領域中一種重要的感測器，其利用超音波來偵測車輛周遭的物體以避免可能發生的碰撞。但是壓電換能器的偵測範圍會受到其本身機械振盪衰減速度的限制，故本論文希望藉由引入主動減振控制來提升此感測器振動的衰減速度。

發送超音波的過程包含了對壓電換能器的驅動以及減振。壓電換能器的最佳操作頻率可根據驅動電路的操作由其共振頻率來決定。此外，由於壓電換能器通常具有極高的頻率選擇性且其特性容易因環境變化而改變，使得要持續有效操作壓電換能器在同一頻率有所困難。因此壓電換能器在進行操作前需先行追蹤其共振頻率。

為了實踐所提出的主動減振控制方案，在本論文中製作了數個驅動電路。第一個電路使用方波電壓來驅動壓電換能器以追蹤其串聯共振頻率。第二個電路則是藉由偵測其可達到零電壓切換的頻率區間來追蹤並聯共振頻率。最後主動減振控制被實現於第三個電路中。透過實驗結果可知，藉由使用主動減振控制，壓電換能器振動衰減速率的理論時間常數可由 368.86 μs 改善為 117.37 μs。

關鍵字：壓電換能器；主動減振控制；共振頻率追蹤；電流驅動轉換器；雙向能量傳送。

ABSTRACT

This dissertation proposes an active damping control method for the piezoelectric transducer in a distance measurement system of a vehicle. In recent years, automotive electronics have become more and more popular and important. Among the devices of automotive electronics, the piezoelectric transducer is one of essential sensors. It utilizes ultrasound to detect the objects surrounding a vehicle to prevent possible collision. However, the detectable range of the measurement system with piezoelectric transducer is restricted by the decay rate of its mechanical vibration, and thus the active damping controls are introduced to enhance the decay rate of the vibration.

The process of transmitting ultrasound with active damping controls includes driving and damping a piezoelectric transducer. The optimum operating frequency of a piezoelectric transducer should be determined by the resonant frequencies according to the operation of the driving circuit. Moreover, because a piezoelectric transducer is usually highly frequency-dependent, and its characteristics are easily influenced by the variation of environment, it is difficult to continuously operate a piezoelectric transducer efficiently at a constant frequency. Therefore, the resonant frequencies of the piezoelectric transducer should be tracked before the transmitting process starts.

To realize the proposed active damping controls on a piezoelectric transducer, several prototype driving circuits of the piezoelectric transducer were constructed. The

first circuit drives the piezoelectric transducer with square-wave voltage to track the serial resonance frequency. As for the second circuit, the frequency at which zero-voltage-switch is achieved is detected to track the parallel resonance frequency. Finally, the active damping control is implemented in the third circuit to transmit ultrasound. The experimental results show that the theoretical time constant of the decay rate is improved from 368.86 μs to 117.37 μs with active damping control.

TABLE OF CONTENTS

LIST OF FIGURES

X

LIST OF TABLES

Chapter 1

Introduction

1.1   Background

Automotive electronics are subjects about any electrical systems which are used in road vehicles. They can be applied on various applications. According to different applications, automotive electronics can be classified into different categories including powertrain, safety, convenience, and infotainment. Although the first electrical devices, which are car radios, were equipped in vehicles since the early 1930s, automotive engineers did not put emphasis on electronics until the invention of power transistor in 1950s. The power transistors can be used on electronic ignition system to improve the efficiency of the engine in automobiles. However, this system was not widely adopted because the cost of this new technology was significantly more than the conventional system. Until 1970s, the US government introduced the regulation of emission control because of the heavily air pollution produced by vehicles. Since that time, electronics for engine controls has been regarded as an adequate solution to reduce the emission of the pollutants from vehicles, and the related techniques were rapidly developed [1], [2]. In recent years, automotive electronics have become more and more popular due to the yield improvement and cost reduction of related semiconductor manufacturing. It is estimated that the total global market volume for automotive electronics has risen to

USD 205 billion in 2014, and this market may reach USD 314 billion by the year 2020. The value share of electronic in a vehicle also increases steadily. It has occupied 30% of total vehicle cost on average in 2011, and the figure may increase to over 40% in the near future [3], [4].

Sensors are essential components in automotive electronics. They can function as inputs in a control system to convert the environmental information into electrical signals. Distance sensors are one type among them. Such sensors can monitor the environment outside the vehicle to prevent dangerous collisions with obstacles or other vehicles. There are two categories of distance sensors: long-range distance sensors, which mainly watch the area forward the vehicle at a distance within the range of 30 to 100 m, and short-range distance, sensors which detect the area all directions around the vehicle at the distance within 30 m. Long-range distance sensors are usually applied on adaptive cruise control system and forward collision warning. On the other hand, short-range distance sensors are usually applied on blind spot detection, lane departure warning, collision warning with pre-impact brake assistance, backup obstacle detection, and parking assistance [5], [6].

1.2   Ultrasonic Distance Measurement System

Ultrasonic sensors are one of the widely adopted short-range distance sensors. The
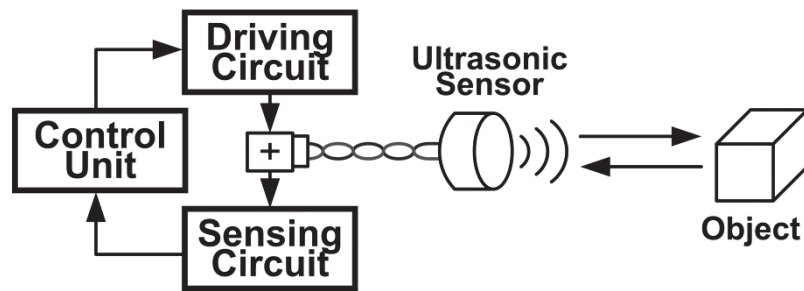
Fig. 1.1. Configuration of an ultrasonic distance measurement system.

operating frequency of ultrasonic sensors is usually around 50 kHz, and the effective

detectable range of ultrasonic sensors is about 2.5 m. Because ultrasonic sensors utilize

ultrasound, which is a type of mechanical wave, to detect the environment, the

measurement of ultrasonic sensors is easily influenced by bad weather condition and

high-speed wind. Nevertheless, they have the advantage of low price and wide

horizontal aperture comparing to other short-range distance sensors. Thus, ultrasonic

sensors are widely applied on the systems which should detect large area around a

vehicle such like backup obstacle detection and parking assistance.

The configuration of the ultrasonic distance measurement system is shown in Fig.

1.1. It contains four parts: ultrasonic sensor, driving circuit, sensing circuit, and control

unit. The distance measurement process is usually as follows: First, the control unit

transmits signals to the driving circuit, and the driving circuit will convert these signals

into high-voltage alternating current (AC) waveform to drive the ultrasonic sensor.

Second, the ultrasonic sensor will work as a transmitter to generate a sequence of

ultrasound waves. Third, after the ultrasonic sensor works as a receiver to sense the

reflecting waves, the sensing circuit will amplify the reflecting signals and will trigger the control unit. Finally, the control unit calculates the period of time between transmitted and received signals. Then, the distance of the object can then be known.

Ultrasonic sensors are generally made of piezoelectric material, which can transfer electrical energy into mechanical energy, and vice versa. They are also called piezoelectric transducers. Whether devices are called "ultrasonic sensors" or "piezoelectric transducers" depends on the field of applications. In the following of this dissertation, we will call it piezoelectric transducers (PTs) to prevent from possible confusions.

1.3   Motivations and Objectives

In a distance measurement system, a transmitter is needed to generate ultrasound, and a receiver is needed to detect the reflected waves. They can be either two independent PTs or a single PT. Because of the inertia of the mechanical resonator in the PT, it cannot stop vibrating as soon as the driving circuit stops operating. If we use a single PT in a distance measurement system, this PT should take a period of reverberation time for V_{PT} to decay. In this reverberation time, the PT cannot sense the reflecting ultrasound. The voltage waveform crossing the PT in the measurement process is displayed in Fig. 1.2. Thus, the minimum detectable range of the system

4
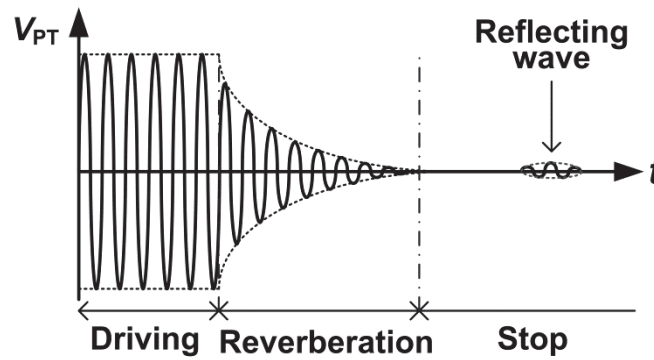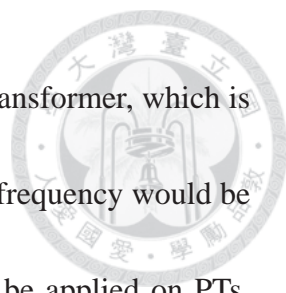
Fig. 1.2. Voltage waveform of a piezoelectric transducer as a transceiver in distance measurement system.

would be restricted. If the decay rate of V_{PT} could be faster, the minimum detectable range may be improved.
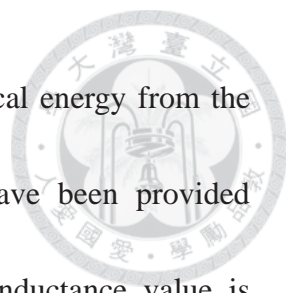
How to drive the PT efficiently is another important issue. The high quality factor of piezoelectric materials is usually high. Thus, a PT should be operated at its resonant frequency for higher transmitting gain. However, the characteristics of a PT would easily change with environmental variation. Therefore, the resonant frequency of a PT should be tracked before transmitting the ultrasound. Moreover, because of the input capacitance of a PT, a lot of reactive power should be supplied by the power source when transmitting ultrasound. This reactive power may be dissipated on power transistors and the PT. As a result, heat sinks are needed for transistors in the driving circuit and characteristics of the PT may change due to temperature rise.

In previous researches, many tracking methods based on phase difference detection have been developed. One method is to track the frequency with zero phase difference

between the input voltage and the output current of a piezoelectric transformer, which is

a piezoelectric device for converting electrical energy [7]-[10]. This frequency would be

very close to the resonance frequency whereas this method cannot be applied on PTs,

which do not have secondary side in electrical domain. Another method is to track the

frequency with zero phase difference between the input voltage and the input current

[11]-[15]. The phase difference should approach zero at both the resonance frequency

and the anti-resonance frequency of a PT. However, this condition is not always

satisfied because the value of the input capacitance might be so large that the input

impedance of a PT only shows capacitive reactance. A frequency-dependent

compensation in the feedback loop is required for preventing the tracking process from

locking at another resonance frequency [15]. To compensate for the capacitive behavior

of the PT, additional reactive components are connected [7]-[11], [13]-[16]. Moreover,

some soft-switch technologies have also been developed to reduce the power losses on

transistors [10], [12]-[14]. Nevertheless, additional components should be highly

dependent on characteristic frequencies of the PT, and tracking the operating frequency

from phase detection might become difficult due to additional harmonic currents

introduced by additional components.

Piezoelectric transducers could be used as an energy source to collect mechanical

energy from the environment. They have been widely used on structure active damping

[17]-[20] and energy harvesting [21]-[32]. To transfer more electrical energy from the PTs, non-linear techniques about synchronized switch control have been provided [17]-[32]. In these techniques, an external inductor with small inductance value is connected to resonate with the PT in a way synchronous with the vibration. One of these techniques is called synchronous electrical charge extraction (SECE). The other technique is called synchronized switching damping on inductor (SSDI). By applying these techniques, the decay rate of the vibration of the PT can be improved. Moreover, the inverse approach of these non-linear techniques could also be used to drive PTs and such a technique has been developed in [33].

In this dissertation, a novel control method for driving circuits of PTs is developed to automatically track the resonant frequency and to transmit ultrasound with active damping. Conventionally, a phase detector is needed to realize active damping control since the receiving mechanical waves are arbitrary. However, if the PT could be driven in a designed waveform and could operate at its resonance frequency, the phase of the mechanical vibration might be predicted. Therefore, the active damping can be achieved without any extra sensing circuits. Moreover, the proposed control method can track the resonance frequency with soft-switch techniques, which means both the efficiency of the driving circuit and the transmitting gain of the PT can be improved. The fundamental theories of the proposed control method will be presented, and the

operation of the experimental circuits will be explained in the following of this dissertation.

1.4 Dissertation Organization

The remaining chapters of the dissertation are organized as follows. Chapter 2 reviews characteristics of PTs in electrical domain and explains the role of PTs in a distance measurement system in the view of its electrical characteristics. Chapter 3 presents conventional damping controls including the effectiveness of passive damping and the operating process of active damping in the previous researches. Chapter 4 shows the phase relationship between the driving waveform and the oscillation of the PT in different driving methods. After that, various circuit implementations and their experimental results of the proposed control will be provided in chapter 5, chapter 6, and chapter 7. In Chapter 5, a compensation method for the input capacitance of the PT to track the resonant frequency is shown. Chapter 6 develops a resonance-frequency-tracking method which utilizes the frequency dependence of a resonant converter. Then, the driving circuits with active damping control will be realized in chapter 7, and the effectiveness of the active damping control will be discussed. Finally, chapter 8 provides a conclusion of the proposed control method.

Chapter 2

Piezoelectric Transducer

The piezoelectric transducer is an important component in ultrasonic systems. The operating principle of a PT includes different areas of knowledge. Hence, the basic characteristics of the PT should be understood for proper utilization. These characteristics will be introduced in this chapter.

2.1   Piezoelectricity

Piezoelectricity is a phenomenon that mechanical energy and electrical energy can convert to each other via some materials. The word "piezoelectricity", which was proposed by Hankel in 1881, means "electricity and pressure" to name the phenomenon observed by Curies brothers in 1880. They found that electrical charges appeared on the surface of the crystal when mechanical stresses were applied. After their discovery, Lippmann predicted the reverse piezoelectric effect from fundamental thermodynamic principles. The reverse effect was confirmed by Curies [34], [35]. However, the first application of piezoelectricity, which is a quartz oscillator, did not emerge until early 1920. Nowadays, piezoelectricity has been applied on many applications. For example, piezoelectric transformers, which are devices to realize energy conversion, can be found in many power supply circuits in liquid-crystal displays and can function as backlight
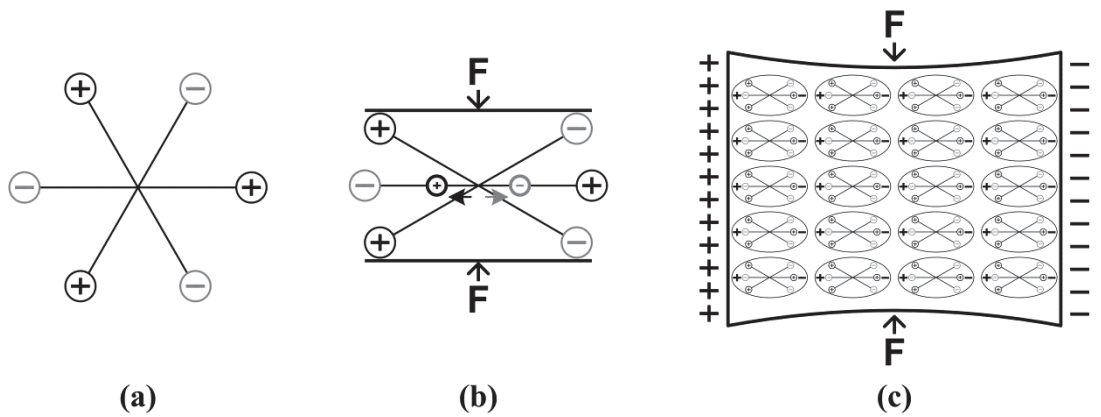
Fig. 2.1. Piezoelectric Effect. (a) Simple molecule model. (b) Molecule with pressure.

(c) Material with pressure.

ballasts. In addition, piezoelectric transducers, which can generate ultrasound from

electrical energy, have been applied in ultrasonic cleaning devices and distance

measurement systems.

The fundamental theory of piezoelectric effect is shown in Fig. 2.1. Fig 2.1(a) is a

simple model of a molecule. In this molecule, the gravity centers of the positive charges

and the negative charges are both located at the same point. Therefore, the electrical

effects of the positive and negative charges outside the molecule can be mutually

cancelled, and the molecule is electrical neutral. However, when a stress is applied on

the molecular, its structure may be deformed. As a result, the gravity centers of the

positive charges and the negative charges separates and generates little dipoles on the

molecule in Fig. 2.1(b). The material with these molecules is shown in Fig. 2.1(c). The

electrical dipoles inside the material cancel each other, and the density of the charges
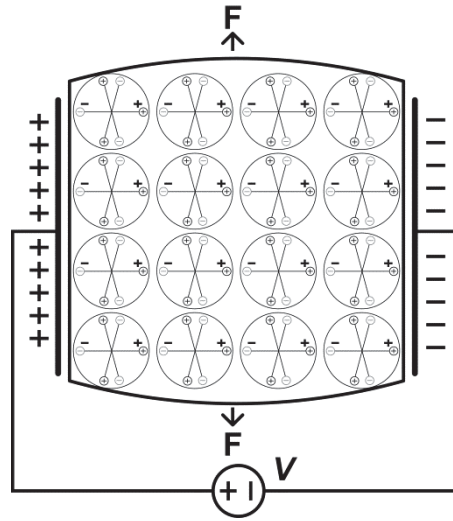
Fig. 2.2. Reverse piezoelectric effect.

increase on the surface of the material. In other word, the material is polarized and an

electrical field is generated [35]. On the other hand, the reverse piezoelectric effect can

be explained in the same manner. When a voltage is applied on a piezoelectric material,

a mechanical deformation will be produced. This phenomenon is presented in Fig. 2.2.

2.2 Equivalent Circuit

The piezoelectric transducer can be simply modeled as the equivalent circuit which

is shown in Fig. 2.3 near its resonance frequency [36]. The transformer in Fig. 2.3(a)

emulates the energy coupled between electrical and mechanical domains. The

components in the mechanical domain can be reflected to the electrical domain. Then,

the other model is got in Fig. 2.3(b). It consists of two parallel branches: one is the

parallel capacitor C_0. The other is the serially connected R_1-L_1-C_1 circuits. Because a PT
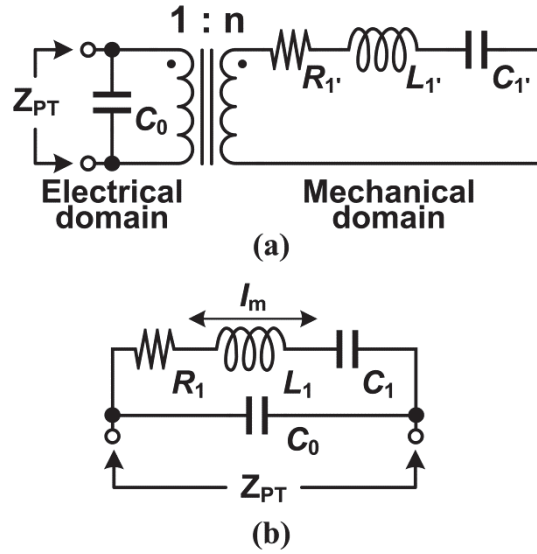
Fig. 2.3. Equivalent circuit of a PT. (a) Original simple version. (b) Reflected version.

is composed with piezoelectric materials and dielectric materials, these dielectric materials constitute a static capacitance between the two metal electrode plates of the PT. The behavior of this static capacitance can be represented by the capacitor C_0, and the R_1-L_1-C_1 branch can show the mechanical resonator of a PT [35]. Moreover, the sound pressure level of ultrasound generated by the PT is proportional to the mechanical current I_m which flows through the R_1-L_1-C_1 circuit.

A piezoelectric transducer could have many resonance modes according to different vibration behaviors. The vibrations of these modes, which can include flexural mode, length mode, expansion mode, and shear mode, are illustrated in Fig. 2.4. All of them and their harmonics can be modeled by an independent R-L-C circuit to represent their vibrations. Therefore, a more complete equivalent circuit of a PT should be like the one in Fig 2.5. However, a PT would usually be designed to have only one main
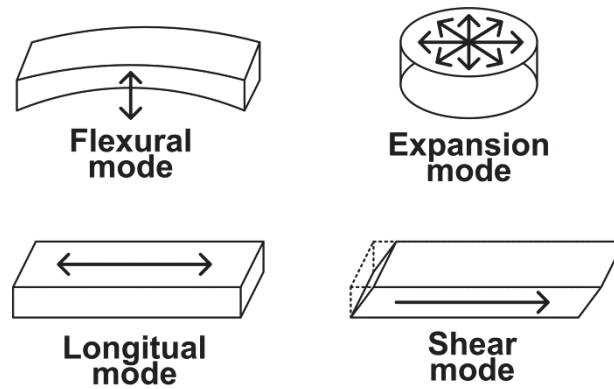
Fig. 2.4. Different vibration modes.
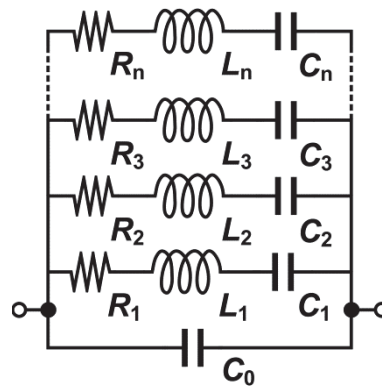
Fig. 2.5. Equivalent circuit with different resonant modes.

resonance mode, which means the quality factor of the main resonant mode would be much larger than others. Hence, the influences from other resonant modes can be ignored, and the analysis for the circuit with a PT can directly replace the PT with the equivalent circuit in Fig 2.3(b).

2.3   Resonance Frequencies

Resonance means a system have a tendency to oscillate with larger amplitude at some particular frequencies. These frequencies are called resonance frequencies or
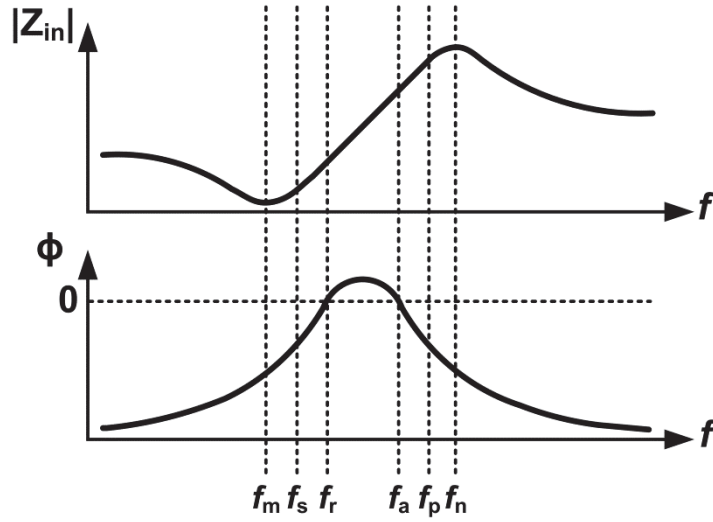
Fig. 2.6. Bode plot of the PT.

resonant frequencies. At these frequencies, the energy in the system can be easily transferred between two different storage modes. A PT has several resonance frequencies. Two of them are the series resonance frequency f_s and the parallel resonance frequency f_p. Their values could be directly known from the equivalent circuit of the PT, which are

$$f_s = \frac{1}{2\pi\sqrt{L_1 C_1}}, \quad f_p = \frac{1}{2\pi}\sqrt{\frac{C_0 + C_1}{L_1 C_0 C_1}} \tag{2.1}$$

The frequency f_s is the frequency with maximum conductance, and f_p is the frequency with maximum resistance.

From the Bode plot of the PT shown in Fig. 2.6, the other four resonance frequencies can be identified, they are the frequency with maximum admitance f_m, the frequency with zero susceptance f_r, the frequency with zero reactance f_a, and the
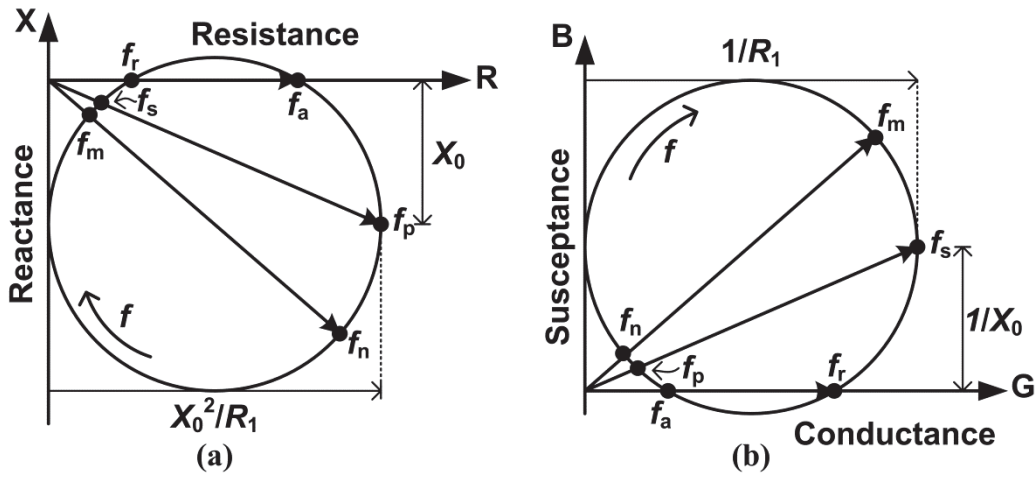
Fig. 2.7. Circle of (a) impedance. (b) admittance.

frequency with maximum impedance f_n. The impedance and the admittance cycles of

the PT are drawn in Fig 2.7. If the mechanical resonator of the PT is lossless, which

means the value of R_1 is zero, the diameter of the cycles in Fig 2.7 would be infinity.

Therefore, the frequencies f_m, f_s, f_r will be the same frequency called resonance

frequency of the PT. Likewise, the frequencies f_n, f_p, f_a will also be the same frequency

called anti-resonance frequency.

To understand the differences among these three resonance frequencies, the driving

source of the PT should also be considered. Assume that the driving source is an AC

voltage source with constant amplitude. Operating at f_s can achieve largest value of

mechanical current I_m because it is the frequency with maximum conductance.

Additionally, operating at f_r can get maximum efficiency for the driving source because

the PT is zero susceptance at f_r. Furthermore, operating at f_r can cause largest energy

transfer between the driving source and the PT. Similar relationship can be find between

15
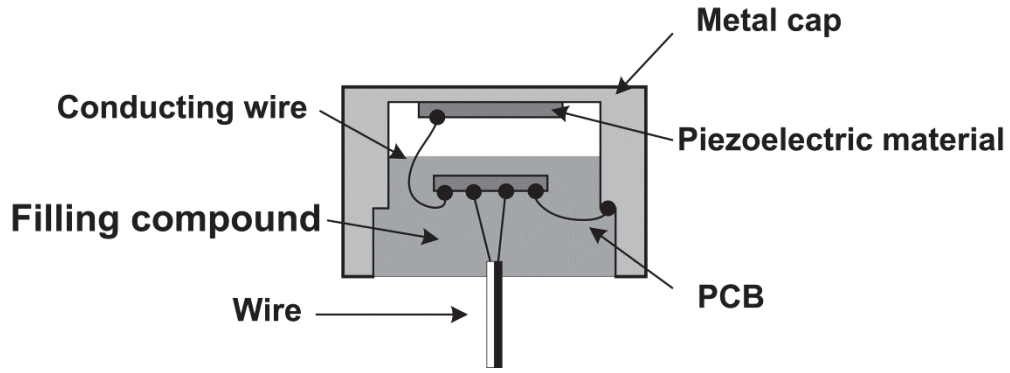
Fig. 2.8. Structure of a PT.

an AC current source and the three anti-resonance frequencies.

The energy transferred in a PT cannot be described only by the mechanical resonator because of the existence of C_0. Thus, the energy conversion will be associated with the relationship between the values of f_s and f_p. According to IEEE standard of piezoelectricity [37], the figure of merit M for the PT has been defined as

$$M = \frac{k_{eff}^2 Q}{1 - k_{eff}^2} \qquad (2.2)$$

where

$$k_{eff}^2 = \frac{f_p^2 - f_s^2}{f_p^2}, \qquad Q = \frac{1}{R_1}\sqrt{\frac{L_1}{C_1}}. \qquad (2.3)$$

The quantity k_{eff} is the effective coupling coefficient to shown the difference between f_s and f_p, and the quantity Q is the quality factor of the mechanical resonator.

2.4 Application in an Ultrasonic Measurement System

The structure of the PT in this dissertation is illustrated in Fig. 2.8. It is enclosed by
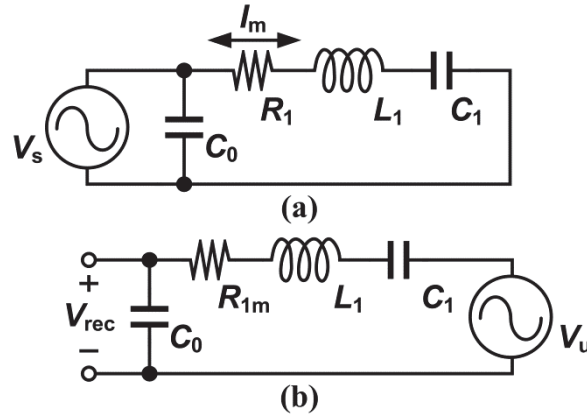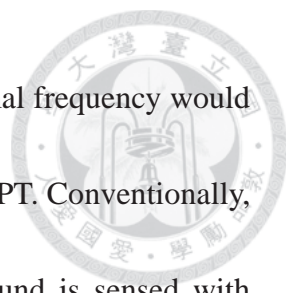
Fig. 2.9. Configuration of a PT as (a) a transmitter. (b) a receiver.

a metal cap to protect the piezoelectric material from water droplets and dust. Moreover, the metal cap is usually connected to ground to prevent EMI issues. This PT can work as a transmitter or a receiver in an ultrasonic distance measurement system.

If a PT is operated as a transceiver, the frequency with maximum transmitting gain may not be the same frequency with maximum receiving gain. When a PT is used as a transmitter, the configuration is showed in Fig. 2.9(a). Where the optimal operating frequency locates would depend on the AC driving source. If the driving source is a voltage source, the optimal operating frequency would be f_s. In contrast, if the driving source is a current source, the optimal operating frequency would be f_p. Furthermore, when a PT is used as a receiver, the configuration is a second-order passive filter showed in Fig. 2.9(b) [38]. The reflecting ultrasound signal could be model as a voltage source V_u which is serial connected with R_1-L_1-C_1 branch. Hence, the frequency with the optimal receiving gain would locate at f_p if the sensing circuit detects the voltage

crossing the PT as the reflecting signal. On the other hand, the optimal frequency would

locate at f_s if the sensing circuit detects the current flowing from the PT. Conventionally,

the PT is driven with a voltage source, and the reflecting ultrasound is sensed with

voltage signal. Thus, the frequency with maximum transmitting gain would be different

from the frequency with maximum receiving gain. As a result, the frequency of the

transmitting ultrasound usually falls between f_s and f_p to get maximum receiving voltage

in a conventional measurement system.

Chapter 3

Conventional Damping Controls

Damping controls in a PT can be classified into two groups which are passive and active damping. Passive damping refers to the energy dissipating process only caused by resistive components. In this chapter, the discussion about passive damping only includes the components in the equivalent circuit of the PT, and the passive damping involved in other additional shunt components is not discussed. Additionally, active damping is realized with active components, which are usually power transistors or operational amplifiers, to increase the damping effect of the vibration. One of the control methods of active damping is synchronized switch techniques. This chapter will describe the principles and the theoretical effectiveness of active damping control applied synchronized switch techniques.

3.1 Passive damping

Passive damping in the PT is achieved by viscous effect, which is shown as a resistor in the equivalent circuit. Because this damping control is not disturbed by components outside the PT, the PT would oscillate at its natural frequency, which is approximately equal to the resonant frequency. There are two types of oscillation: One
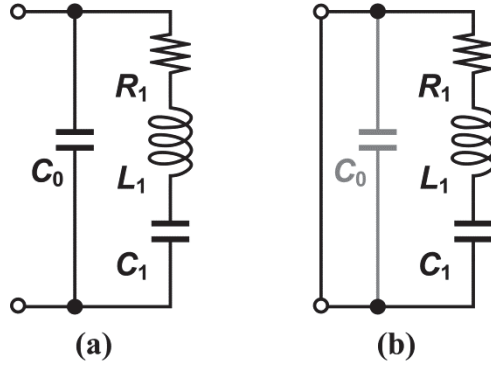
Fig. 3.1 Configuration of PT. (a) Open-circuit. (b) Short-circuit.

is open-circuited, and the other is short-circuited. The configurations are illustrated in

Fig. 3.1. The analysis of passive damping control is as follows.

Assume that the initial value of I_m is I_{max}, and that the driving circuit stops driving

the PT at $t = 0$. In addition, the PT is in open-circuited configuration. Then, from the

circuit shown in Fig. 3.1(a), the laplace transform of I_m in the PT would be

$$I_m(s) = \frac{L_1 i_{max}}{R_1 + sL_1 + \frac{1}{sC_{eff}}} = \frac{i_{max}s}{s^2 + s\frac{R_1}{L_1} + \frac{1}{L_1 C_{eff}}}$$

$$= \frac{i_{max}(s + \frac{R_1}{2L_1}) - i_{max}\frac{R_1}{2L_1}}{(s + \frac{R_1}{2L_1})^2 + (\frac{1}{L_1 C_{eff}} - \frac{R_1^2}{4L_1^2})}$$

(3.1)

where $C_{eff} = C_0 C_1/(C_0+C_1)$. Thus, the inverse laplace transform of (3.1) would be

$$i_m(t) = i_{max}e^{-\frac{R_1}{2L_1}t}\cos\omega_o t - i_{max}\frac{R_1}{2L_1\omega_o}e^{-\frac{R_1}{2L_1}t}\sin\omega_o t$$

$$\cong i_{max}e^{-\frac{R_1}{2L_1}t}\cos\omega_o t$$

(3.2)

where

$$\omega_o = \sqrt{\frac{1}{L_1 C_{eff}} - \frac{R_1{}^2}{4L_1{}^2}} \cong \frac{1}{\sqrt{L_1 C_{eff}}} = \sqrt{\frac{C_0 + C_1}{L_1 C_0 C_1}}, \tag{3.3}$$

which is the same frequency of f_p. Furthermore, the time constant of the passive damping in the open-circuited configuration would be

$$\tau_{passive} = \frac{2L_1}{R_1}. \tag{3.4}$$

The time constant in the short-circuited configuration is the same as (3.4). The difference between the short-circuited and the open-circuited configurations is whether the capacitor C_0 joins the oscillation of I_m. If C_{eff} is replaced by C_0 in (3.1)-(3.4), the analysis for the short-circuited configuration could be got. The difference between these two passive damping controls is the value of the natural frequency ω_0. The natural frequency of short-circuited configuration is approximate to f_s whereas the one of open-circuited configuration is near f_p. Therefore, the effectiveness of the passive damping control in a PT can be described by the time constant shown in (3.4).

3.2　Active Damping

Active damping control in a PT aims to extract energy from the PT by some external active components. Then, the decay rate of the mechanical vibration of the PT can be enhanced. The extracted energy can be consumed by resistive components or can be transferred to storage devices. Consequently, the researches of active damping

controls could often relate to energy harvesting, which is a research topic about acquiring energy from the environment. Among the proposed techniques of active damping and energy harvesting, synchronized switch control is the most popular one. This technique has several sub-categories. They will be described in the following section.

3.2.1 Synchronized Switch Damping on Inductor (SSDI)

In the technique of SSDI, an inductor is used to reverse the polarity of electric charge on the parallel capacitor C_0 when the direction of the mechanical current I_m of the PT is changed. This technique is also called synchronized switch harvesting on inductor (SSHI) in the applications of energy harvesting. Because the operations of these two techniques are very similar, this section will first describe the operating principles of SSHI.

The purposes of applying SSHI for energy harvesting applications are to acquire more energy from C_0 and to overcome the voltage difference between the PT and the energy reservoir. There are two types of SSHI, which are the serial-SSHI and the parallel-SSHI. The configuration of the former is shown in Fig. 3.2(a), and the one of the latter is shown in Fig. 3.2(b). The mechanical resonator of the PT is model as an AC current source I_{ms} in Fig. 3.2 to represent the energy converted from the environments.
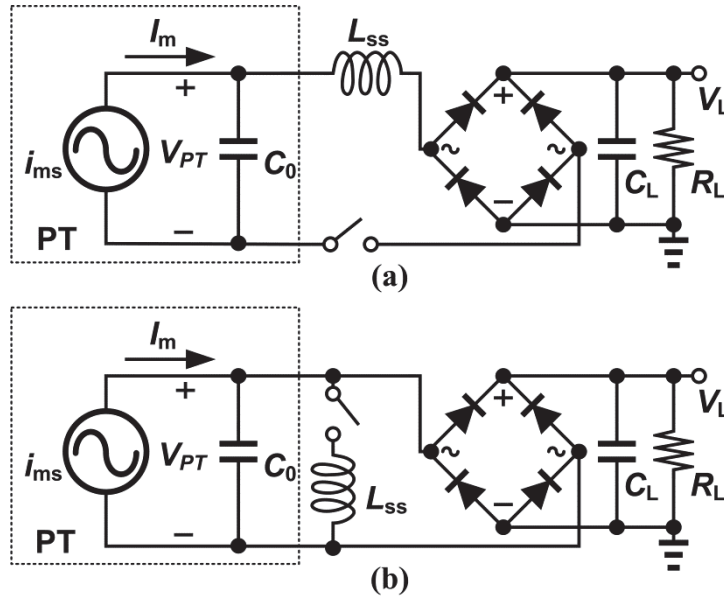
Fig. 3.2. Configurations of (a) serial-SSHI. (b) parallel-SSHI.

For the serial configuration, the PT is in open-circuited condition in most of the cycle.

Thus, the energy stored in C_0 per cycle can be shown by

$$E_{C_0} = \int_T^{T-1} I_m(t)V_{C_0}(t)dt \tag{3.5}$$

where T is the period of one cycle. Assume that the amplitude of I_m is independent to

V_{C0}. Then, the higher the value of V_{C0}, the higher the energy can be stored in C_0. Thus,

more energy can be acquired with the serial-SSHI than the conventional configuration

in which the PT is directly connected to the rectifier, and this energy will be transferred

to the energy reservoir by the resonance between C_0 and L_{ss}. In contrast to the serial

configuration, the PT in the parallel configuration is connected to the reservoir through

the rectifier in the whole cycle. The voltage of C_0 will be reversed in polarity by the

resonance between C_0 and L_{ss} whenever the direction of I_s is changed. As a result, the

23
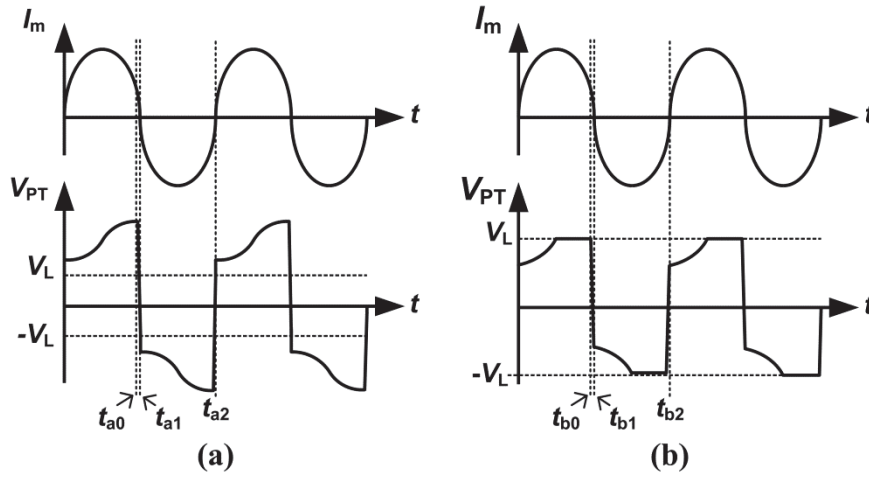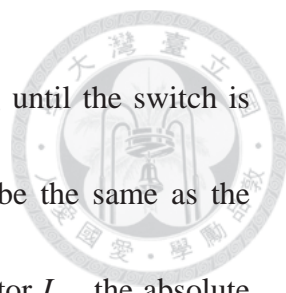
Fig. 3.3. Ideal waveform of (a) serial-SSHI. (b) parallel-SSHI.

voltage crossing the PT can be larger than the voltage of the reservoir for most of the

cycle, and the conducting time of the rectifier can be maximized to transfer more energy

than the conventional energy harvesting circuit.

The ideal operating waveforms of the serial-SSHI in Fig. 3.2(a) and the

parallel-SSHI in Fig. 3.2(b) are respectively illustrated in Fig. 3.3(a) and 3.3(b). For the

serial-SSHI, the switch turns on when the voltage crossing the PT, V_{PT}, is the maximum

value at t = t_{a0}, and the resonance between L_{ss} and C_0 begins. When V_{PT} is reversed in

polarity at t = t_{a1}, the switch will be turned off, and the resonance is stopped. Thus, the

resonance time T_r should be half of the resonant period between L_s and C_0, which is

$$T_r = t_{a1} - t_{a0} = \frac{1}{4\pi\sqrt{L_{ss}C_0}}. \tag{3.6}$$

After t = t_{a1}, I_m flows into C_0, and V_{PT} increases until the next maximum value. Then,

the next half cycle starts at t = t_{a2}. For the parallel-SSHI, the switch is closed at t = t_{b0}

24

when the direction of I_m is altered. Then, C_0 will resonate with L_{ss} until the switch is turned off at t = t_{b1}. The period of time between t_{b0} and t_{b1} will be the same as the resonance time shown in (3.6). Due to the non-ideality of the inductor L_{ss}, the absolute value of V_{PT} at t_{b1} will be smaller than the value at t_{b0}. Hence, deadtime may exist from t_{b1} to t_{b2}. After t = t_{b2}, V_{PT} is higher than the voltage of the energy reservoir, and the rectifier conducts until the next cycle begins. Moreover, the resonance time in both the serial-SSHI and the parallel-SSHI should be minimized because the resonance begins when the direction I_m is changes. The energy in C_0 will transfer not only to L_{ss} but to the mechanical current source I_{ms} before the polarity of the voltage on C_0 is modified. Therefore, the period in (3.6) should be much smaller than the frequency of I_m to avoid this unwanted energy flow. This criterion can also be used to determine the inductance value of L_{ss}.

The operation of SSDI is similar to SSHI. However, the main purpose of active damping control is not to harvest energy but to reduce the amplitude of vibration. Moreover, assume that the PT will not receive any force in the applications of active damping control. Thus, the model of the PT in SSDI would be the same as the structure in Fig. 2.3. Because the energy reservoir cannot absorb the energy stored in C_0 when the local maximum value of V_{PT} is lower than the voltage level of the reservoir, the energy should be consumed by a resistive component in SSDI. The conventional configuration
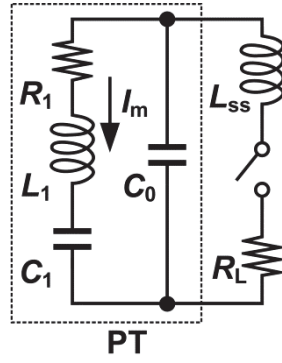
Fig. 3.4. Configuration of SSDI.
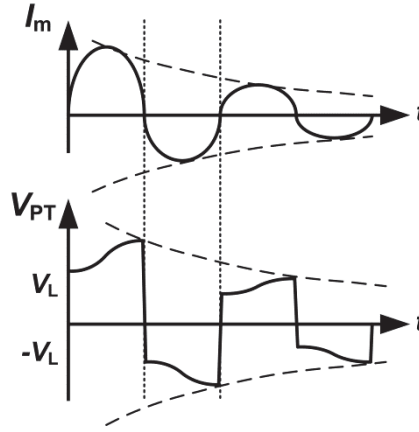
Fig. 3.5. Ideal waveform of SSDI.

of SSDI is shown in Fig. 3.4, and the operating waveform of the SSDI is illustrated in

Fig. 3.5. The inductor L_{ss} is connected to the PT to reverse the polarity of C_0 for a

limited short time when V_{PT} locates at the local maximum value. Hence, the structure in

Fig. 3.4 will be in open-circuited condition for the whole cycle. In addition, the

operation of SSDI only occurred when I_m is zero. Therefore, the phase of I_m would not

be disturbed by the operation. As a result, the operating frequency in SSDI is

approximate the parallel resonance frequency f_s of the PT, and the amplitude of I_m will

decay exponentially.

3.2.2 Synchronized Electrical Charge Extraction (SECE)

The SECE is an active damping control method which is independent to the electric load. In SECE, the electric charges in C_0 will be totally transferred to the reservoir or the load when the voltage crossing the PT reaches maximum value, and the voltage of C_0 will decrease to zero. Because the electric load will not affect the process in which the energy is transferred from the PT, the operations of the SECE method in active damping control and in energy harvesting are identical. Thus, only the operation of active damping will be described.

To realize SECE on a PT, several configurations can be used to discharge C_0. Assume that the mechanical force is not applied on the PT. Fig. 3.6(a) is one of the configurations, which is a PT with a flyback converter. The flyback transformer can work as the resonant inductor to transfer the energy from the C_0 to the electric load in the secondary side. The electric load can be a DC voltage source or a resistor because the output voltage of a flyback converter can be either higher or lower than the input voltage. Another configuration is presented in Fig. 3.6(b), which is a resonant inductor L_{ss} with a switch. This switch will be opened when the current on L_{ss} is at maximum value and the voltage of C_0 is zero. Then, the switch will function as a large resistance to consume the energy in L_{ss}. Fig. 3.6(c) is the other configuration, which is a switch connected to the PT. The voltage of C_0 can be discharged to zero through the
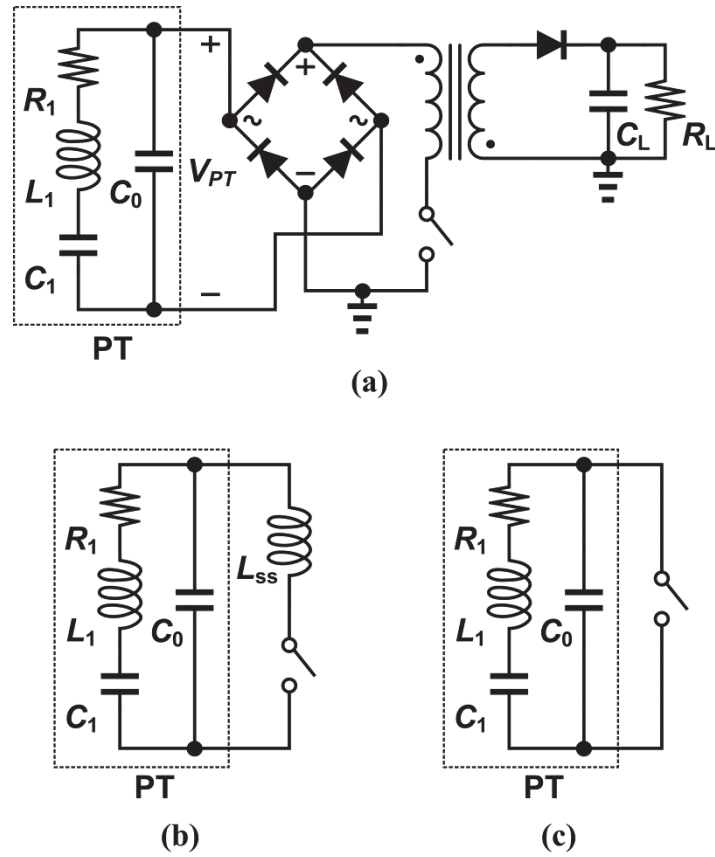
Fig 3.6. Different configurations of SECE. (a) Flyback converter. (b) Switch with an inductor. (c) Discharge through the short-circuited path.

short-circuited path when the switch is turned on.

The operating waveforms of the SECE method are shown in Fig. 3.7. At $t = t_{c0}$, the switch in Fig. 3.6 is turned on. The energy in C_0 starts to transfer to the flyback transformer in Fig. 3.6(a) and the inductor in Fig. 3.6(b). Furthermore, C_0 will be discharged through the short-circuited path in Fig. 3.6(c). The switch will be turned off at $t = t_{c1}$ when the current in the inductive component reaches maximum value or the voltage of C_0 is zero. The flyback transformer in Fig. 3.6(a) will discharge to the secondary side, and the inductor in Fig 3.6(b) will be demagnetized by the spike voltage

28
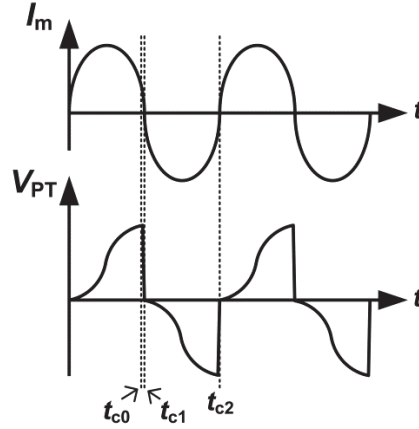
Fig. 3.7. Operating waveforms of SECE.

occurred on the switch. Then, V_{PT} will rise until t = t_{c2}, and the next cycle begins. If C_0

is discharged by an inductive component, the period when the switch is closed should

be

$$t_{c1} - t_{c0} = \frac{1}{8\pi\sqrt{L_{ss}C_0}},$$ (3.7)

which is one-fourth of the period of the resonant frequency between C_0 and the

inductive component. Then, the energy stored in C_0 could be totally transferred or be

consumed. Moreover, if C_0 is discharged by short-circuited condition, the time constant

of this process would be

$$\tau_{R_{on}C_0} = R_{on}C_0$$ (3.8)

where R_{on} is the turn-on resistor of the switch. Like the SSDI method, both of the value

in (3.7) and (3.8) should be minimized comparing to the frequency of I_m to extract

maximum energy from PT. If this criterion is achieved, the oscillating frequency of I_m

will be the parallel resonance frequency of the PT, and the decay curve of I_m will be an

exponential curve.

Chapter 4

Theoretical Analysis on Driving Methods
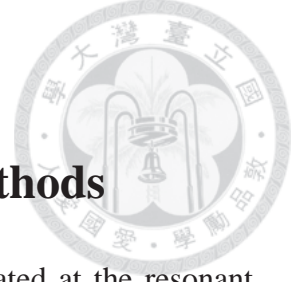
Because of the high quality factor of a PT, it should be operated at the resonant frequency to get the maximum transmitting gain of ultrasound. However, the resonant frequencies of a PT could be divided into two groups. One is called resonance frequency, and the other is called anti-resonance frequency. The resonant state of the PT at these two resonant frequencies may be quite different from each other if the coupling coefficient of the PT is high. Operating at which resonant frequency can get the maximum transmitting gain may depend on the driving source of the PT. Therefore, the relationship between the driving sources and the PT will be presented in this chapter.

4.1 Driving with an Ideal AC Source

The analysis starts from ideal sinusoidal driving sources. The symbols used in the analysis of this section are identified in Fig. 4.1.

4.1.1 Ideal Sinusoidal Current Waveform

Assume that the driver is an ideal sinusoidal current source. Then, the PT will be open-circuited when it is driven. The transfer function $H_i(\omega)$ between the input current I_{in} and the mechanical current I_m can be derived as
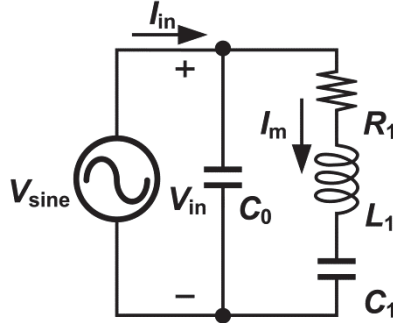
Fig. 4.1. PT with a sinusoidal driving source.

$$H_i(\omega) = \frac{I_m}{I_{in}} = \frac{1}{L_1 C_0} \cdot \frac{1}{j\omega \frac{R_1}{L_1} + \left(\frac{C_1 + C_0}{L_1 C_1 C_0} - \omega^2\right)} \tag{4.1}$$

which can be rewritten as

$$H_i(f) = \frac{\alpha_i}{j\frac{f}{Q_p f_p} + (1 - \frac{f^2}{f_p^2})} \tag{4.2}$$

where

$$Q_p = \frac{1}{R_1}\sqrt{\frac{L_1}{C_{eff}}}, \qquad f_p = \frac{1}{2\pi\sqrt{L_1 C_{eff}}}, \tag{4.3}$$

$$C_{eff} = \frac{C_0 C_1}{C_0 + C_1}, \qquad \alpha_i = \frac{1}{4\pi^2 L_1 C_0 f_p^2}$$

and the phase Φ_i of $H_i(f)$ is

$$\phi_i = -tan^{-1}\frac{f/f_p}{Q_p\left(1 - \frac{f^2}{f_p^2}\right)} \quad \text{for } f \leq f_p$$

$$= -\pi + tan^{-1}\frac{f/f_p}{Q_p(1 - \frac{f^2}{f_p^2})} \quad \text{for } f > f_p. \tag{4.4}$$

From (4.4), the phase of I_m will lag I_{in} with $\pi/2$ when the PT is driven at the parallel

resonance frequency f_p with a sinusoidal current waveform. Furthermore, according to

(4.1), the amplitude of I_m could have maximum gain at f_p. Therefore, the energy

32

transferred between the mechanical domain and the electrical domain could have

maximum efficiency when the driver operates at f_p.

4.1.2　Ideal Sinusoidal Voltage Waveform

On the other hand, assume that the driver is an ideal sinusoidal voltage source. The

PT will be short-circuited, which means that the influence of the parallel capacitance C_0

in Fig. 4.1 can be ignored when it is driven. Then, the transfer function $H_v(\omega)$ between

the input voltage V_{in} and the mechanical current I_m will be

$$H_v(\omega) = \frac{I_m}{V_{in}} = \frac{1}{L_1} \cdot \frac{1}{j\omega \frac{R_1}{L_1} + \left(\frac{1}{L_1 C_1} - \omega^2\right)},\tag{4.5}$$

which can be represented as

$$H_v(f) = \frac{j\alpha_v \cdot f/f_s}{j\frac{f}{Q_s f_s} + (1 - \frac{f^2}{f_s^2})}\tag{4.6}$$

where

$$Q_s = \frac{1}{R_1}\sqrt{\frac{L_1}{C_1}}, \qquad f_s = \frac{1}{2\pi\sqrt{L_1 C_1}}, \qquad \alpha_v = \frac{1}{2\pi L_1 f_s^2}\tag{4.7}$$

and the phase Φ_v of $H_v(f)$ is

$$\begin{aligned}\phi_v &= \frac{\pi}{2} - tan^{-1}\frac{f/f_s}{Q_s\left(1 - \frac{f^2}{f_s^2}\right)} \text{ for } f \le f_s\\[2mm]&= -\frac{\pi}{2} + tan^{-1}\frac{f/f_s}{Q_s\left(1 - \frac{f^2}{f_s^2}\right)} \text{ for } f > f_s\end{aligned}\tag{4.8}$$

According to (4.6) and (4.8), the amplitude of I_m has maximum gain at the serial resonance frequency f_s. Moreover, the phase of I_m will align with V_{in} at f_s. Thus, the maximum efficiency for transmitting ultrasound will exist when the PT is driven at f_s with a sinusoidal voltage waveform.

4.2 Driving with a Switching Power Supply

To generate ultrasound large enough in distance measurement system, the PT should be driven with a high-power AC source and it can be realized with a high-power audio amplifier. This amplifier can both provide enough energy to drive the PT and generate a sinusoidal wave at the resonant frequency of the PT. However, a high-power audio amplifier which can operate at the bandwidth of ultrasound is usually expensive and needs a bulky heat sink due to its low efficiency. Therefore, to increase the efficiency of the driver and to reduce the cost, the PT is usually driven with a switch power supply which generates pulse width modulation waveforms.

Switch power supplies have output impedance over a wide range. It could be seen as a current source when the output impedance is high and as a voltage source when the output impedance is low. Moreover, the operation of the power switch in the converter might change the configuration of the PT between open-circuit and short-circuit.

Consequently, the resonant frequency of the PT driven with a switch power supply can

locate between f_s and f_p, and the value will be

$$f_{r,PWM} = (\frac{t_s}{t_s + t_o} \cdot \frac{1}{f_s} + \frac{t_o}{t_s + t_o} \cdot \frac{1}{f_p})^{-1} = \frac{f_s f_p (t_s + t_o)}{t_s f_p + t_o f_s} \tag{4.9}$$

where t_s is the time when the PT is in short-circuit or connected to an energy source

with high impedance, and t_o is the time when the one is in open-circuit or connected to

an energy source with low impedance in one driving cycle. When the PT is operated at

the frequency shown in (4.9), the phase difference between the driving waveforms and

I_m should be a fixed value.

4.3   Harmonic Currents of the Pulse Waveform Driving

Conventionally, the driving waveforms generated from the switch power supplies

are pulse waveforms, which contain a lot of harmonic components besides its

fundamental component. These harmonic may cause distortion on the waveform of I_m

and should be considered when the PT is driven at the resonant frequency.

Assume that the width of the pulse waveform X_{pulse} is β. Fig. 4.2 illustrates the

pulse waveform. Then, it could be represented as combinations of its harmonic, and the

Fourier series of X_{pulse} would be

35
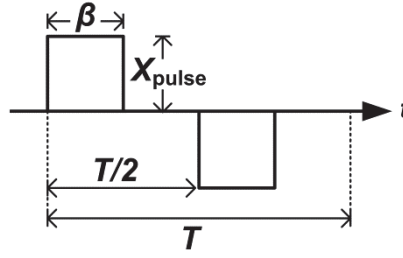
Fig. 4.2. Pulse waveform.

$$X_{pulse} = \sum_{k=1}^{\infty} \frac{4sin(k\pi f_0 \beta)}{k\pi} X_{pulse(k)} \tag{4.10}$$

where k is a positive integer. $X_{pulse(k)}$, of which the magnitude is 1, is the k-th harmonic

of X_{pulse}.

4.3.1 Pulse Current Waveform

If X_{pulse} is a pulse current waveform I_{pulse}, the fundamental frequency should be the

parallel resonance frequency f_p of the PT. Moreover, If the inequality

$$\frac{f}{f_p} \gg Q_p(1 - \frac{f^2}{f_p^2}) \tag{4.11}$$

could be true when the operating frequency does not approach f_p, (4.2) could be

rewritten as

$$H_i(k) \cong \alpha_i Q_p \angle \phi \text{ for } k = 1$$

$$\cong \frac{\alpha_i}{1 - k^2} \text{ for } k \neq 1. \tag{4.12}$$

which means

$$I_m \cong \sum_{k=1}^{\infty} \frac{4 \sin(k\pi f_p \beta)}{k\pi} H_i(k) I_{pulse(k)}$$

$$\cong \frac{4\alpha_i}{\pi} \left(Q_p \sin(\pi f_p \beta) I_{pulse(1)} \angle \phi_i + \sum_{k=2}^{\infty} \frac{\sin(k\pi f_p \beta)}{k(1-k^2)} I_{pulse(k)} \right)$$

(4.13)

where Φ_i is the phase difference between I_m and $I_{pulse(1)}$. The sum of the amplitude of

harmonic in (4.13) could have a maximum value, which is

$$I_{m,harmonic} = \sum_{k=2}^{\infty} \left| \frac{\sin(k\pi f_p \beta)}{k(1-k^2)} \right| \leq \sum_{k=2}^{\infty} \left| \frac{1}{k(1-k^2)} \right| = \frac{1}{4}$$

(4.14)

As a result, if Q_p, which only relates to the amplitude of the fundamental frequency,

is large enough. I_m could be seen as a sine wave of which the frequency is the same as

the fundamental frequency of I_{pulse}.

4.3.2 Pulse Voltage Waveform

Likewise, if X_{pulse} is a voltage pulse waveform V_{pulse}, the fundamental frequency of

X_{pulse} should be f_s. Assume that the inequality

$$\frac{f}{f_s} \gg Q_s (1 - \frac{f^2}{f_s^2})$$

(4.15)

could be established. Then, the transfer function $H_v(f)$ in (4.6) would become

$$H_v(k) \cong \alpha_v Q_s \angle \phi \text{ for } k = 1$$

$$\cong \frac{\alpha_v k}{1-k^2} \text{ for } k \neq 1,$$

(4.16)

and I_m would be

$$I_m \cong \sum_{k=1}^{\infty} \frac{4 \sin(k\pi f_s \beta)}{k\pi} H_v(k) V_{pulse(k)}$$

(4.17)

$$\cong \frac{4\alpha_v}{\pi} \left(Q_s \sin(\pi f_s \beta) V_{pulse(1)} \angle \phi_v + \sum_{k=2}^{\infty} \frac{\sin(k\pi f_s \beta)}{1 - k^2} V_{pulse(k)} \right)$$

where Φ_v is the phase difference between I_m and $V_{pulse(1)}$. The maximum value for the

sum of the amplitude of harmonic would be

$$I_{m,harmonic} = \sum_{k=2}^{\infty} \left| \frac{\sin(k\pi f_s \beta)}{1 - k^2} \right| \leq \sum_{k=2}^{\infty} \left| \frac{1}{1 - k^2} \right| = \frac{3}{4}$$

(4.18)

Hence, if the amplitude of the fundamental frequency in (4.17) is much larger than

the one shown in (4.18), I_m could also be regarded as a sine wave of which frequency is

the fundamental frequency of V_{pulse}.

Chapter 5

Resonance-Frequency-Tracking Circuit for Low-Coupling-Coefficient Piezoelectric Transducers

This chapter presents a driving circuit which can track the serial resonance frequency f_s of a PT with a low coupling coefficient. Conventionally, the frequency with zero reactance f_r approximates the frequency f_s in a PT. This characteristic can be used to track the resonant frequency of the PT. However, if the coupling coefficient of a PT is low, f_r might not exist and could not be directly regarded as f_s. Nevertheless, by driving the PT with a square wave instead of a sine wave voltage, the phase of the mechanical current I_m, which has zero phase difference with the driving voltage at f_s, can be known. Thus, f_s can be tracked with techniques related to conventional phase-locked loops. A prototype inverter circuit has been built to verify the proposed control method, and the experimental results show that the PT with a low coupling coefficient can be automatically operated at the frequency close to the ideal resonant frequency.

5.1 Input Capacitance Compensation with Square Voltage Waveform

The PT could be driven with a square wave voltage instead of a sine wave voltage to overcome the difficulty of applying phase-locked loop control. The ideal waveforms
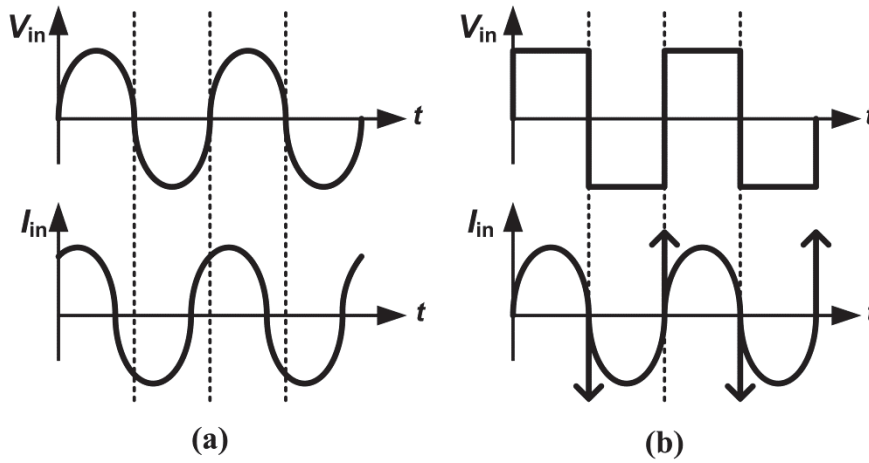
Fig. 5.1. Driving waveforms at f_s when V_{in} is (a) a sine wave. (b) a square wave.

of the input voltage V_{in} and the current I_{in} are illustrated in Fig. 5.1. Due to the high

quality factor of the PT, the mechanical current I_m can still be considered as a sine wave.

In Fig. 5.1(a), when the waveform of V_{in} is a sine wave, I_{in} is composed of I_m and the

current flowing through the parallel capacitor C_0 of the PT. At this condition, I_{in} lags V_{in}

at f_s. However, if the waveform of V_{in} is a square wave, the current from C_0, which is a

narrow current pulse, only emerges at the edge of the square wave voltage in Fig. 5.1(b).

Thus, I_m can be distinguished, and its phase can be known. Moreover, I_m should have

zero phase difference with V_{in} at f_s when V_{in} is a square wave. Then, the resonant

frequency of a low coupling coefficient PT may be tracked with square voltage wave as

its driving voltage.

The frequency tracking control method could be similar to a conventional

phase-locked loop. Because the mechanical resonator can be regarded as a serial R-L-C

circuit, its phase in the Bode plot change in a single direction with the frequency

40
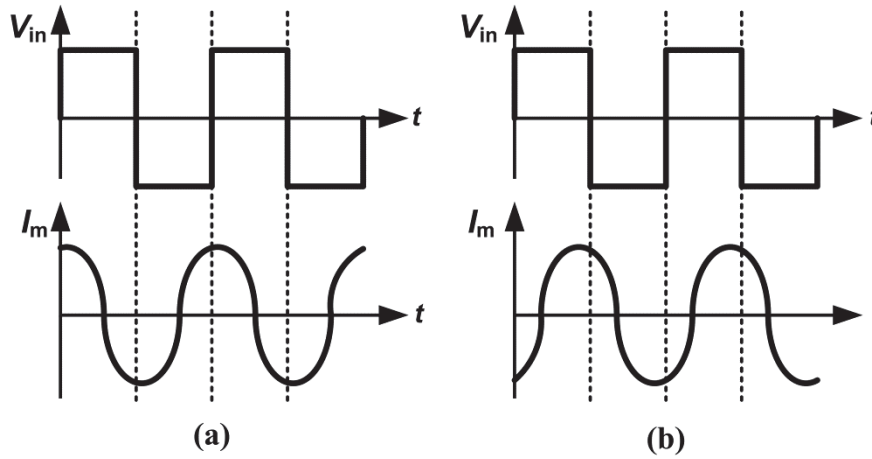
Fig. 5.2. Ideal relationship between V_{in} and I_m at (a) $f < f_s$. (b) $f > f_s$.

varying from low to high. When the operating frequency is lower than f_s, V_{in} lags I_m. In contrast, when the operating frequency is higher than f_s, V_{in} leads I_m. The waveforms in these two conditions are represented in Fig. 5.2. Thus, if the control loop can response to this phase difference, the serial resonance frequency f_s, at which V_{in} and I_m has zero phase difference, could be tracked. However, a short and large current pulse would emerge at the edges of the square wave voltage due to the existence of C_0. This short-circuited current pulse may distort the phase of the detected current waveform and should be removed from the feedback loop. This could be realized with a sampling circuit.

The sampling circuit records the current flowing direction before the positive edge or the negative edge of the driving voltage to avoid the influence of current pulse shown in Fig. 5.1(b). Because I_m will have the same frequency as V_{in}, whether the phase of I_m leads or lags V_{in} could be known from the flowing direction of the current at the edge of
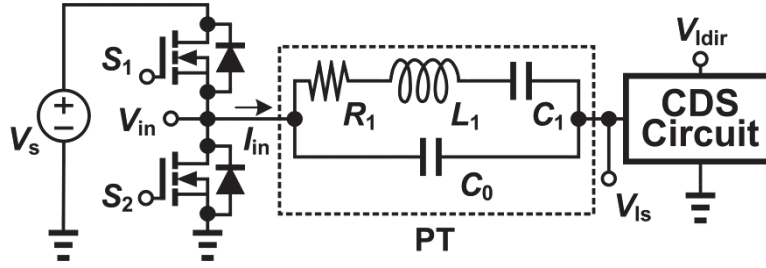
Fig. 5.3. Configuration of the proposed circuit.

the square wave V_{in}. However, the current waveform may be distorted by the short-circuited current pulse. The timing for detecting the current flowing direction should be in front of the edge of V_{in} for a period of time, and this time period should not be too long to prevent further error between the tracked frequency and the ideal resonant frequency of the PT.

5.2 Circuit Implementation

5.2.1 Half-Bridge Inverter Configuration

The configuration of the proposed circuit for the PT is provided in Fig. 5.3. It is composed of a half-bridge inverter, a current direction sensing circuit (CDS circuit), and this circuit is controlled with a digital microcontroller (MCU). The half bridge inverter realized with two power transistors, S_1 and S_2, is used to generate the square voltage waveform. The duty cycles of these transistors are both approximate 50% of the whole cycle, and the conducting time of these transistors would not overlap each other to prevent the voltage source V_s from short circuit faults. The current flowing direction
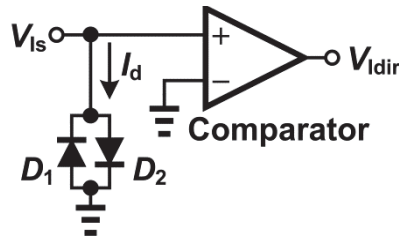
Fig. 5.4. Configuration of current flowing direction sensing circuit.

sensing circuit provides a digital signal representing the information of current flowing

direction. The MCU is functioned as the control circuit. It receives the signal of current

flowing direction and provides the signals for driving the power transistors via gate

drivers. The explanations of the control algorithm of the MCU to track the resonant

frequency will be presented below.

5.2.2　Current Direction Sensing Circuit

A pair of diodes, D_1 and D_2, with a comparator consists of the current flowing

direction sensing circuit. Its topology is shown in Fig. 5.4. The diodes D_1 and D_2 are

reversely connected. If I_m flows from the PT to ground, the voltage value of V_{Is} will be

approximate 0.7 V. Conversely, if I_m flows from ground to the PT, the voltage value of

V_{Is} will be approximate -0.7 V. Because the value of V_{Is} is clamped by these two diodes,

V_{Is} can be directly used as the input of a comparator without any voltage divider. Then,

the comparator will enlarge the voltage signals to 0 V and 5 V, which respectively

represent signals 0 and 1 for a digital controller.
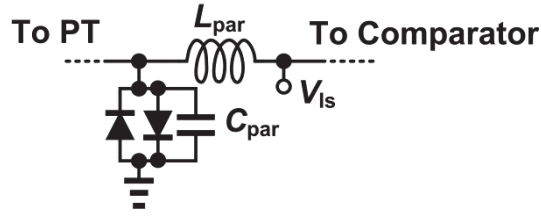
Fig. 5.5. Parasitic components configuration.

The detected signal V_{Is} may contain a lot of noise. When the power transistors are turned on, a short-circuited current flows through the parallel capacitance C_0 and the current direction sensing diode. If the operating frequency is larger than the serial resonance frequency f_s, the flowing direction of the short-circuited current and I_m is reverse. Because the peak value of the short-circuited current is much larger than I_m, the signal of current flowing direction V_{Idir} will be changed for a short while. Moreover, this short-circuited current could also cause oscillation between the parasitic inductors L_{par} in the wire connected to the input of the comparator and the parasitic components C_{par} of the sensing diodes. The configuration of those parasitic components is drawn in Fig. 5.5. This oscillation may influence the voltage value of V_{Is} and make V_{Idir} change its value if the amplitude of I_m is small. Therefore, the value of the current flowing signal V_{Idir} should be sampled before one of the transistors is turned on in every cycle to avoid the noise generated by the short-circuited current.

5.3 Operation Principles

5.3.1 Key Waveforms

The key waveforms of the operation are presented in Fig. 5.6. Assume that the duty cycle of V_{in} is exactly 50 percent. Moreover, the waveforms in the first half cycle are symmetrical to the other half cycle. Hence, only the waveforms when V_{in} is positive will be described. The waveform of I_m leads V_{in} in Fig. 5.6(a) when $f < f_s$, and the waveform of I_m lags V_{in} in Fig. 5.6(b) when $f > f_s$. At t = t_0, the upper-side switch S_1 is turned-on, and V_{in} rises from zero to high voltage level. At this time, a short-circuited current flows through C_0 and the current direction sensing diodes. If $f > f_s$, the direction of this current is opposite to I_m. Thus, the polarity of V_{Is} will be changed until I_m recharges the parasitic capacitance of the diodes at t = t_{0a}. Conversely, If $f < f_s$, the direction of the short-circuited current is the same as I_m. Hence, the polarity of V_{Is} will remain if the oscillation caused by the parasitic components is not too large. Then, at t = t_1, I_m changes its flowing direction, and the polarity of V_{Idir} will be altered, too. Finally, the half operating cycle terminates at t = t_2.

5.3.2 Tracking Strategy

The proposed control strategy for the MCU to track the resonant frequency is perturb-and-observe. The MCU changes the operating frequency for a step a frequency.
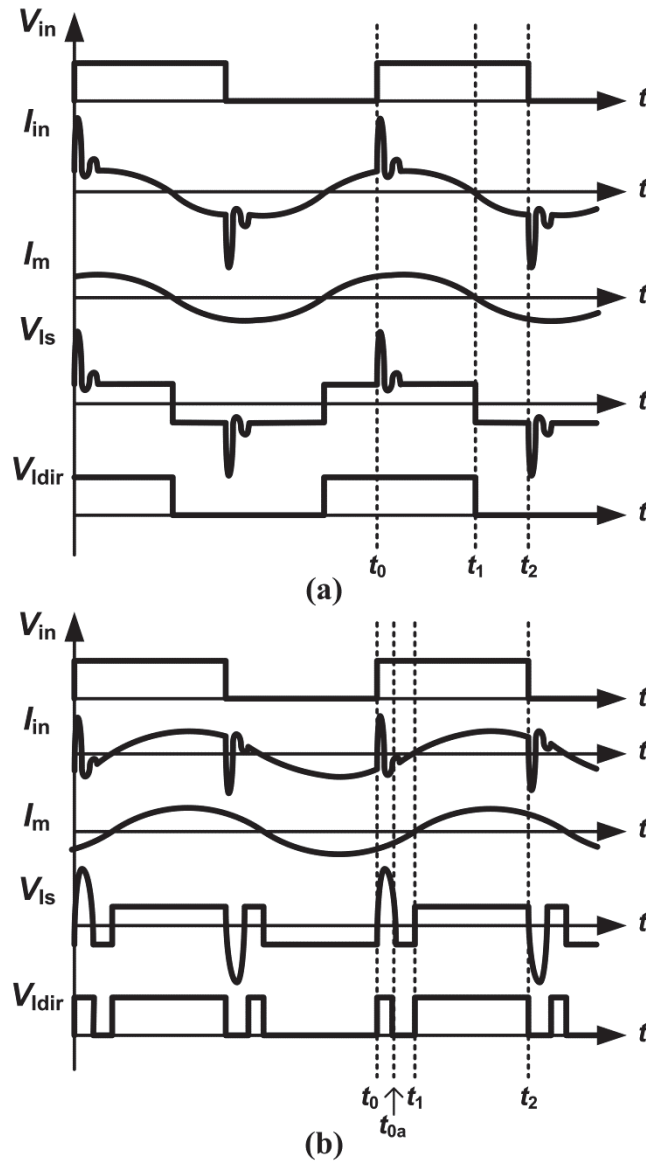
Fig. 5.6. Key waveforms at (a) $f < f_s$. (b) $f > f_s$.

Then, it observes the voltage value of V_{Idir}, which gives the flowing direction of I_m and

finally decides whether the operating frequency will be increased or decreased in the

next control cycle. Furthermore, the timing for sampling V_{Idir} could be aligned with the

reset signal of the timer, which is a counter to determine the output of the actuating

signal in the MCU. Because a short period of dead time is added to prevent the voltage

46
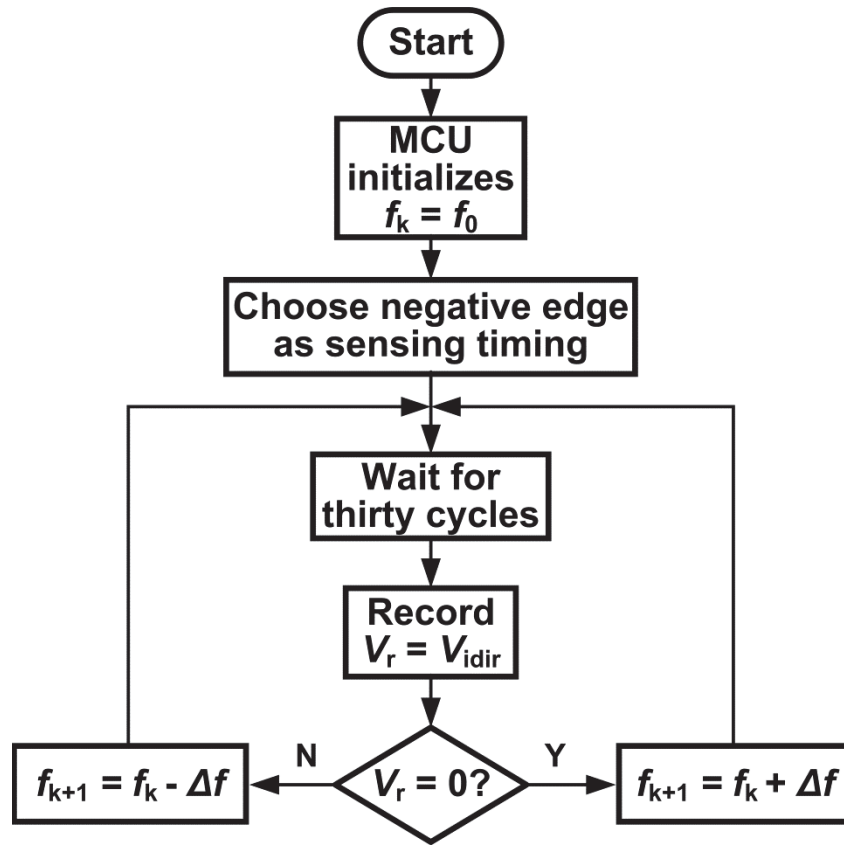
Fig. 5.7. Tracking flowchart.

source from short-circuit, the driving signal of the transistors will be blocked for a period of time at the beginning of the control cycle. Thus, the time for sampling will be located before the edge of V_{in} for a period of time equaling to the dead time.

The control flows for the MCU are as follows. First, initialize the MCU and set the initial operating frequency. Next, choose the timing before the negative edge of V_{in} as the sampling timing. After thirty cycles pass, the system is in steady state. Then, sample the value of V_{Idir} and assign the value to a register V_r in the MCU. If $V_r = 0$, the operating frequency should increase for a step of frequency Δf in the next control cycle.
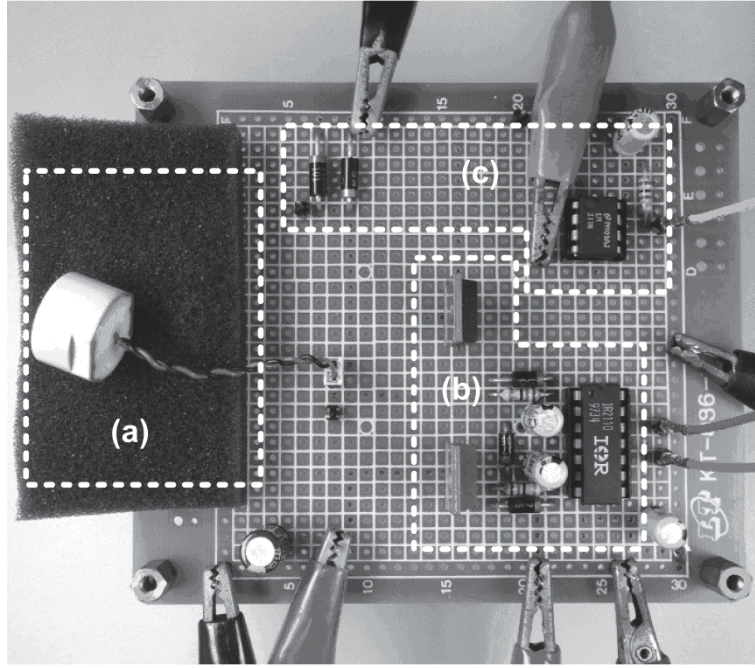
Fig. 5.8. Prototype of the implemented circuit. (a) PT. (b) half-bridge inverter.

(c) current direction sensing circuit.

Otherwise, the operating frequency should decrease in the next control cycle. The flowchart for the MCU is summarized in Fig. 5.7.

5.4 Experimental Results

A prototype circuit has been constructed to realize the proposed resonant frequency tracking control. Fig. 5.8 shows the photo of the implemented circuit. The PT in this circuit was manufactured by Tung Thih Electronic Co., and the values of its components were measured by an impedance analyzer. The measured results and the characteristic frequencies are listed in Table 5.1. Although this PT does not have a zero reactance frequency f_r, The series resonance frequency f_s of the PT can be tracked with the

Table 5.1 Specification of the PT

Parameter	Value
C_0	1.563 nF
R_1	1.330 kΩ
L_1	155.7 mH
C_1	47.64 pF
f_r	not exist
f_s	58.44 kHz
f_m	58.08 kHz

Table 5.2 Part Number of the Components

Component	Part Number
MCU	dsPIC30F2020
S_1, S_2	IR930G
D_1, D_2	MUR1100E
Comparator	LM311N
Gate driver	IR2110

proposed control circuit. Additionally, the time in front of the negative edge of the driving voltage V_{in} is chosen for sampling V_{Idir}. Moreover, the voltage value of the input voltage source was set to be 24 V, and the part numbers of the discrete components in the circuit are summarized in Table 5.2.

The operating waveforms of the converter are provided below. In Fig. 5.9, the waveform shows the driving voltage V_{in} of the PT, the output voltage V_{Idir} of the comparator, and the voltage V_{Is} crossing the current direction sensing diodes. The

Fig. 5.9. Waveforms for $f < f_s$. (vertical: V_{in}, 20 V/div; V_{Idir}, 5 V/div; V_{Is}, 5 V/div;

horizontal: 5 μs/div)

operating frequency in Fig. 5.9 is at 57.35 kHz, which is below the serial resonance

frequency f_s of the PT. Thus, the waveform of V_{Idir}, which represents the phase of the

current, leads the waveform of V_{in}. Moreover, voltage spikes occur on the waveform of

V_{Is} at the positive and negative edge of V_{in}. These spikes are induced by the

short-circuited current of C_0 in the PT. The flowing direction of these spikes should be

the same as the mechanical current I_m. However, due to the parasitic components, the

voltage V_{Is} oscillates after the spike and the amplitude of the oscillation is large enough

to cause a pulse on V_{Idir} at the positive edge of V_{in}. At the negative edge, the oscillation

does not cause a voltage pulse on V_{Idir} because the current path from the voltage source

to the node V_{in} could be with a larger parasitic capacitance than the one between the

node V_{in} to ground. In Fig. 5.10, the operating frequency is 58.67 kHz, which is higher
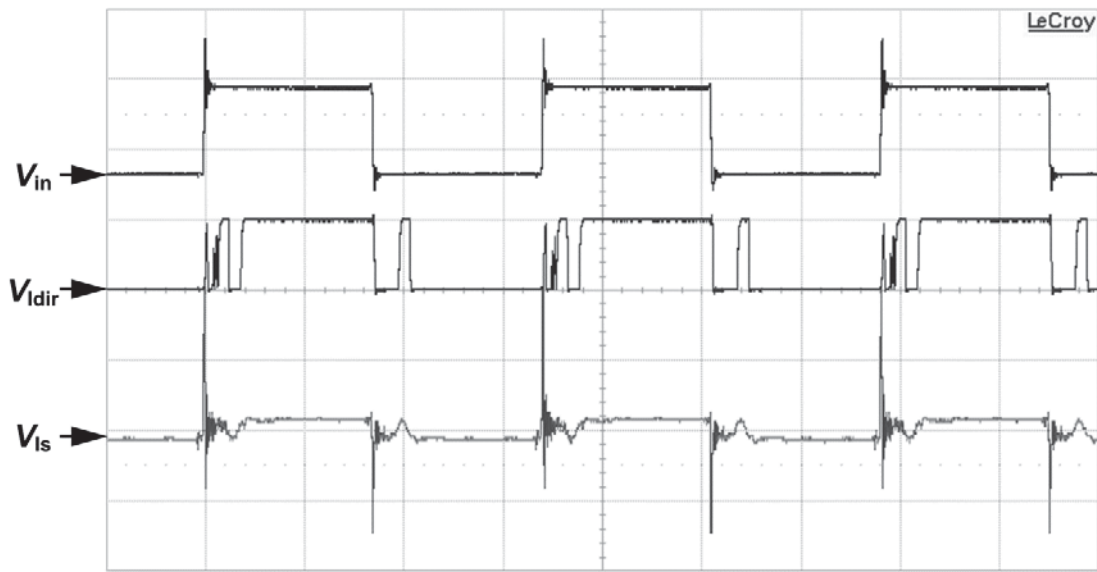
Fig. 5.10. Waveforms for $f > f_s$. (vertical: V_{in}, 20 V/div; V_{Idir}, 5 V/div; V_{Is}, 5 V/div; horizontal: 5 μs/div)

than f_s. The waveform of V_{Idir} should lag the waveform of V_{in}. However, due to the voltage spike on V_{Is}, of which the current flowing direction is reverse to I_m, the waveform of V_{Idir} changes with the edge of V_{in}. After the oscillation occurs by the spike comes to a halt, V_{Is} will be determined by I_m and then change the value of V_{Idir}.

The waveforms of the resonant frequency tracked process are shown in Fig. 5.11. The waveform V_{dir} in Fig. 5.11 is a voltage signal from the MCU that indicates whether the operating frequency will be increased or decreased in the next cycle. If $V_{dir} = V_{dd}$, the operating frequency will be increased. If $V_{dir} = 0$, the operating frequency will be decreased. The initial operating frequency is 53.2 kHz and one-step frequency change Δf is approximate 0.16 kHz to acquire large enough variation of the phase difference between V_{in} and V_{Idir}. According to the waveform of V_{dir}, after the tracking process starts,

51
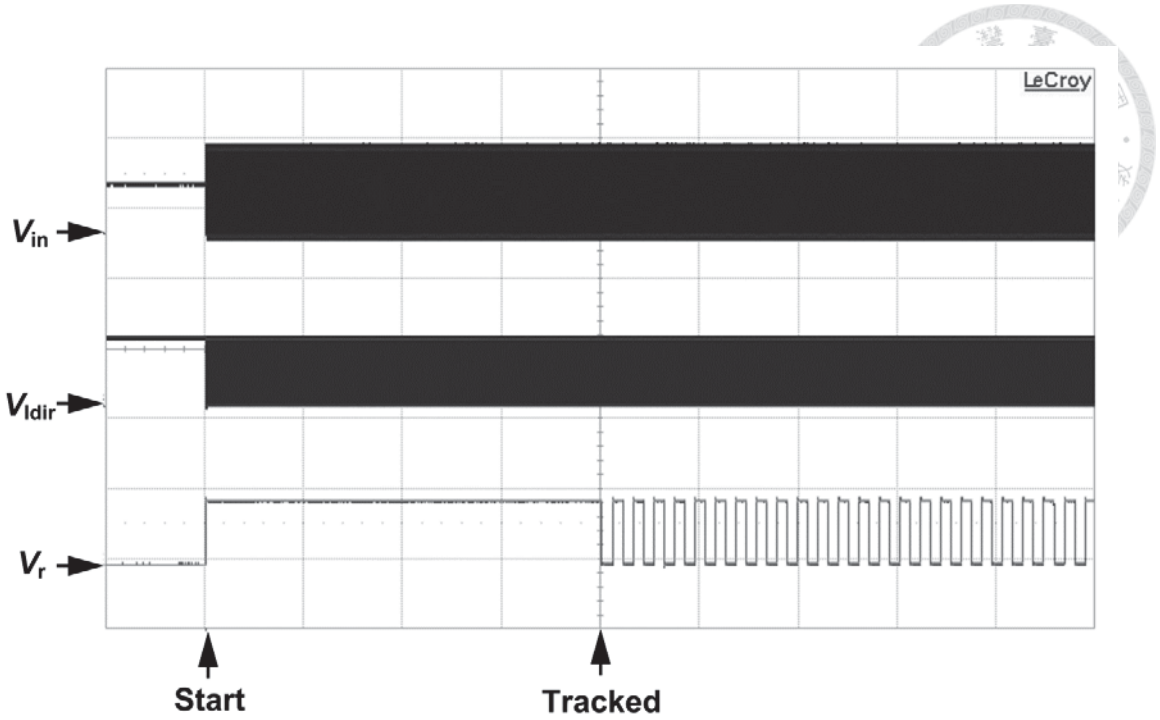
Fig. 5.11. Resonant frequency tracked waveforms. (vertical: V_{in}, 20 V/div; V_{Idir},

5 V/div; V_r, 5 V/div; horizontal: 5 ms/div)

the operating frequency increases consistently until the operating frequency reaches

58.03 kHz. Then, the waveform of V_{dir} starts to oscillate and the operating frequency is

alternated between 57.86 kHz and 58.03 kHz. The operating waveform at these two

frequencies is shown in Fig. 5.12. The waveform of V_{in} lags V_{Idir} in Fig. 5.12(a) and

leads V_{Idir} in Fig. 5.12(b). Thus, the waveform of V_{in} and V_{Idir} should be zero phase

difference at a frequency, which could be regarded as the tracked resonant frequency,

between 57.86 kHz and 58.03 kHz. However, this frequency range does not include the

ideal serial resonance frequency f_s, which is 58.44 kHz. This may be caused by the

delays in the control loop. Because the current direction sensing diodes need some

charge to turn on and there is delay from the input node to the output node of the

52
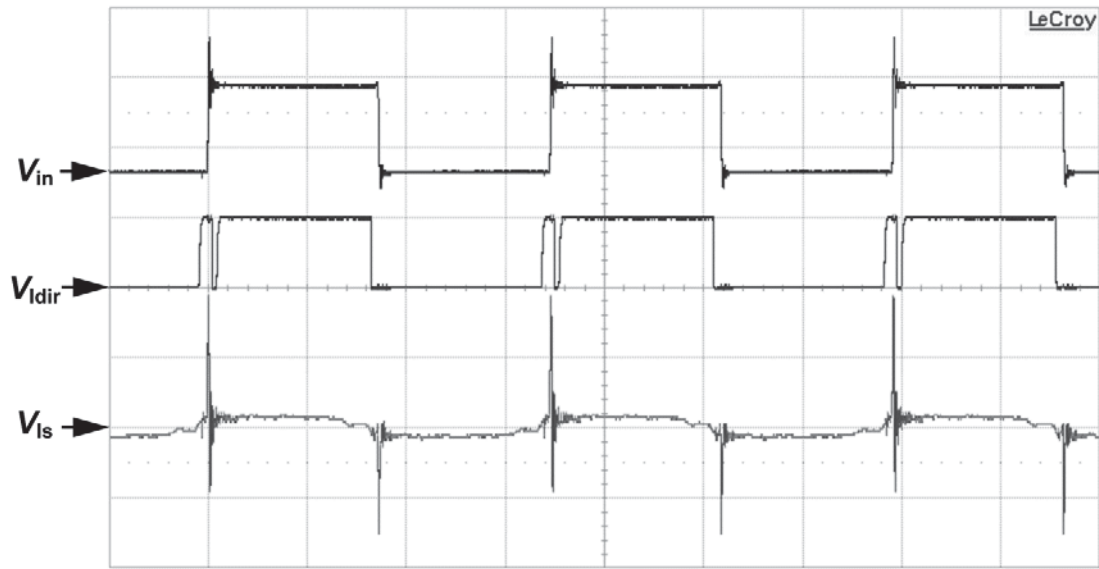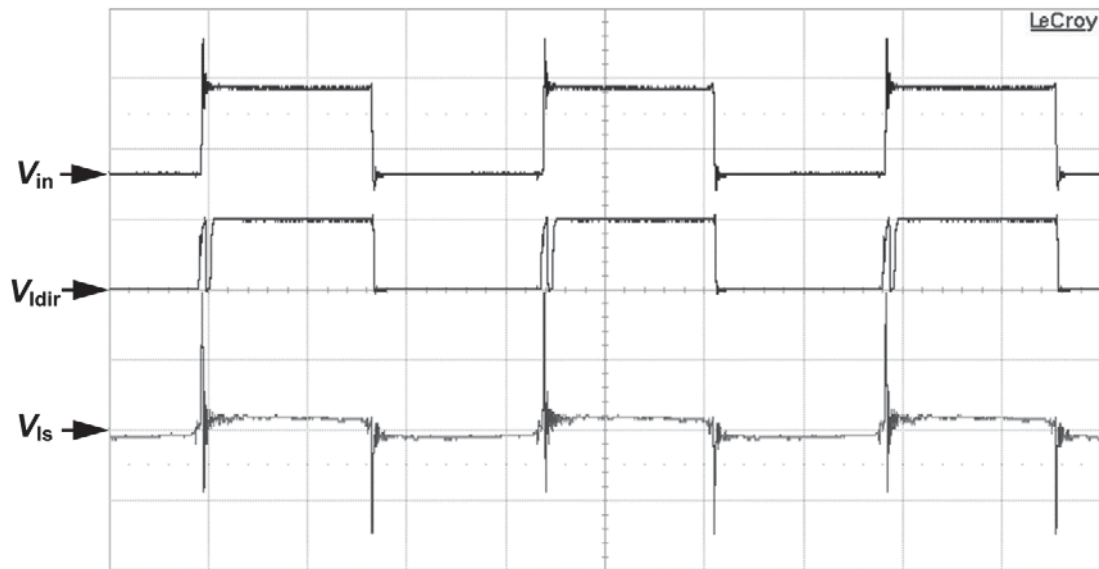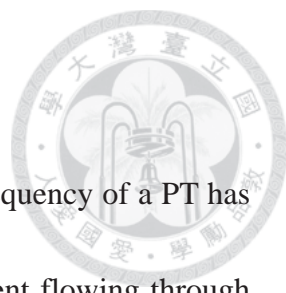
Fig. 5.12. Waveforms of the tracked frequencies: (a) 57.86 kHz (b) 58.03 kHz.

(vertical: V_{in}, 20 V/div; V_{Idir}, 5 V/div; V_{Is}, 5 V/div; horizontal: 5 μs/div)

comparator, the waveform of V_{Idir} may lag the actual waveform of I_m. Therefore, the tracked resonant frequency would be lower than the ideal value of f_s.

5.5   Summary

In this chapter, a novel driving method to track the resonant frequency of a PT has been proposed. By driving with a voltage of square wave, the current flowing through C_0 of the PT only occurs in the form of current pulses at the positive and negative edge of V_{in}, and the phase of I_m in the PT could be directly detected from the input current. Then, the resonant frequency can be tracked from the phase difference between V_{in} and I_m. According to the experimental results, the operating frequency of the inverter circuit can alternately stay at two frequencies which are close to the ideal resonant frequency. Therefore, it may be appropriate to apply this circuit to track the resonant frequency of a PT with low coupling coefficient.

Chapter 6

Resonance-Frequency-Tracking Method for

Current-Fed Piezoelectric Transducers

This chapter presents a novel control method for a current-fed full-bridge inverter driving an ultrasonic PT. In the conventional ultrasonic detection system, the PT has maximum transmitting gain at its series resonance frequency f_s while having maximum receiving gain at its parallel resonance frequency f_p. With the proposed approach, the PT could have maximum transmitting gain at f_p, and this frequency can be automatically tracked and hence adapted to the environmental variation. A prototype circuit was constructed to verify the proposed control method. The experimental results show that the receiving voltage signal could have a maximum value at f_p, and the tracked frequency approximates this resonant frequency.

6.1 Resonance-Frequency Detection with Zero-Voltage-Switch Technique

Whether ZVS could be achieved depends on the impedance of the resonator which is connected with transistors. The original purpose of applying ZVS techniques on transistors of converter is to avoid the loss of energy stored in the parasitic capacitances of transistors, which can in turn enhance the efficiency of the convertor [39].
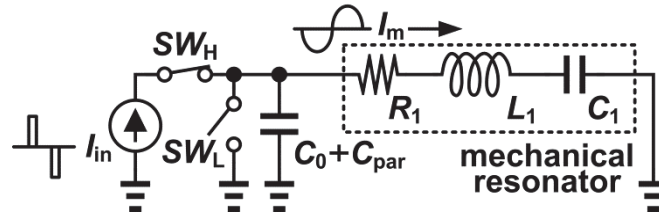
Fig. 6.1. Driving process of ZVS.

When a bridge-type inverter directly actuates a PT, its parallel capacitance C_0 is parallel to the output capacitance C_{par} of the transistor. The configuration is shown in Fig. 6.1. If the driving waveform is a narrow current pulse train, the PT will be in open-circuit for most of the time. Thus, capacitances parallel to transistors would act as an integrator of the mechanical current I_m, and the quantity of electrical charge transfers into the mechanical resonator could be known. If ZVS is achieved, the energy transfers from power supplies to the capacitances C_0 and C_{par} would completely transfer into the mechanical resonator. The amplitude of the mechanical current should be larger than those which cannot achieve ZVS so tracking the frequency where the switches of the inverter can achieve ZVS could find the resonant frequency of the PT. However, whether this tracking method could be applied to PTs depends on their characteristics. The analyses of the proposed tracking method are derived as follows:
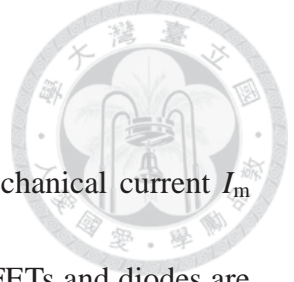
6.1.1 Input Pulse Current and Mechanical Current

Assume that the quality factor of a PT is so large that its mechanical current I_m could be seen as a sine wave and that all transistors including MOSFETs and diodes are ideal. Moreover, lower side switches of the inverter have achieved ZVS in steady state so the energy delivered by the power supply is completely consumed in the PT. The power stage actuating the PT is a full-bridge inverter which transfers energy twice the amount per period. After a current pulse is injected, the voltage of C_0 rises from 0 to V_p, of which the value is determined by the waveform of I_{in}. The energy transferred into the PT per period is

$$E_{per} = 2 \times \frac{1}{2} C_0 V_p{}^2 = C_0 V_p{}^2 . \tag{6.1}$$

Then, the average power into the PT will equal to the power dissipated on the resistance R_1 in steady-state condition.

$$P_{avg} = \frac{E_{per}}{T} = \frac{C_0 V_p{}^2}{T} = \frac{1}{2} R_1 I_m{}^2 \tag{6.2}$$

where T is the period of the inverter. From (6.2), the amplitude of the mechanical current I_m when ZVS has been achieved is derived as

$$I_m = V_p \sqrt{\frac{2C_0}{TR_1}} = V_p \sqrt{\frac{\omega C_0}{\pi R_1}} \tag{6.3}$$

where ω is the radius frequency of the inverter.

6.1.2 Boundary Condition of Achieving Zero-Voltage-Switch

If the boundary condition was derived, whether the proposed tracking method could apply to the PT could be known. When the PT is driven by current pulse, the phase Φ of the transfer function of the PT has been derived in Chapter 4, which is

$$
\begin{aligned}
\Phi &= -tan^{-1}\frac{f_n}{Q(1-f_n{}^2)} \quad \text{for } f_n \leq 1 \\
&= -\pi + tan^{-1}\frac{f_n}{Q(1-f_n{}^2)} \quad \text{for } f_n > 1
\end{aligned}
\tag{6.4}
$$

where $f_n = f/f_p$. For a convenient explanation, θ, which is the phase difference between I_m and the phase current pulse injected, is defined. The relationship between θ and Φ is

$$
\theta = \Phi + \frac{\pi}{2}.
\tag{6.5}
$$

Supposing that C_0 is much larger than C_1, then, the voltage change on C_0 will have little influence on the waveform of I_m. Thus, I_m can still be seen as a sine wave. In order to achieve ZVS, I_m should discharge C_0 to zero voltage before the next current pulse

$$
\begin{aligned}
Q_{C_0} = C_0 V_p &\leq \int I_m(t)\,dt \\
&= \int I_m \sin(\omega t)\,dt \\
&= \int V_p \sqrt{\frac{\omega C_0}{\pi R_1}} \sin(\omega t)\,dt.
\end{aligned}
\tag{6.6}
$$

By rearranging and changing the integrating variable, the inequality is obtained

$$
1 \leq \int I_n \sin(\psi)\,d\psi
\tag{6.7}
$$
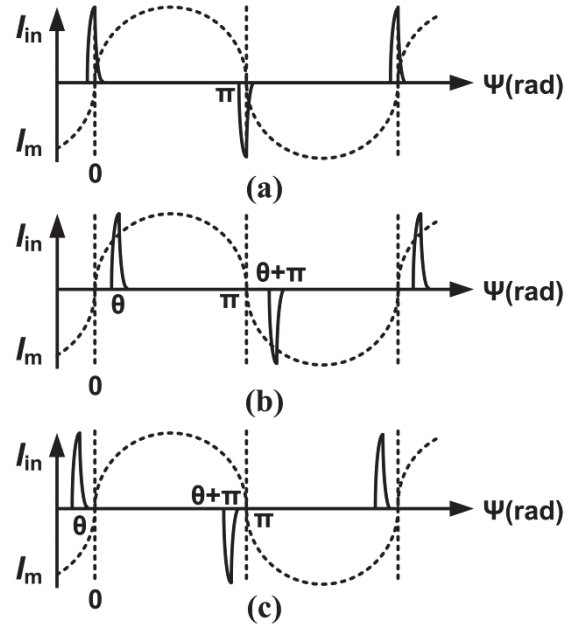
Fig. 6.2. Phase difference between I_{in} and I_m. (a) $f_n = 1$. (b) $f_n < 1$. (c) $f_n > 1$.

where $\psi = \omega t$ is the integrating variable changed from time to phase, and I_n is the

normalized current defined in

$$I_n = \sqrt{\frac{1}{\pi \omega C_0 R_1}}. \tag{6.8}$$

The integrating range of (6.7) can be observed from Fig. 6.2. When $f_n = 1$, the input

current pulse train is in phase, i.e. $\theta = 0$, with I_m. The maximum charge can be

discharged from C_0. Thus, the boundary condition for achieving ZVS is known and the

result is

$$1 \leq \int_0^{\pi} I_n \sin(\psi)\, d\psi = 2I_n \ \text{ for } f_n = 1 \tag{6.9}$$

which means f_p is the frequency where the lower side switches are most likely to

achieve ZVS.
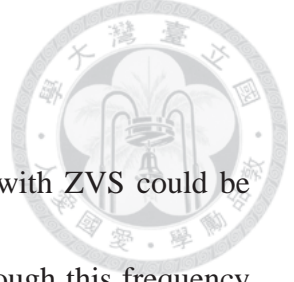
6.1.3 Ideal Zero-Voltage-Switch Frequency Range

If the boundary condition is satisfied, a range of frequencies with ZVS could be acquired, and it is called ZVS frequency range in this chapter. Although this frequency range must include f_p, the exact value of f_p is not known. However, due to the high quality factor of the PT, the phase sharply changes in this frequency range. This frequency range would be narrow around f_p. The theoretical ZVS frequency range could be derived from (6.7). For $f_n < 1$ in Fig. 6.2(b), I_{in} lags I_m. If C_0 reaches zero voltage before $\psi = \pi$, the PT can be short-circuited to prevent the reverse directional current back to C_0. Thus, the integrating range is from θ to π, and the normalized lower bound of the frequency range could be known from

$$1 \leq \int_{\theta}^{\pi} I_n \sin(\psi)\, d\psi = I_n(1 + cos\theta) \text{ for } f_n \leq 1. \tag{6.10}$$

For $f_n > 1$ in Fig. 6.2(c), the input current pulse train leads I_m. The phase difference θ is a negative value. The initial reverse directional current should be included. Thus, the integrating range is θ to $\theta + \pi$, and the normalized upper bound of the frequency range could be known from

$$1 \leq \int_{\theta}^{\pi+\theta} I_n \sin(\psi)\, d\psi = 2I_n cos\theta \text{ for } f_n \geq 1. \tag{6.11}$$

From (6.10) and (6.11), the upper bound is closer to f_p than the lower bound. Assume that I_n defined in (6.8) could be seen as a variable independent of frequency, the theoretical value of the upper bound frequency could be derived from (6.4) and (6.11)
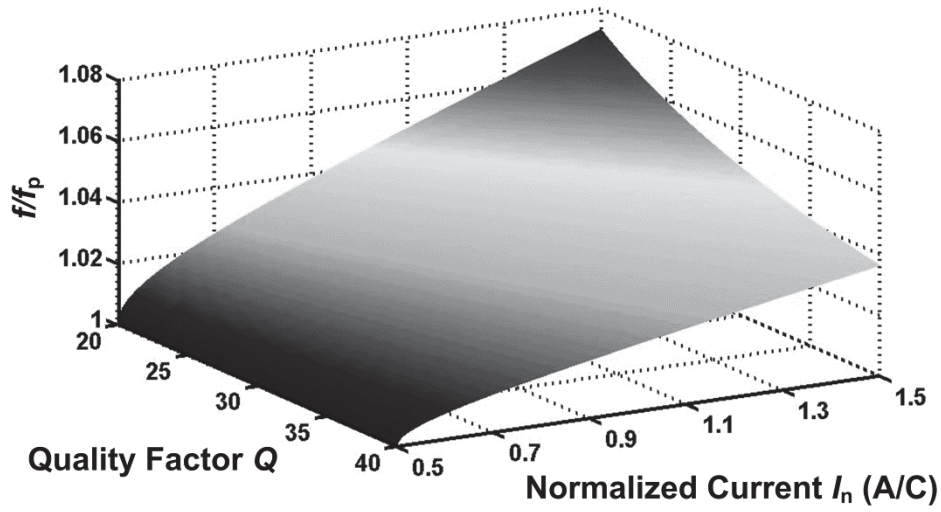
Fig. 6.3. Upper bound frequency versus quality factor and normalized current.

$$f_{n,u} = \sqrt{1 + \frac{4I_n{}^2 - 1}{2Q^2} + \sqrt{\frac{(4I_n{}^2 - 1)^2}{4Q^4} + \frac{(4I_n{}^2 - 1)}{Q^2}}} \qquad (6.12)$$

The value of (6.12) is drawn as Fig. 6.3. From Fig. 6.3, if the quality factor Q is

large enough, the upper bound frequency would be very close to f_p. Thus, with the

abovementioned analysis, the proposed control method could track f_p of the PT, and the

transmitting circuit could generate ultrasound with maximum power efficiency at this

frequency.

6.1.4   Comparison with Conventional Detecting Method

The contour maps of maximum phase of input impedance Z_{in} and I_n value of a PT

are shown in Fig. 6.4. If the converter tracks the zero phase difference of the input

voltage and current to detect the resonance frequency, the maximum phase of Z_{in} should
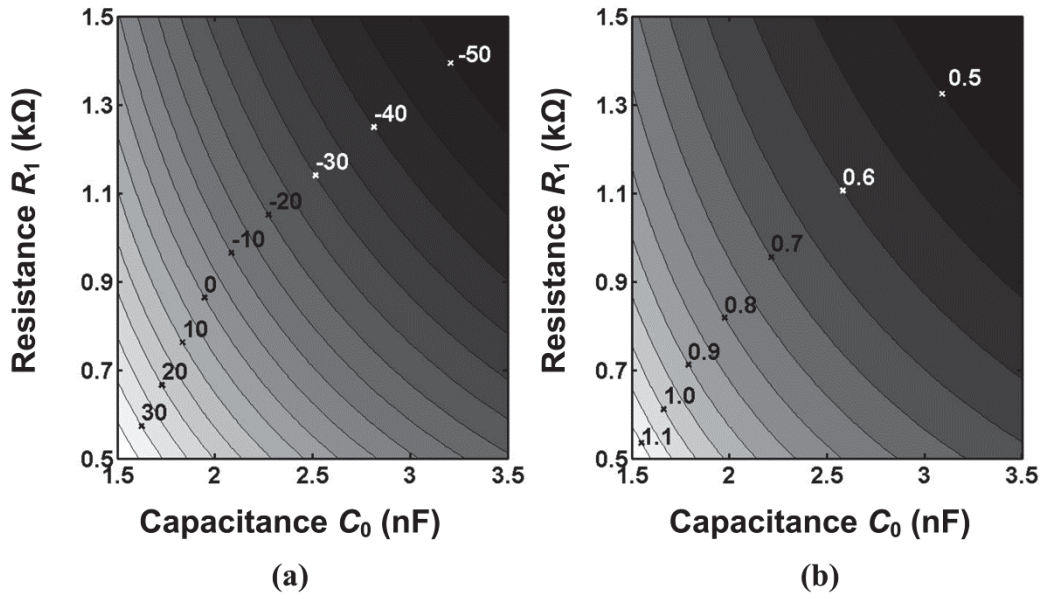
Fig. 6.4. Contour maps of characteristics of a PT ($L_1 = 74$ mH and $C_1 = 145$ pF).

(a) Maximum phase of Z_{in} (degree). (b) Value of I_n (A/C).

be higher than zero. If the converter tracks the resonance frequency with the proposed

method, the value of I_n should be higher than 0.5 A/C. Comparing the areas of which

$I_n > 0.5$ A/C in Fig. 6.4(b) and of maximum phase of Z_{in} in Fig. 6.4(a), it is apparent that

the former is larger than the latter. For increasing the applicable area of the conventional

method, compensation could be added to lock at a frequency whose phase is lower than

zero. However, it is difficult to know the value that should be compensated without

measuring the value of equivalent circuit. Hence, tracking the resonance frequency with

the proposed method might be more applicable to different PTs.
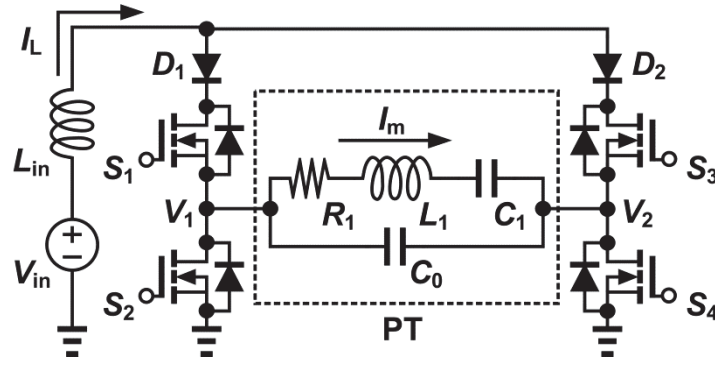
Fig. 6.5. Topology of current-fed full-bridge inverter with the PT.

6.2　Circuit Implementation

6.2.1　Current-fed Inverter Topology

The topology of the proposed circuit is shown in Fig. 6.5. It is a current-fed full-bridge inverter combing a dc/dc boost converter and a dc/ac full-bridge inverter. The inductor L_{in} changes a voltage source into a current source. Conventional applications of current-fed full-bridge inverter can be seen in [40]-[43]. This converter can generate current pulse train with proper operation to drive the PT, and the magnitude of current pulses could be adjusted with the magnetizing time.

There are two stages for transferring energy in this inverter. The first one is composed of L_{in} and C_0, and the second one is composed of C_0 and the mechanical resonator of the PT. The associated circuit is demonstrated as Fig. 6.6. In every half period, L_{in} is magnetized by the input voltage source. After L_{in} is connected to the PT, the energy will first transfer from L_{in} to C_0, and then transfer from C_0 to the mechanical

63
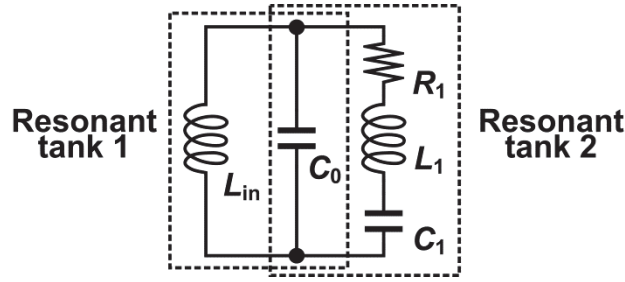
Fig. 6.6. Energy transfer in resonant tanks.

resonator. In steady state, the frequency of I_m is the same as the operating frequency of the inverter.

The input current waveform will be like a narrow current pulse train if the resonance frequency of first stage is much higher than the frequency of I_m, which means

$$\frac{1}{2\pi\sqrt{L_{in}C_0}} \gg f_{I_m}.$$
(6.13)

Additionally, L_{in} is in discontinuous conduction mode condition, and the frequency of its current waveform is twice higher than the operating frequency of switches. In this inverter, upper-side switches S_1 and S_3 are in zero-current-switch condition. Diodes D_1 and D_2 are also in zero-current-switch condition, so they have no reverse recovery problems. The inductor value of L_{in} could be determined by (6.13) and is usually small.

6.2.2   Configuration of Diodes

The purpose of connecting diodes with inductor L_{in} is to prevent energy from flowing back to the voltage source V_{in}. Therefore, the voltage change across the PT

64
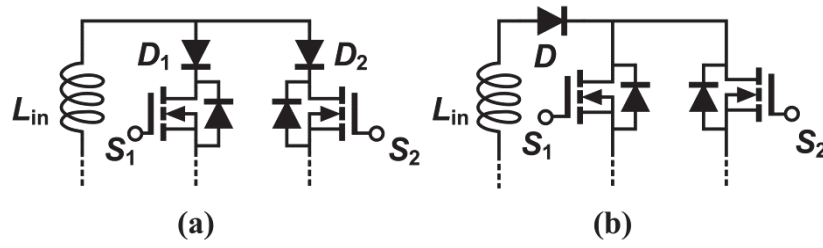
Fig. 6.7. Different configurations for blocking the reverse current. (a) Two diodes.

(b) One diode.

would only be determined by the resonance of the PT itself. Moreover, there is a similar

topology with only one serial diode, and these two different configurations of diodes are

shown in Fig. 6.7. For the configuration with one diode, the parasitic capacitance of

upper side switch S_3 could have resonance with the PT when the voltage of V_1 is still

higher than V_{in}. Hence, the turn-on losses of upper-side switches could also be reduced.

However, when L_{in} starts to be magnetized, V_1 would be short through the free-wheeling

diode of S_1. It means that the time interval for the lower side switches to achieve ZVS is

shortened, and that the adaptability of the proposed converter for tracking the resonance

frequency is reduced. For the configuration with two diodes, the aforementioned issue

could be avoided with the cost of larger turn-on losses of upper side switches. In this

chapter, the topology with two diodes was chosen to verify the adaptability of the

proposed tracking method.

6.3 Operation Principles

6.3.1 Key Waveforms

The key waveforms are shown in Figs. 6.8 and 6.9. This timing diagram is based on the assumption that all switches and diodes are ideal and that the inverter is in steady state condition. Because the input pulse current leads I_m for $f_n < 1$, one more interval is presented. Moreover, since the timing diagram t_3-t_6 is symmetrical to the timing diagram t_0-t_3, only operational intervals in the first half cycle are presented in detail.

1) Interval t_0-t_1: In this interval, the energy transfers from the inductor L_{in} into the PT. At t = t_0, the switch S_2 turns off, and S_1 and S_4 still turn on. The current in L_{in} charges C_0 and the parasitic capacitance C_{par} of S_2. Before $V_1 > V_{in}$, I_{in} will still increase for a short time. Then, L_{in} start to demagnetize until $I_{in} = 0$. The operation is shown in Fig. 6.10(a). The length of this interval is approximately:

$$t_1 - t_0 = \frac{\pi}{2}\sqrt{L_{in}(C_0 + C_{par})}. \tag{6.14}$$

2) Interval t_1-t_{u1}: At t = t_1, L_{in} is fully demagnetized. The energy transfers from C_0 and parasitic capacitances of S_1 and S_2 into the mechanical resonator. The operation is shown in Fig. 6.10(b). If $f_n < 1$, I_m immediately discharges C_0 and V_1 starts to decrease. If $f_n > 1$, I_m charges C_0. Thus, V_1 rises for a while before current direction of I_m is reversed. In addition, the upper side switch S_1 should be turned off before $V_1 < V_{in}$. Otherwise, V_{in} recharges C_0, and V_1 cannot decrease to below V_{in}.
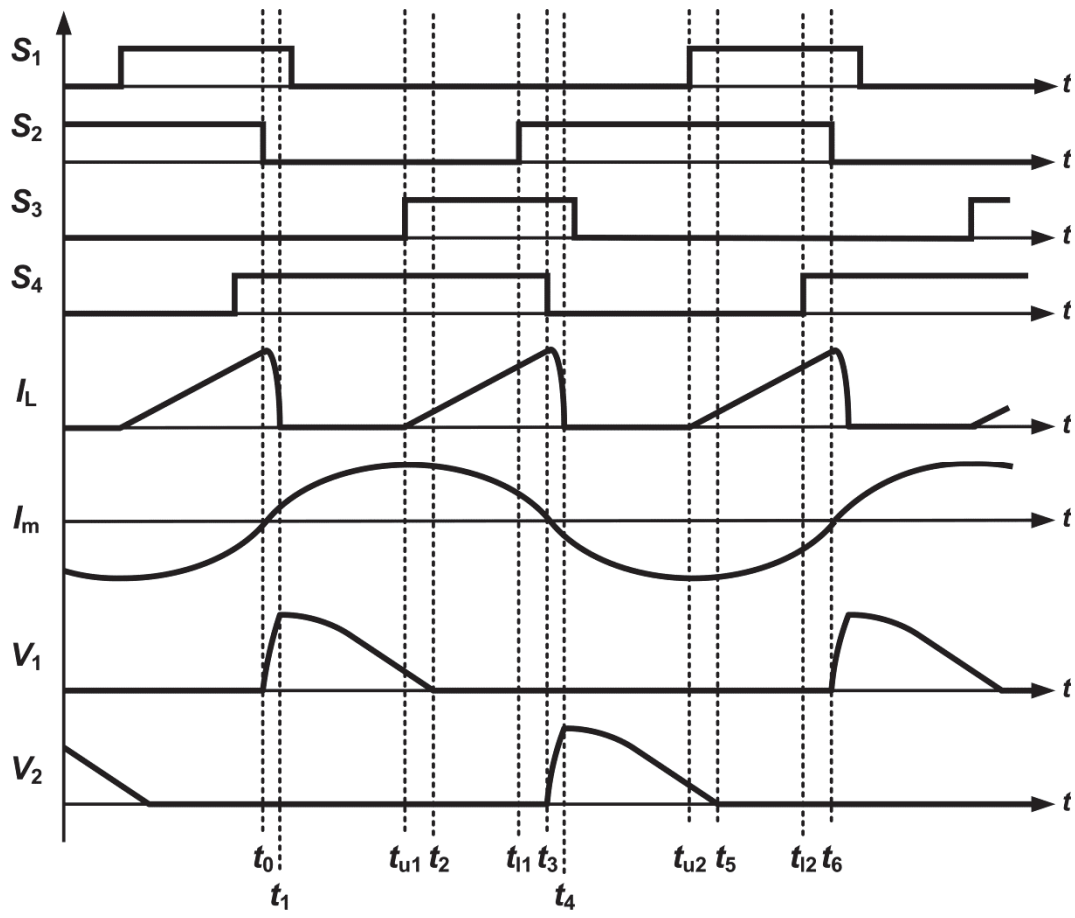
Fig. 6.8. Key waveforms for proposed current-fed full-bridge inverter at $f_n = 1$.
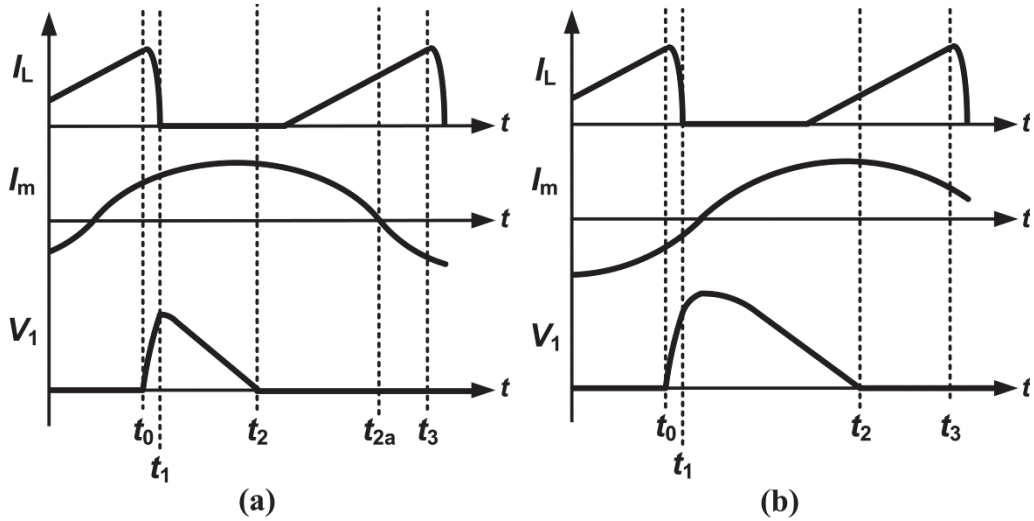
Fig. 6.9. Key waveforms at (a) $f_n < 1$. (b) $f_n > 1$.

3) Interval t_{u1}-t_2: At t = t_{u1}, the upper side switch S_3 turns on, and V_{in} magnetizes L_{in} for generating the current pulse of next half cycle. The operation is shown in Fig. 10(c). Because this operation is independent from discharging C_0, the time t_{u1} where S_3 turns on can be located within the interval t_2-t_3. The magnitude of input energy per half cycle can be determined by

$$
\begin{aligned}
E_{half\ cycle} &= \frac{1}{2}C_0 V_p{}^2 = \frac{1}{2}L_{in}I_{in,peak}{}^2 \\
&= \frac{V_{in}{}^2(t_3 - t_{u1})^2}{2L_{in}},
\end{aligned}
\tag{6.15}
$$

and the peak value of the voltage crossing the PT should be

$$
V_p = \frac{V_{in}(t_3 - t_{u1})}{\sqrt{L_{in}C_0}}.
\tag{6.16}
$$

4) Interval t_2-t_3: At t = t_2, V_1 reaches zero voltage if the operating frequency is within the ZVS frequency range derived by (6.10) and (6.11). Then, the PT is short-circuited, and I_m flows through parallel diode of S_2. If the operating frequency is not within the range that can achieve ZVS, this interval will not appear. The operation is shown in Fig. 6.10(d). The time point t_{l1} is when S_2 turns on, and S_2 will achieve ZVS if t_{l1} is within the interval t_2-t_3 at $f_n > 1$ or the interval t_2-t_{2a} at $f_n < 1$.

5) Interval t_{2a}-t_3: This interval only appears when $f_n < 1$ and the inverter operates in the ZVS frequency range. At t = t_{2a}, the current direction of I_m is reversed and I_m flows through switch S_2. The operation is shown in Fig. 6.10(e). At t = t_3, the switch S_4 turns off, and the other half period starts.
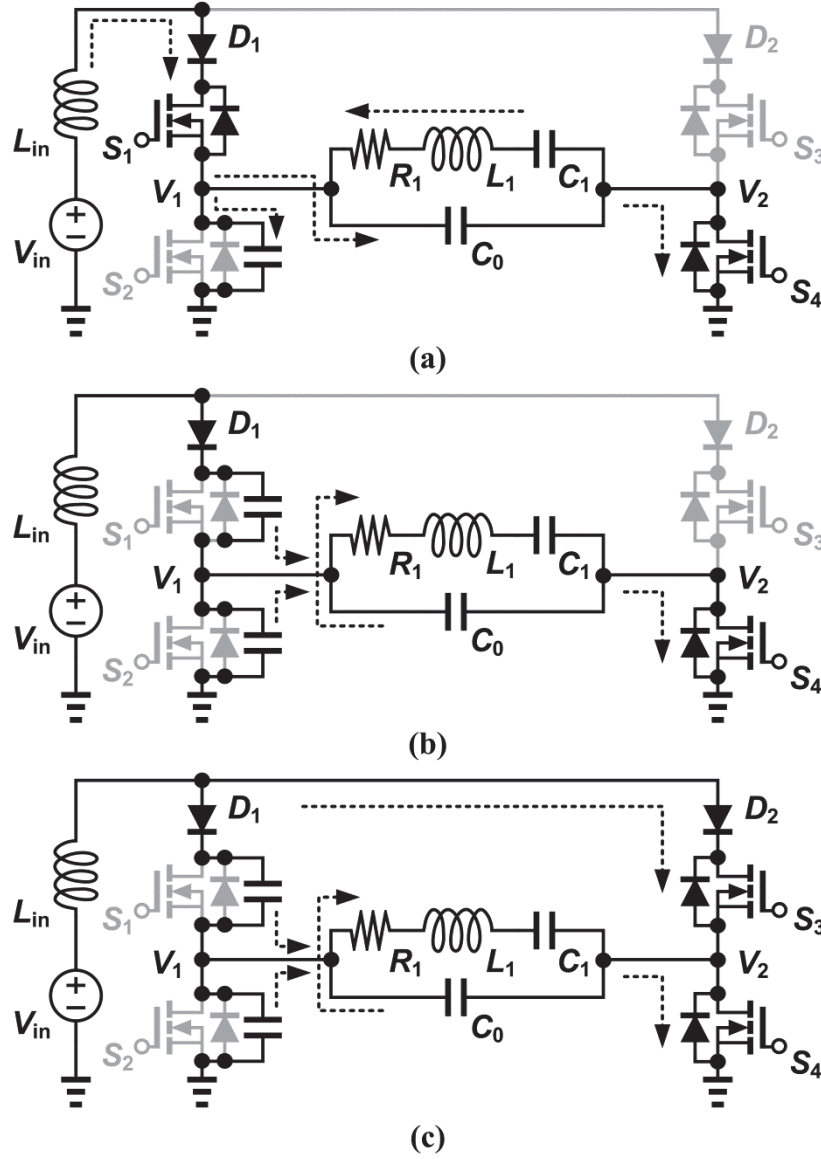
Fig. 6.10. Operations in intervals (a) t_0-t_1. (b) t_1-t_{u1}. (c) t_{u1}-t_2.

6.3.2   Tracking Strategy

The main point of the control strategy is to sweep a range of frequencies and to

detect whether the voltage V_1 decreases to zero after a current pulse is injected. If a PT,

of which the type is the same as the transmitter, is used as the receiver, operating at f_p

will have maximum gain of the receiving voltage. With the proposed control method,

(d)

(e)
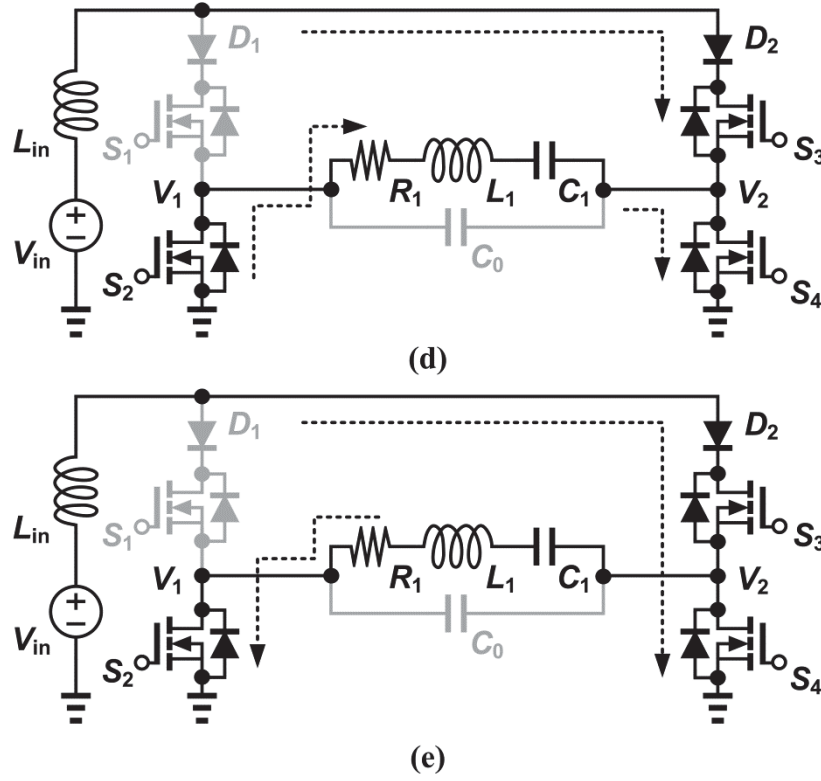
Fig. 6.10. Operations in intervals (d) t_2-t_3. (e) t_{2a}-t_3.

the ZVS frequency range is tracked, and the upper bound frequency is closer to f_p than

the lower bound frequency in this range. Thus, to get the maximum receiving voltage,

the frequency which is slightly lower than the highest frequency will be chosen as the

operating frequency.

The control flow for a microcontroller is as follows. To track the whole ZVS

frequency range, the initial operating frequency starts at a frequency which is lower than

f_p. When the converter is in steady state, whether V_1 can achieve zero voltage is

determined. If V_1 cannot achieve zero voltage, the operating frequency is increased with

a step of frequency Δf. After the first time V_1 achieves zero voltage, the frequency
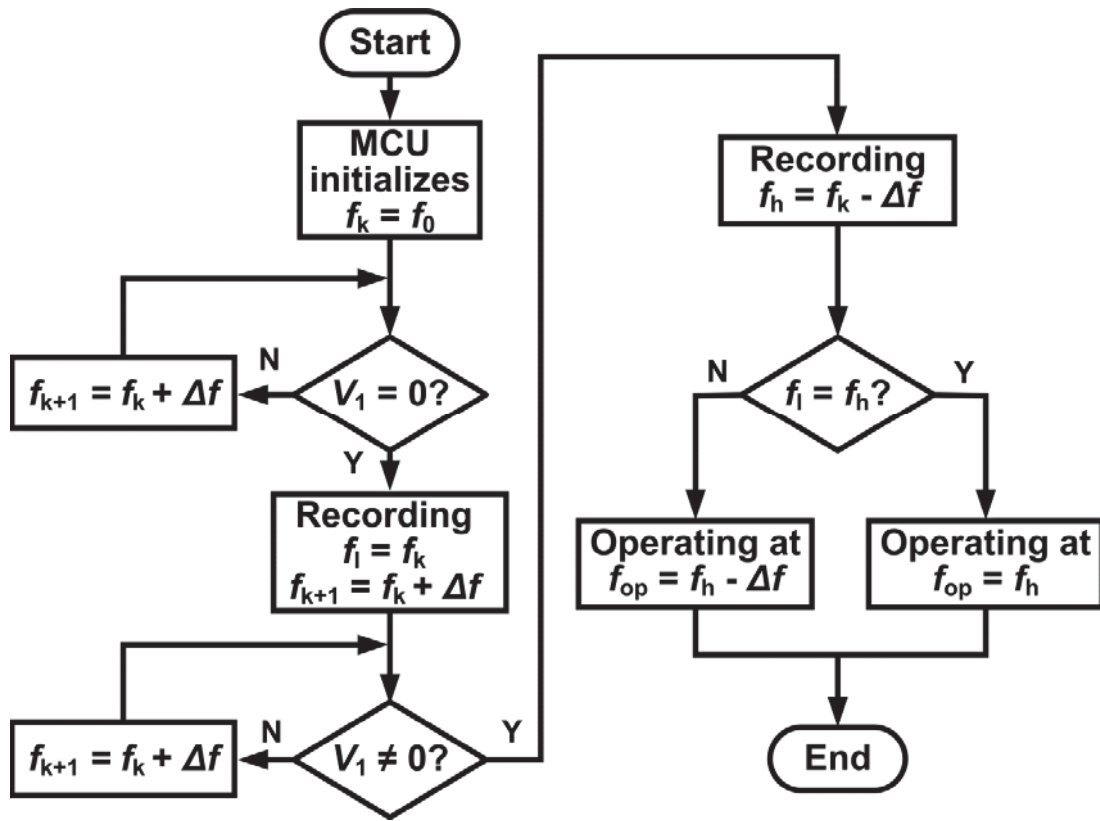
Fig. 6.11. Tracking flowchart for microcontroller (MCU).

which the inverter operates at is recorded as f_l, which is the lowest frequency where

ZVS can be achieved. The frequency increasing process continues until V_1 cannot

achieve zero voltage. Then, the previous operating frequency in the process is the

highest frequency that achieves ZVS and is recorded as f_h. Thus, the ZVS frequency

range has been tracked and the inverter can operate within it. If $f_l = f_h$, f_h will be chosen

as the operating frequency. Otherwise, the frequency which is lower than f_h with a step

of Δf is chosen. The tracking flow diagram is summarized as Fig. 6.11.
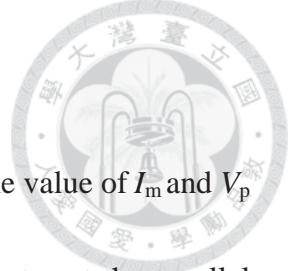
6.3.3 Power Losses Analysis

Assume that the power losses of the inverter are so small that the value of I_m and V_p could be known from (6.3) and (6.16). Moreover, the inverter operates at the parallel resonance frequency f_p. Then, the losses due to parasitic capacitances of switches and forward voltage of diodes could be

$$P_{loss,cir} = P_{loss,sd} + P_{loss,fd} + P_{loss,Cpar}$$

$$= f_p\left(\frac{V_{ds,on}}{2}\sqrt{\frac{C_0}{L_{in}}} + 2\gamma V_{df,on}I_m + C_{par}V_p^2\right)$$

(6.17)

where

$$\gamma = 1 - cos\left(2\pi f_p(t_3 - t_2)\right).$$

(6.18)

$P_{loss,sd}$ and $P_{loss,fd}$ are the conduction losses of the serial diodes and the free-wheeling diodes, respectively. $P_{loss,Cpar}$ is the turn-on losses of upper side switches. $V_{df,on}$ and $V_{ds,on}$ are forward voltage drop of the serial diodes and the free-wheeling diodes. C_{par} is the parasitic capacitances of a switch.

The transmission losses, which could only be shown from the difference between the power consumed by the transmitter and the signal power of the receiver, would be

$$P_{loss,trans} = P_{tran} - P_{rec}$$

(6.19)

where the value of P_{tran}, approximately equal to (6.2), is the actual power consumed by equivalent resistance R_1, and P_{rec} is the power of signal measured from the receiver.
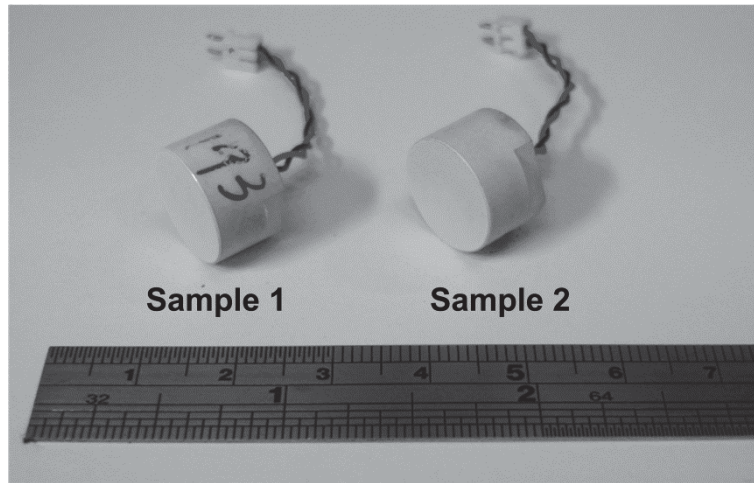
Fig. 6.12. Samples of PTs.

6.4   Experimental Results

A prototype circuit has been built to verify the frequency tracking method for a PT and the operation principle of the proposed topology. Fig. 6.12 is the photograph of PTs which are manufactured by Tung Thih Electronic Co. and are made of lead zirconium titanate (PZT). The type of those samples is the same, and they have similar characteristics. The parameters of the equivalent circuit of PTs were measured by an impedance analyzer (Agilent 4294A). The measurement results are listed in Table 6.1. Both PTs satisfied (6.9) and could apply approach proposed in this chapter to track the resonant frequency. Fig. 6.13 is the implemented circuit and the experimental setup. The topology of the implemented circuit is the same as that of Fig. 6.5. The input inductor L_{in} is designed to satisfy (6.13), and its value is 52.06 uF. The input voltage V_{in} is 24 V. The power MOSFETs S_1-S_4 are N-channel MOSFETs IRF740, and diodes connected
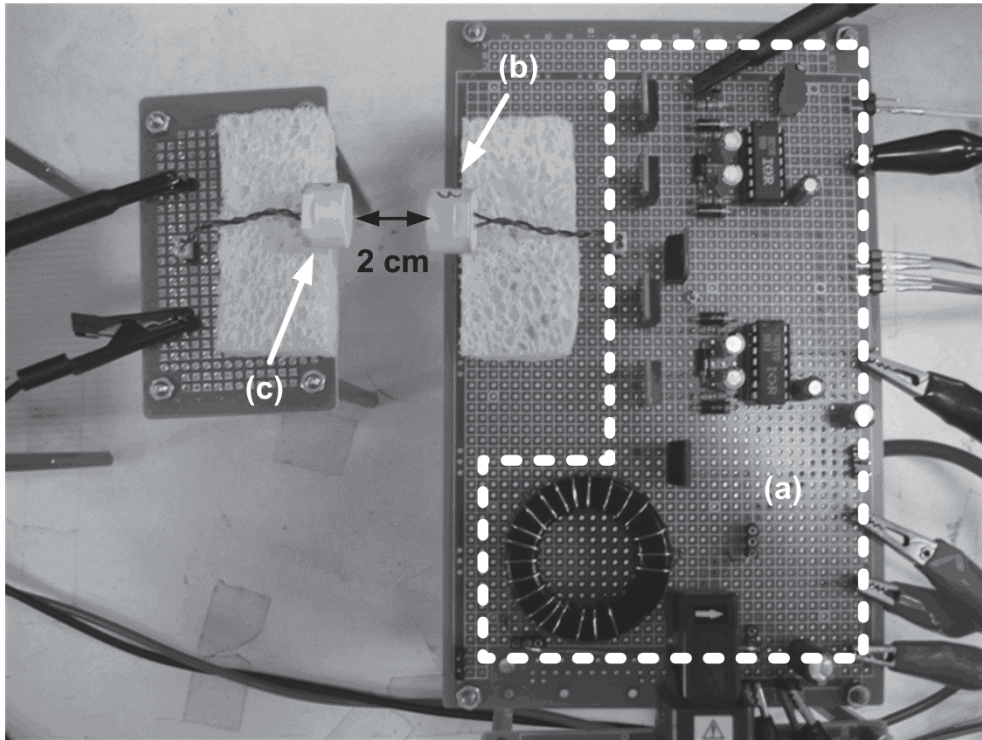
Fig. 6.13. Prototype of the proposed circuit and experimental setup. (a) Proposed

transmitting circuit. (b) The PT as a transmitter. (c) The PT as a receiver.

with upper side switches are HFA15TB60. According to the datasheet of IRF740, the

value of output capacitances is 300 pF. Therefore, the ideal specification for the

implemented circuit could be calculated and listed in Table 6.2. The microcontroller is

PIC18F4520, which is an 8-bits microcontroller manufactured by Microchip

Technology Inc. Sample 1 was used as the transmitter and sample 2 as the receiver to

measure the transmitting ultrasound. The receiving circuit was a PT directly connected

with the probe of the oscilloscope. The distance between the transmitter and the receiver

was 2 cm to get a larger receiving signal value.

Table 6.1 Specification of PTs

Parameter	Sample 1 Value	Sample 2 Value
C_0	2.406 nF	2.461 nF
R_1	646.9 Ω	828.4 Ω
L_1	74.01 mH	66.37 mH
C_1	145.0 pF	163.8 pF

Table 6.2 Ideal Specification for Transmitting Circuit

Parameter	Sample 1	Sample 1 with C_{par}
f_p	50.03 kHz	49.82 kHz
Q	35.96	35.85
I_n	0.81	0.76

The operation of frequency tracking was started where the frequency was 45 kHz, and a step of a frequency change was about 0.25 kHz for the MCU. The magnetizing time t_{mag} for the input inductor L_{in} was set to be 2 μs, and the peak value of input current pulses should be 1 A. After the inverter reached steady-state, the tracked frequency came to 49.86 kHz, which is 0.04 kHz higher than theoretical value.

Fig. 6.14 shows the waveforms of the input current I_{in}, the voltage V_1 on one side of the PT, and the gate driving signals of switches S_1 and S_2. The maximum value of I_{in} is 978 mA. After the lower side switch S_2 turned off, the inductor current charged C_0 and parasitic capacitances. Then, I_{in} decreased and V_1 increased to the maximum value, i.e., 136 V. Due to parasitic components, some ripples can be found on I_{in} and V_1
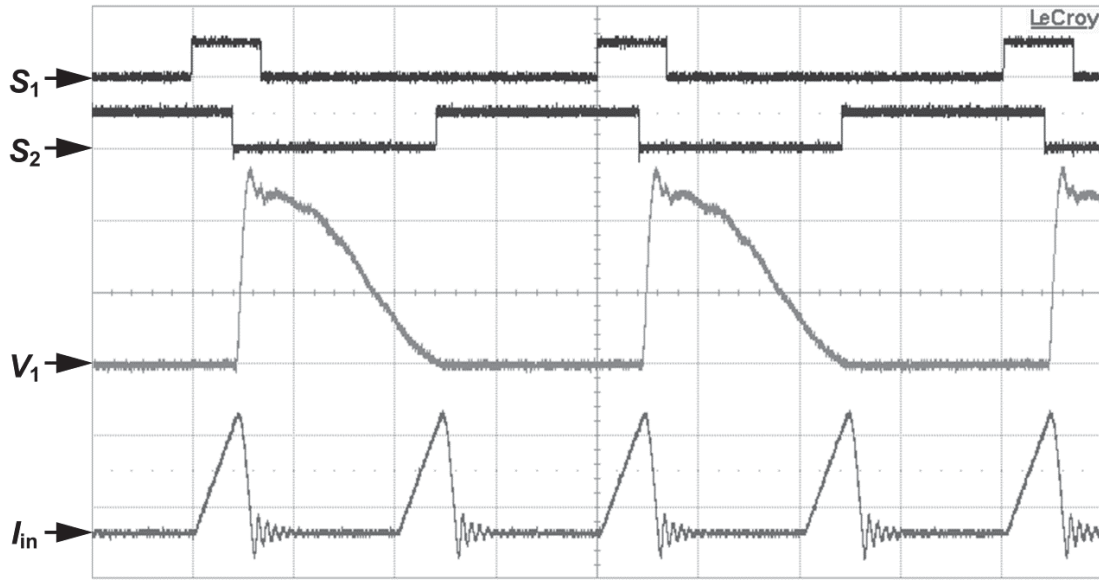
Fig. 6.14. Measured waveforms at frequency detected for $t_{mag} = 2$ μs (vertical:

S_1, 10 V/div; S_2, 10 V/div; V_1, 50V/div, I_{in}, 500 mA/div; horizontal: 5 μs/div).

waveforms after I_{in} decreased to zero. The frequency of I_{in} is twice higher than that of

other waveforms because I_{in} also charges the other side of the PT. The waveforms of the

other side S_3, S_4, and V_2 are symmetrical to the waveforms in Fig. 6.14. Additionally, the

upper side switch S_1 turned off after I_{in} decreased to zero, and the lower side switch S_2

turned on after V_1 decreased to zero. As a result, the inverter was in ZVS condition at

this frequency. Fig. 6.15 shows the waveform of receiving voltage signal. The shape of

the measured waveform is a sine wave. The frequency of the waveform is 49.86 kHz,

which is the same as the operating frequency of the inverter.

Fig. 6.16 shows the waveforms of V_1 and the receiving signal in the process of

parallel resonance frequency tracking. The converter started the process at t = t_{start}, and
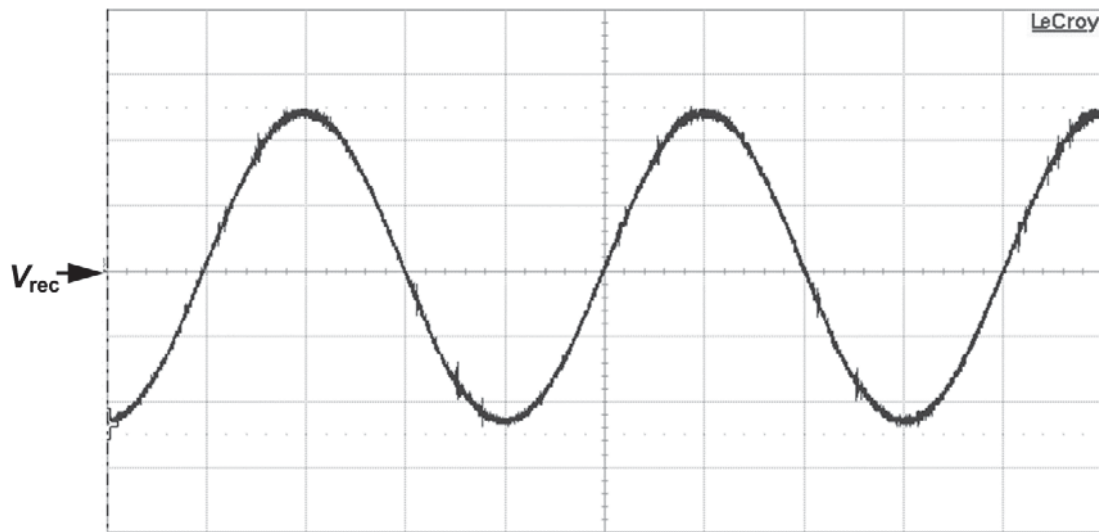
Fig. 6.15. Receiving signal waveform (vertical: 200 mV/div; horizontal: 5 μs/div).
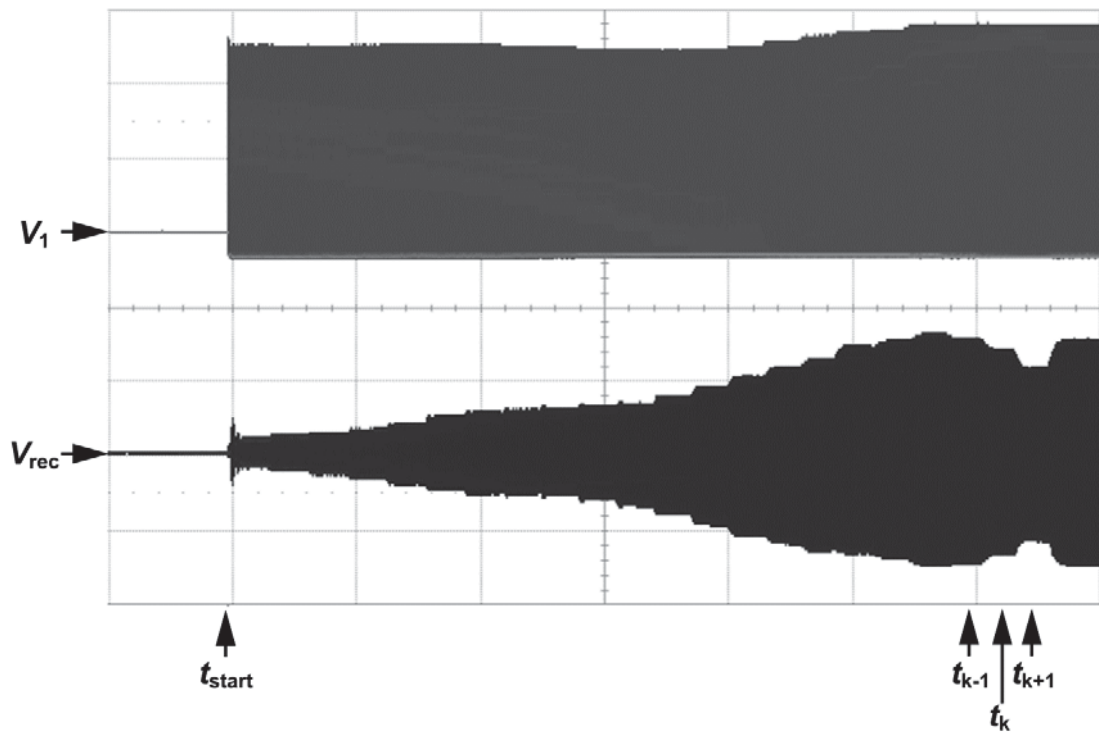
Fig. 6.16. Resonant frequency tracking waveforms (vertical: V_1, 50 V/div; V_{rec},

200 mV/div; horizontal: 5 ms/div).

the operating frequency increased. The lower side switches of the converter achieved

ZVS at t = t_k while they could not achieve ZVS at t = t_{k+1}. Thus, the resonant frequency,

which would locate near the operating frequency at t = t_{k-1}, could be determined. Then, the converter could begin to operate at the tracked frequency from the next step.

To verify the theoretical ZVS frequency range proposed in the analysis of control method and whether or not operating at the tracked frequency could result in maximum gain of receiving voltage, the receiving voltage signal was measured in different operating frequencies. Fig. 6.17 shows the waveforms at different operating frequencies. When the frequency is lower than the lower bound of the ZVS frequency range, the waveform of V_1 decreases in the beginning but cannot reduce to zero voltage. Then, V_1 increases after the direction of the mechanical current is reversed. When the frequency is higher than the upper bound of the ZVS region, the waveform of V_1 increases in the beginning and does not decrease to zero before the next current pulse. Both waveforms in Fig. 6.17 indicate the mechanical current was not large enough, and the phase angle deviation from input current pulse was too large beyond the ZVS frequency range.

An additional capacitor C_{add} was connected in parallel with the PT to verify the adaptability of the proposed method. The parallel resonance frequency would deviate from the original value due to these external parasitic components. The measured frequencies ranged from 45 kHz to 55 kHz and one step of frequency was about 0.25 kHz. The measured values of the receiving voltage are shown in Fig. 6.18, and the
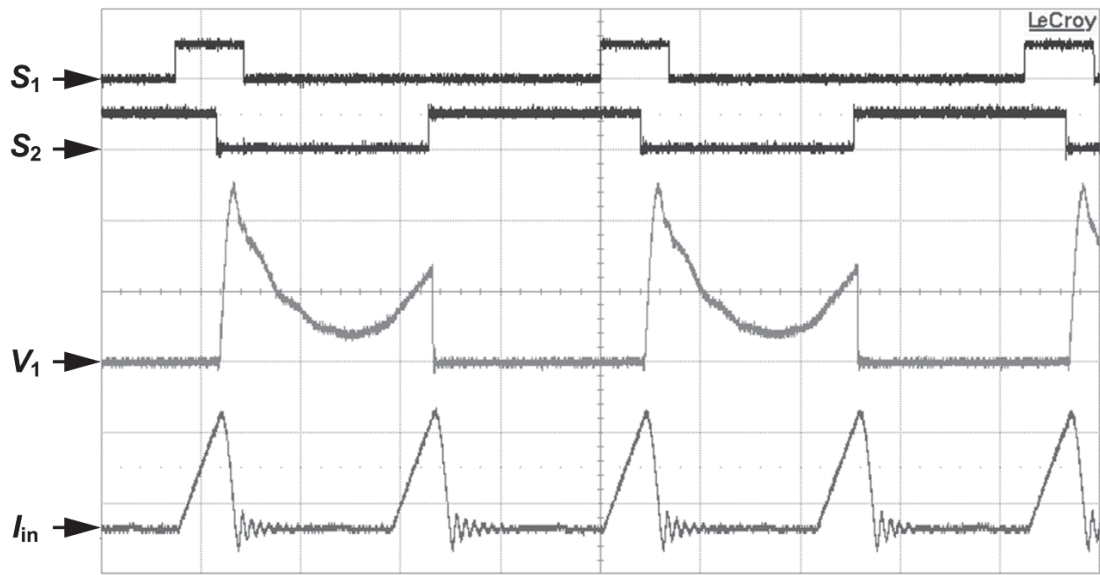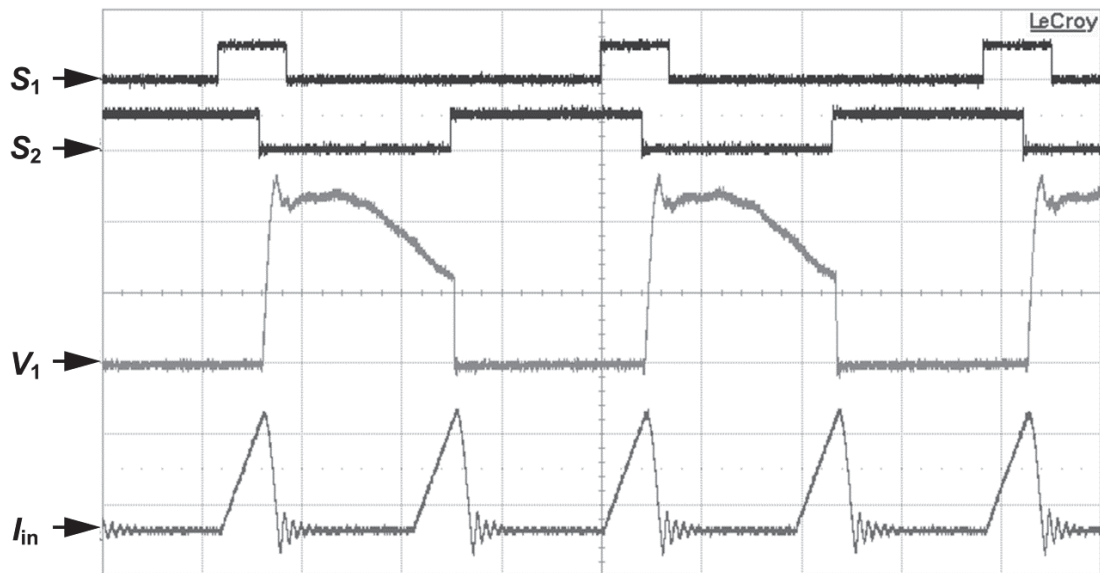
Fig. 6.17. Measured waveforms for different operating frequencies. (a) Lower than the ZVS region. (b) Higher than the ZVS region. (vertical: S_1, 10 V/div; S_2, 10 V/div; V_1, 50V/div, I_{in}, 500 mA/div; horizontal: 5 μs/div)

parameters with different values of C_{add} are listed in Table 6.3. All of experimental conditions satisfy (6.9). Because the transfer function of the receiver is also highly
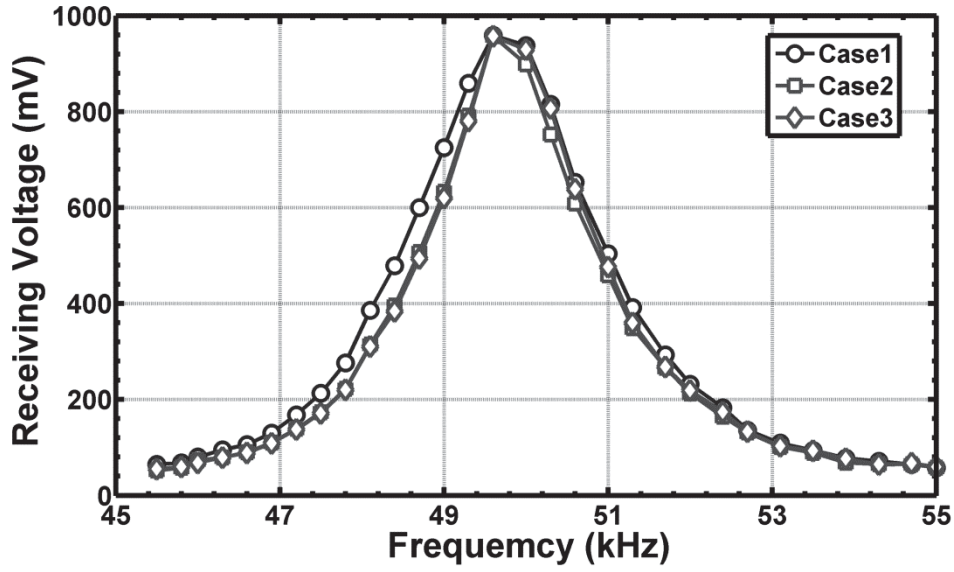
Fig. 6.18. Experimental results of operating frequency versus receiving voltage

with different additional capacitances.

Table 6.3 Parameters of PTs with Different Additional Capacitances

Parameter	Case 1	Case 2	Case 3
C_{add}	None	600 pF	1200 pF
f_p	49.82 kHz	49.64 kHz	49.48 kHz
I_n	0.76	0.69	0.64
ZVS Range	48.05 kHz - 50.30 kHz	48.37 kHz - 49.96 kHz	48.68 kHz - 49.91 kHz
$V_{rec, max}$	959 mV	957 mV	960 mV
f_{op}	49.86 kHz	49.54 kHz	49.61 kHz
$V_{rec} @ f_{op}$	938 mV	957 mV	960 mV
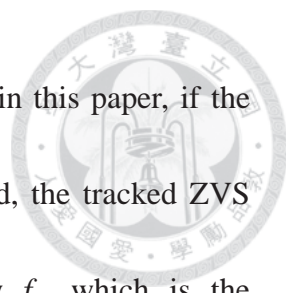
frequency-dependent, the receiving voltage curves in Fig. 6.18 do not display a

significant difference when the values of C_{add} are changed. Moreover, due to

non-ideality of the components, the ZVS range is shorter than the theoretical values.

However, it still contains the parallel resonance frequency f_p of the PT, and the upper

bound of frequency range is much closer to f_p. The magnitudes of receiving signals

which are close to lower bound of the ZVS range have a significant drop because the

sharp change of the transfer function of receiving voltage gain.

With the value of C_add increasing, ZVS ranges are shortened, which makes the

tracked operating frequencies f_op locate within 0.25 kHz from their theoretical values.

When $C_\mathrm{add} = 0$, which means the additional capacitance is not connected, the frequency

with maximum receiving voltage is 49.62 kHz, which is 0.24 kHz lower than the

frequency tracked by the proposed control method. Furthermore, the maximum

receiving voltage is 959 mV, and the receiving voltage at tracked frequency is 938 mV.

The difference between these two receiving voltages is 3% of the maximum value. On

the other hand, when $C_\mathrm{add} = 600$ pF or $C_\mathrm{add} = 1200$ pF, the frequency with maximum

gain of receiving voltage would be the same as the tracked frequency, and the values of

receiving voltage at the tracked frequency are 957 mV and 960 mV, respectively.

6.5   Summary

In this chapter, a novel resonance frequency tracking method for the PT driven

with a current-fed full-bridge inverter has been proposed. In this tracking method,

whether ZVS is achieved is used to acquire the frequency range with maximum gain of

transmitting ultrasound. Besides, according to the theory analyzed in this paper, if the boundary condition for applying this tracking method was satisfied, the tracked ZVS frequency range must include the parallel resonance frequency f_p, which is the frequency with maximum gain of receiving voltage. Hence, with the proposed control method, the PT could be operated at f_p with maximum gains of both transmitting ultrasound and receiving voltage. Additionally, by implementing soft-switch techniques in the transmitting circuit, the power loss on transistors could be reduced, which prevents heat generated on transistors.

A prototype circuit has been implemented to verify the proposed control method. The experimental results show that the tracked operating frequency is only 0.04 kHz higher than the theoretical parallel resonance frequency of the PT in the transmitting circuit without an additional capacitor. Furthermore, the proposed method could also track the theoretical resonant frequencies even with different values of additional capacitors. Thus, tracking the ZVS frequency range might be a good method to find the resonant frequency of a PT and to generate ultrasound with a light and power-efficient circuit.

Chapter 7

Realization of Active Damping Control

This chapter realizes the active damping control method for the driving circuit of a PT in a distance measurement system. Since the vibration of the PT cannot come to a halt instantly after the driving circuit stops driving it, the minimum detectable length in the system with a single PT is restricted. By applying active damping, the transition time can be reduced, and then the detectable range can be improved. Conventionally, a peak detection circuit is needed to realize the active damping control. However, with the proposed control, the phase of the vibration can be known from the driving signal, and the active damping control can be realized without any sensing circuits. The proposed control method is verified with a bi-directional flyback converter. The experimental results show that the amplitude of terminal voltage of the PT can be reduced to about one-fourth of the value with the conventional passive damping.

7.1 Analysis on the Proposed Active Damping Control Approach

7.1.1 Operation with Pulse Currents at Resonant Frequency

The pulse current is used to drive the PT and realize active damping. Because the objective of applying active damping control is to improve the decay rate when the PT

transmits ultrasound, the active damping control should be activated as soon as possible after the PT is stopped driving. Moreover, the driving circuit should have the capability to transfer energy bi-directionally, which means that the driving operation and the damping operation can be realized in the same circuit. Furthermore, the transferred energy should be discontinuous in every operating cycle, and the driving circuit should possess the capability to change the direction of energy transferring. As a result, pulses current will be an appropriate method for the energy transferring.

The synchronized electrical charge extraction (SECE) is chosen to realize the active damping control. Comparing to the energy transferring in synchronized switch damping on inductor (SSDI), the energy transferring in SECE is pulses current and is independent to the load. Thus, the driving circuit could operate at the resonant frequency of the PT, and the energy source of the driving circuit could also work as the energy reservoir in the active damping operation.

To apply the SECE technique on a PT, the timing at which the voltage crossing the PT is maximum value should be known. The voltage of C_0, which is the terminal voltage of the PT, will reach the maximum absolute value when the mechanical current I_m is zero. In conventional applications about energy harvesting and building structure damping, the vibration of the external mechanical force is irregular, which means that the phase of the mechanical current I_m is irregular, too. Thus, a peak detection circuit is

(a)   (b)
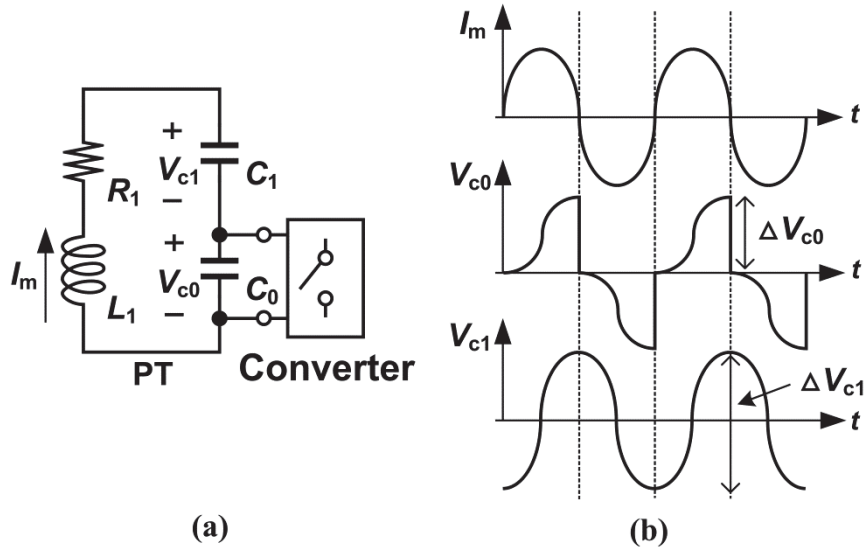
Fig. 7.1. The PT applied active damping control. (a) Configuration.

(b) Ideal waveforms.

needed in the control circuit to detect the maximum voltage crossing the PT. However, if the driving circuit could determine the phase of the mechanical current I_m and could be operated at the resonant frequency, the phase of the I_m might be predicted. This criterion can be achieved when the driving waveform is current pulse train as stated in chapter 4. Therefore, the SECE technique can be directly applied without any extra peak detection circuit.

7.1.2 Effectiveness of the Proposed Active Damping Control

The theoretical effectiveness of the SECE technique will be derived below. Assume that the PT is connected to a full-bridge rectifier, and the SECE technique is properly applied at the resonant frequency. Ignore the effectiveness of R_1, i.e. $R_1 = 0$. The

waveforms of V_{c1}, V_{c0}, and I_m are shown in Fig. 7.1 where V_{c0} and V_{c1} are respectively

the voltage of C_0 and C_1 in the equivalent circuit of a PT. When $I_m = 0$, all of the energy

in the PT would store in C_0 and C_1. Because C_0 and C_1 are serially connected, the

electrical charge Q_{charge} would store in them equally, which means

$$\frac{1}{2} Q_{charge} = C_0 \Delta V_{c0} = C_1 \Delta V_{c1} \tag{7.1}$$

where ΔV_0 and ΔV_1 are the voltage change of C_0 and C_1 in the half cycle. Then, the

voltage value of C_0 and C_1 could be known from Fig. 7.1. Because the SECE technique

discharge C_0 to zero voltage whenever the switch turned on, ΔV_0 would be the voltage

between zero and the peak value while ΔV_1 would be the one between two peak values.

Thus, when $I_m = 0$, the energy stored in capacitors could be known from

$$
\begin{aligned}
E_{C0} &= \frac{1}{2} C_0 V_{c0}{}^2 = \frac{1}{8} \frac{Q_{charge}{}^2}{C_0}, \\
E_{C1} &= \frac{1}{2} C_1 V_{c1}{}^2 = \frac{1}{32} \frac{Q_{charge}{}^2}{C_1}
\end{aligned}
\tag{7.2}
$$

where $V_0 = \Delta V_0$ and $V_1 = \Delta V_1/2$. From (7.2), after the switch turned on to transfer

energy from C_0, the amplitude of I_m in the PT would be

$$i_m[n+1] = \left(\frac{E_{C1}}{E_{C0}+E_{C1}}\right)^{\frac{1}{2}} i_m[n] = \left(\frac{C_0}{C_0+4C_1}\right)^{\frac{1}{2}} i_m[n] \tag{7.3}$$

where $i_m[n]$ is the amplitude of I_m in the n-th cycles. The change of I_m could be

represented as

$$i_m(t) = i_{peak} \left(\frac{C_0}{C_0+4C_1}\right)^{\frac{1}{2} \times 2 f_{op} \times t} = i_{peak} e^{-f_{op} \ln\left(\frac{C_0+4C_1}{C_0}\right) t}. \tag{7.4}$$

Hence, the time constant of the proposed active damping would be

$$\tau_{active} = \left[f_{op} ln(\frac{C_0 + 4C_1}{C_0}) \right]^{-1} \tag{7.5}$$

where f_{op} is the operating frequency when the SECE technique is applied on the PT.

Furthermore, if the rectifier operates in half-bridge configuration, the PT would be open-circuited when I_m is in positive half cycle and would be short-circuited when I_m is in negative half cycle. Because the value of C_1 is usually much smaller than the one of C_0, V_1 is usually much larger than V_0. The waveform of V_1 could still be seen as an ideal sine wave. The operation in half-bridge configuration could be similar to the one in full-bridge rectifier except that the energy is transferred from the PT only once per cycle. Therefore, the time constant of the active damping in half-bridge configuration could be rewritten from (7.4) and would be

$$\tau_{active,half} = \left[\frac{1}{2} f_{op} ln(\frac{C_0 + 4C_1}{C_0}) \right]^{-1} \tag{7.6}$$

The improvement of applying active damping could be seen in the reduction of the equivalent time constant of I_m. Because the phase of I_m is not influenced by the active damping control, the response of active damping is also independent from passive damping. Thus, the time constant τ_{damp} in the PT applied active damping could be known. The equivalent value of τ_{damp} is

$$\tau_{damp} = (\tau_{passive}^{-1} + \tau_{active}^{-1})^{-1} = \frac{\tau_{passive}\tau_{active}}{\tau_{passive} + \tau_{active}}. \tag{7.7}$$

7.1.3　Phase Deviation of Active Damping Control

When the driver operates at the resonant frequency, the phase of I_m can be known, and the SECE technique might be applied at a fixed operating frequency without additional peak detecting circuit. However, the resonant frequency of the PT will be different from the driving frequency when the active damping control is applied on the PT. This frequency depends on the operation of the converter which realizes the active damping control. If the operating frequency is different from the resonant frequency of the damping circuit, the phase of I_m will deviate from the phase of the operating waveform; then, the electrical charge will not be transferred when the voltage crossing the PT is of the maximum value. Therefore, the effectiveness of active damping control to improve the decay rate of I_m will be reduced.

7.2　Bi-directional Flyback Converter Topology

The topology of the bi-directional flyback converter with the equivalent circuit of the PT is illustrated in Fig. 7.2. This converter is derived from a conventional flyback converter by replacing the diode on the secondary-side with a power MOSFET [44]-[46]. With the capability of transferring energy bi-directionally, it is able to remove the DC bias on the PT in the driving operation and to realize the SECE technique in the active damping operation. Moreover, this converter operates in discontinuous
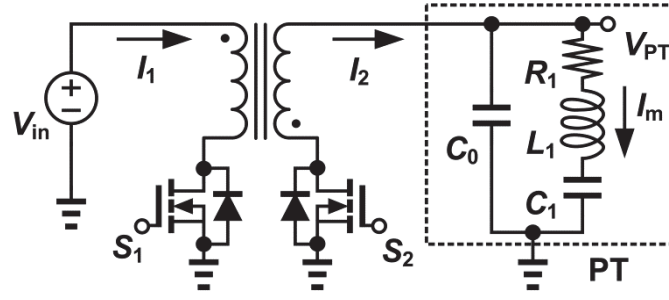
Fig. 7.2. Topology of the bi-directional flyback converter with the PT.

conduction mode (DCM). The flyback transformer can be demagnetized to zero current

after every operating cycle. Therefore, the converter can change the direction of energy

transfer in the next operating cycle, enabling it to start doing the active damping as soon

as it stops driving the PT. Furthermore, due to operating in DCM, the value of the

inductance component could be small, and the size of the flyback transformer could thus

be reduced.

The energy transfer between the flyback transformer and the PT is realized in the

form of narrow current pulses I_{pulse}. This can be achieved when the resonant frequency

between the magnetizing inductance L_{fb} of the transformer and the parallel capacitance

C_0 is much larger than the operating frequency of I_m, which means

$$f_{I_m} \ll \frac{1}{2\pi\sqrt{C_0 L_{fb}}}. \tag{7.8}$$

According to the analysis in Chapter 4, if the converter operates at the resonant

frequency of the PT, the phase of I_m will lag I_{pulse} with $\pi/2$. Moreover, because the width

of I_{pulse} is narrow, the timing at which the value of I_m is zero would locate near the one
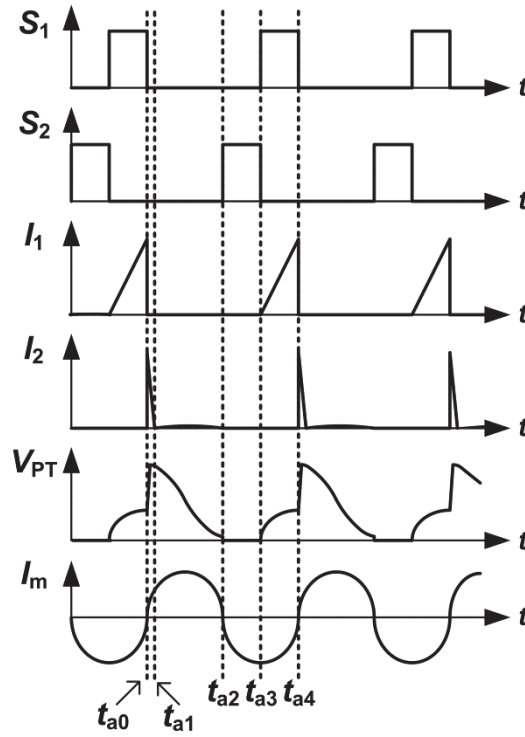
Fig. 7.3. Key waveforms in driving operation.

at which the switch turns off to demagnetize L_{fb}. Thus, the phase of I_{m} could be known

from the phase of I_{pulse}.

7.3 Operation Principles

The key operating waveforms of the converter at the resonant frequency will be

respectively shown in Fig. 7.3 for the driving operation and in Fig. 7.4 for the active

damping operation. Assume that the power switches and their free-wheeling diodes are

ideal components and that the operating frequency of the converter is the resonant

frequency. The individual operation intervals are presented as follow.
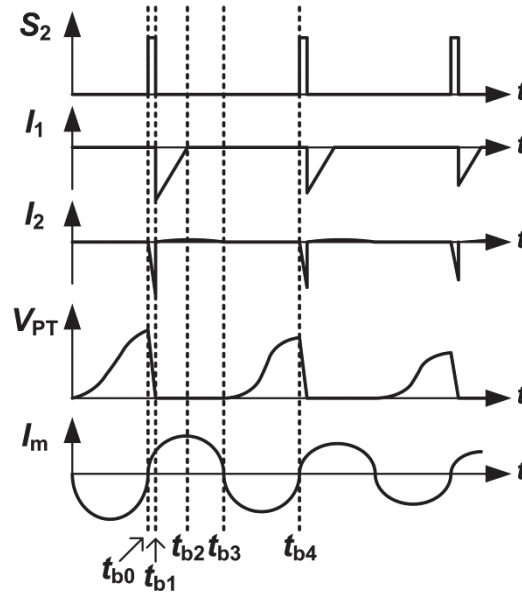
Fig. 7.4. Key waveforms in active damping operation.

7.3.1 Driving Operation

1) Interval t_{a0}-t_{a1}: The operation starts at t = t_{a0}. At this time, the primary-side switch S_1 turns off, and the magnetizing inductance L_{fb} of the transformer charges the PT from the secondary-side of the transformer. The resonance between L_{fb} and C_0 begins until the magnetizing current of L_{fb} is zero. Then, the free-wheeling diode of S_2 will turn off, and all energy stored in the flyback transformer will be transferred to the PT. Fig. 7.5(a) displays this operation. The length of the interval, and the input current waveforms could be seen as current pulse train.

2) Interval t_{a1}-t_{a2}: At t = t_{a1}, L_{fb} is fully demagnetized, and energy would only transfer between C_0 and the mechanical resonator in the PT. The operation is shown in

Fig. 7.5(b). The voltage of C_0, i.e. the terminal voltage of PT, will achieve a minimum value or will become zero at the end of this interval.

3) Interval t_{a2}-t_{a3}: At t = t_{a2}, the direction of I_m is reversed. At this time, the secondary-side switch S_2 is turned on to prevent I_m from flowing through C_0, and L_{fb} will start to resonate with the mechanical resonator. However, due to the small value of L_{fb}, most of the mechanical energy will stay in the mechanical resonator. Thus, the PT could be regarded as short-circuit in this interval. The operation is shown in Fig. 7.5(c).

4) Interval t_{a3}-t_{a4}: At t = t_{a3}, S_1 is turned on and S_2 is turned off to magnetize L_{fb} with the input source V_{in}. In this interval, I_m will flow into C_0. Hence, when the current pulse is injected in the next cycle, the terminal voltage of the PT will not rise from zero, and the PT is open-circuited in this interval. Fig. 7.5(d) shows the operation.

7.3.2 Active Damping Operation

1) Interval t_{b0}-t_{b1}: The operation starts at t = t_{b0}. At this moment, the terminal voltage of the PT reaches maximum value, and S_2 turns on to transfer energy from C_0 to L_{fb}. The operation is shown in Fig. 7.6(a). If the PT is driven at the resonant frequency, the time when the maximum voltage crossing the PT occurs can be determined without other sensing circuit after the converter stops driving the PT.
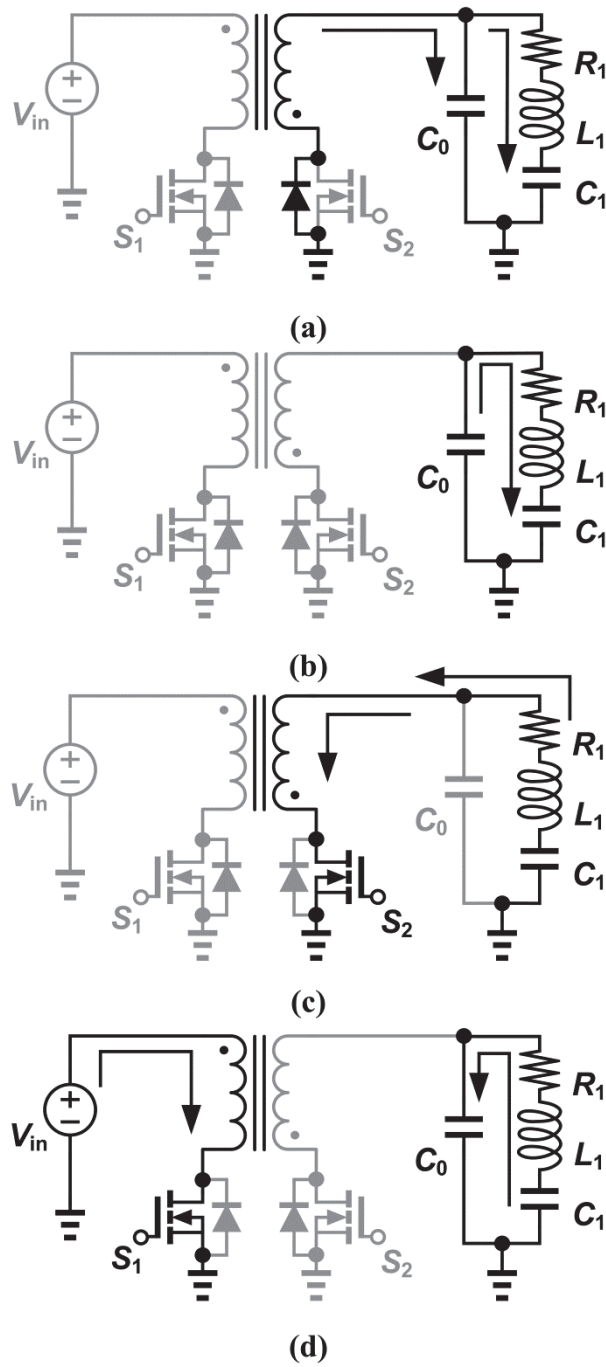
Fig. 7.5. Driving operation in interval (a) t_{a0}-t_{a1}. (b) t_{a1}-t_{a2}. (c) t_{a2}-t_{a3}. (d) t_{a3}-t_{a4}.

2) Interval t_{b1}-t_{b2}: At t = t_{b1}, the voltage of C_0 becomes zero, and the magnetizing

current of L_{fb} reaches maximum value. Then, S_2 turns off to release the energy in L_{fb} to

the input source V_{in}. Fig. 7.6(b) presents the operation. In this interval, the terminal
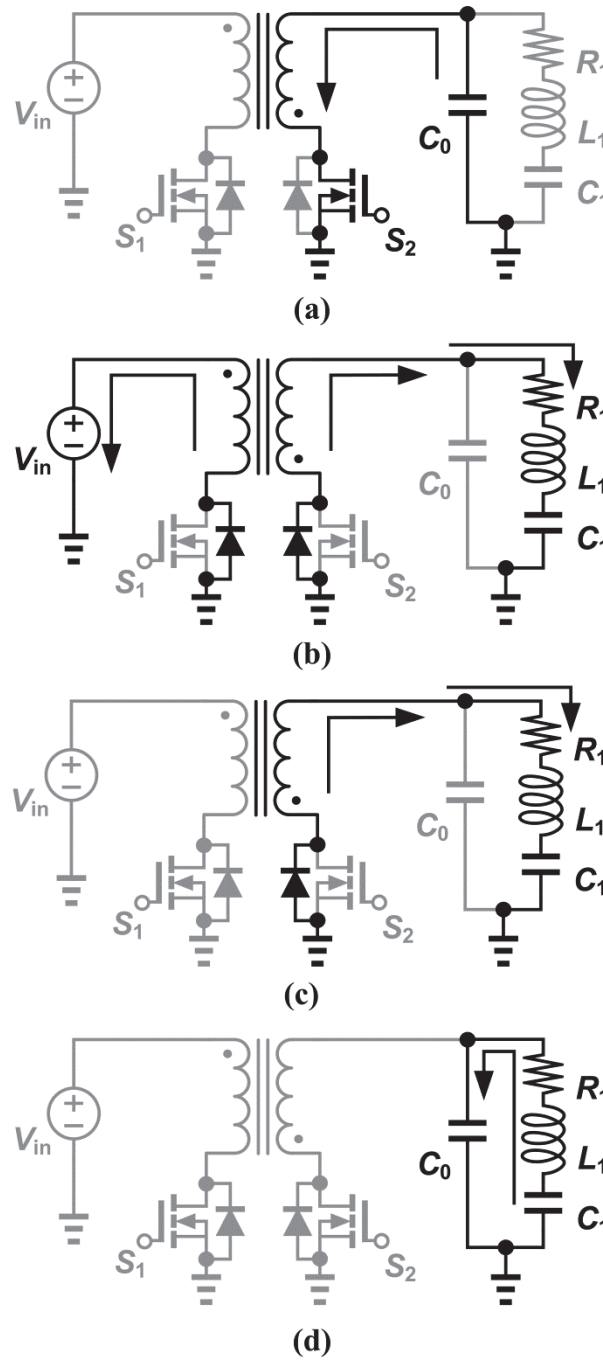
Fig. 7.6. Active damping operation in interval (a) t_{b0}-t_{b1}. (b) t_{b1}-t_{b2}. (c) t_{b2}-t_{b3}. (d) t_{b3}-t_{b4}.

voltage of the PT will be clamped at -V_{in} because the free-wheeling diode of S_2 is

conducted. Thus, the energy in the mechanical resonator would directly transfer to the

input source through the transformer.

3) Interval t_{b2}-t_{b3}: At t = t_{b2}, the magnetizing current in L_{fb} becomes zero on the primary-side. Therefore, L_{fb} will only be seen at the secondary side and will resonate with the mechanical resonator. Due to small inductance value of L_{fb}, the PT could be seen as short circuit in this interval. The operation is illustrated in Fig. 7.6(c).

4) Interval t_{b3}-t_{b4}: At t = t_{b3}, the direction of I_m is reversed, and the electrical charge flow into C_0. The voltage value of C_0 will achieve maximum value at t = t_{b4}, and then the next cycle will start. Fig. 7.6(d) shows the operation.

7.3.3   Determination of the Operating Frequency

The operating frequency should be located at the resonant frequency to prevent the waveform of I_m from deviation during the active damping operation. Then, the phase of I_m can be predicted. According to the aforementioned analysis in chapter 4, this resonant frequency can be determined by the proportion between the interval when the PT is open-circuited and the interval when the PT is short-circuited in one operating cycle. Consequently, the operating frequency in the driving operation and the active damping operation can be known from the operating waveform in Fig. 7.3 and 7.4. From Fig. 7.3, the operating frequency in the driving operation would be

$$f_{drive} = \frac{f_s f_p}{0.5(f_p + f_s) + f_p \Delta t_m (f_p - f_s)} \tag{7.9}$$

where f_s and f_p are respectively the serial resonance frequency and the parallel resonance frequency of the PT. Δt_m is the time when the flyback transformer is magnetized by the input voltage source and its value is t_{a4}-t_{a3}. On the other hand, the operating frequency in the active damping operation would be

$$f_{damp} = \frac{2f_s f_p}{f_s + f_p} \tag{7.10}$$

where f_s and f_p are respectively the serial resonance frequency and the parallel resonance frequency of the PT.

The operating frequencies in the driving operation, f_{drive}, and in the active damping operation, f_{damp} are different for this bi-directional flyback converter according to (7.9) and (7.10). The optimum operating frequency, which should be f_{drive}, detected in the driving operation cannot be directly applied in the damping operation. Therefore, both f_s and f_p should be individually tracked to calculate the values of f_{drive} and f_{damp} if the component values of the equivalent circuits in the PT are not known.

7.4 Experimental Results

To verify the proposed control method, a prototype circuit of bi-directional flyback converter was constructed. The topology of the circuit is the same as Fig. 7.2, and the implemented circuit is displayed in Fig. 7.7. The PT is manufactured by Tung Thih Electronic Co. and is made of PZT. The values of its equivalent circuits were measured
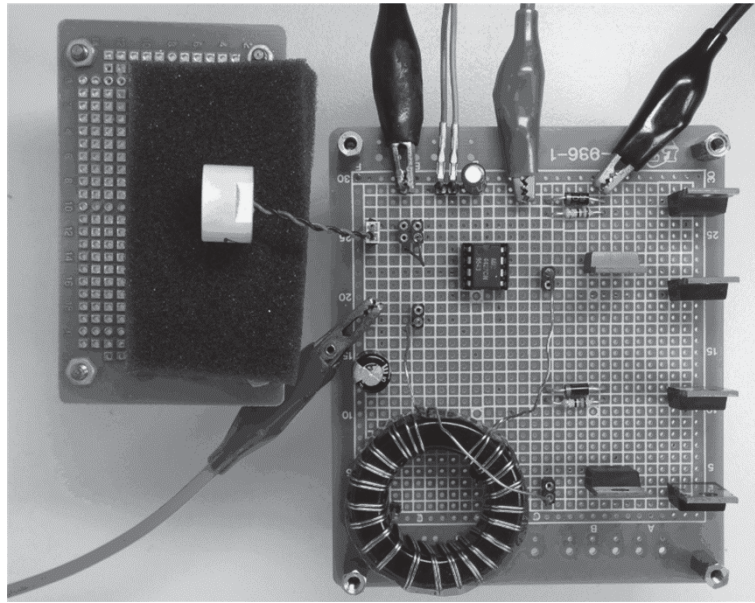
Fig. 7.7. Prototype of the implemented circuit.

Table 7.1 Specification of PT

Parameter	Value
C_0	2.46129 nF
R_1	481.759 Ω
L_1	88.8329 mH
C_1	171.113 pF
f_s	40.822 kHz
f_p	42.217 kHz

by an impedance analyzer and are listed in Table 7.1. The ratio of the flyback

transformer is one-to-one, and the value of its magnetizing inductance is 51.5 μH. This

value satisfies (7.8). Thus, the driving current of the PT can be seen as narrow pulses.

The power MOSFETs are IRF840. Because of the low turn-on speed of

the\free-wheeling diode, the MOSFETs were parallel connected with fast-recovery
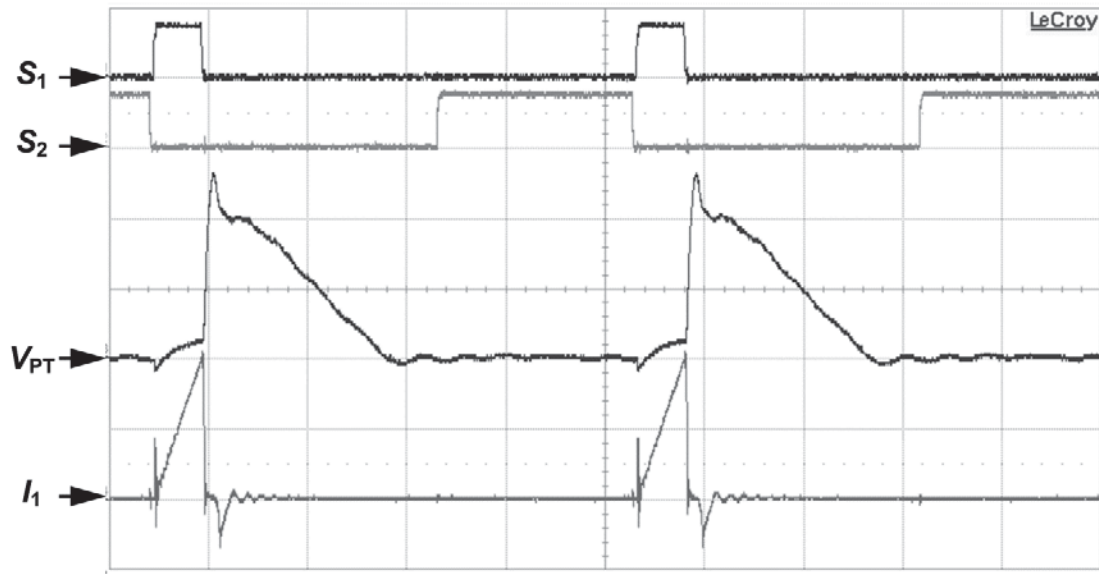
Fig. 7.8. Measured waveforms in driving operation. (vertical: S_1, 20 V/div;

S_2, 20 V/div; V_{PT}, 100 V/div, I_1, 1 A/div; horizontal: 5 μs/div)

diodes, HFA15TB60. The control PWM signals were generated by a microcontroller, PIC30F2020, which is manufactured by Microchip Technology Inc. The magnetizing time of the flyback transformer was set to be 3.75 μs to achieve large enough mechanical current. As a result, the resonant frequency of operations could be respectively derived from (7.9) and (7.10), which is 41.64 kHz in driving operation and is 41.50 kHz in active damping operation.

The waveforms in the driving operation are presented in Fig. 7.8, and the operating frequency is 41.61 kHz. A short period of dead time is added between the turn-on time of switches S_1 and S_2 to prevent input source from connecting to the PT. Moreover, after the switch S_1 turns off, a current pulse I_{pulse} is injected from the magnetizing inductance L_{fb} of the transformer, and the terminal voltage V_{PT} rises for a short period of time. Still,
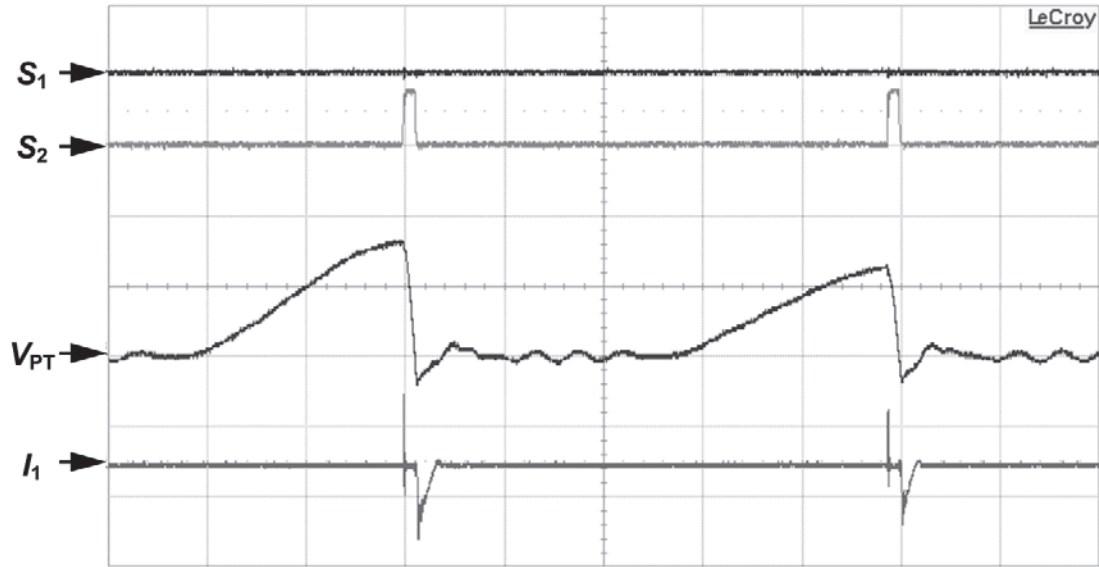
Fig. 7.9. Measured waveforms in active damping operation. (vertical: S_2, 20 V/div;

V_{PT}, 50 V/div, I_1, 500 mA/div; horizontal: 5 μs/div)

the slope of V_{PT} is zero before S_1 turns off and S_2 turns on, which means the mechanical

current I_m is zero. Therefore, the phase of I_m does lag the phase of I_{pulse} with $\pi/2$ at this

operating frequency.

The waveforms in the active damping operation are provided in Fig. 7.9, and the

operating frequency is 41.48 kHz. In this operation, S_1 remains in open-circuit, and S_2

turns on for a short period of time to transfer energy from the PT to L_{fb}. Because the PT

is driven at resonant frequency, the phase of S_2 could be determined from the phase of

S_1 in the driving operation. Thus, S_2 could be turned on at the moment when V_{PT} reaches
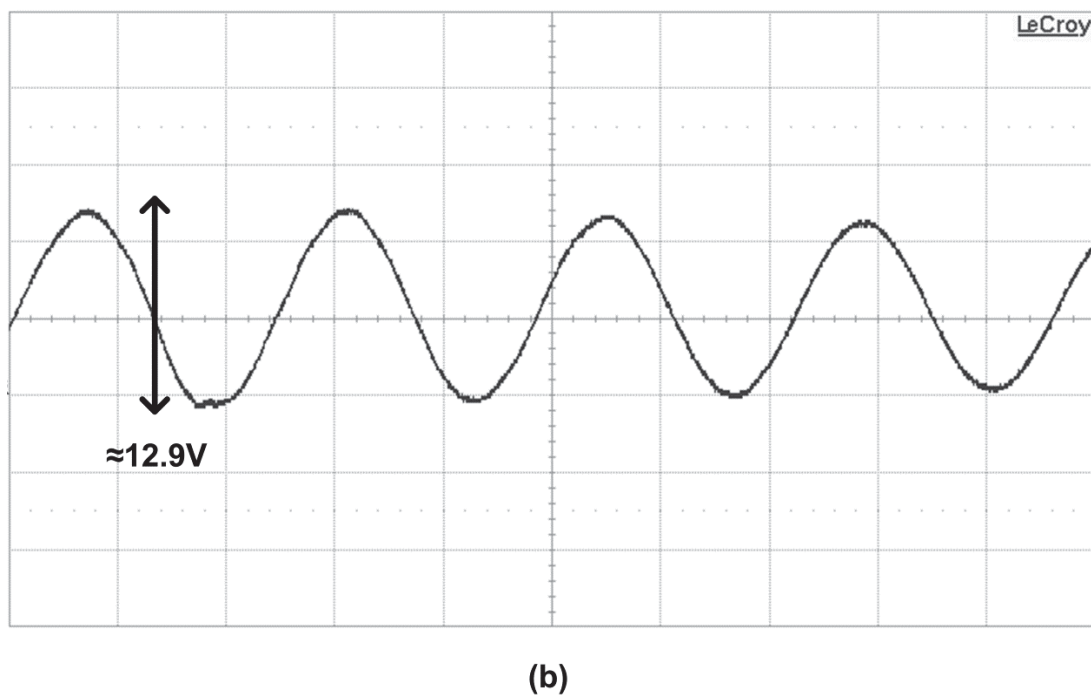
a local maximum value in the cycle.

Fig. 7.10. (a) Waveforms in transmitting operation with active damping. (vertical:

S_1, 20 V/div; S_2, 20 V/div; V_{PT}, 50V/div, I_1, 1 A/div, horizontal: 100 μs/div)

(b) Enlarged waveform of V_{PT}. (vertical: 5 V/div; horizontal: 10 μs/div)
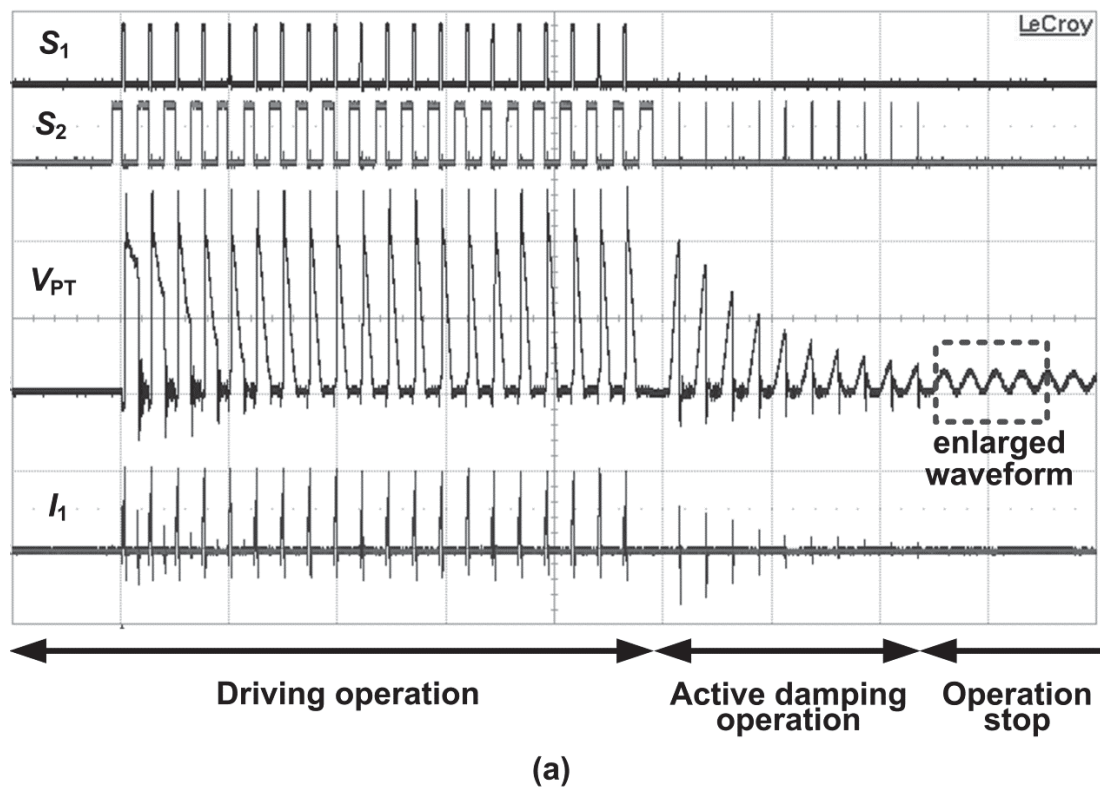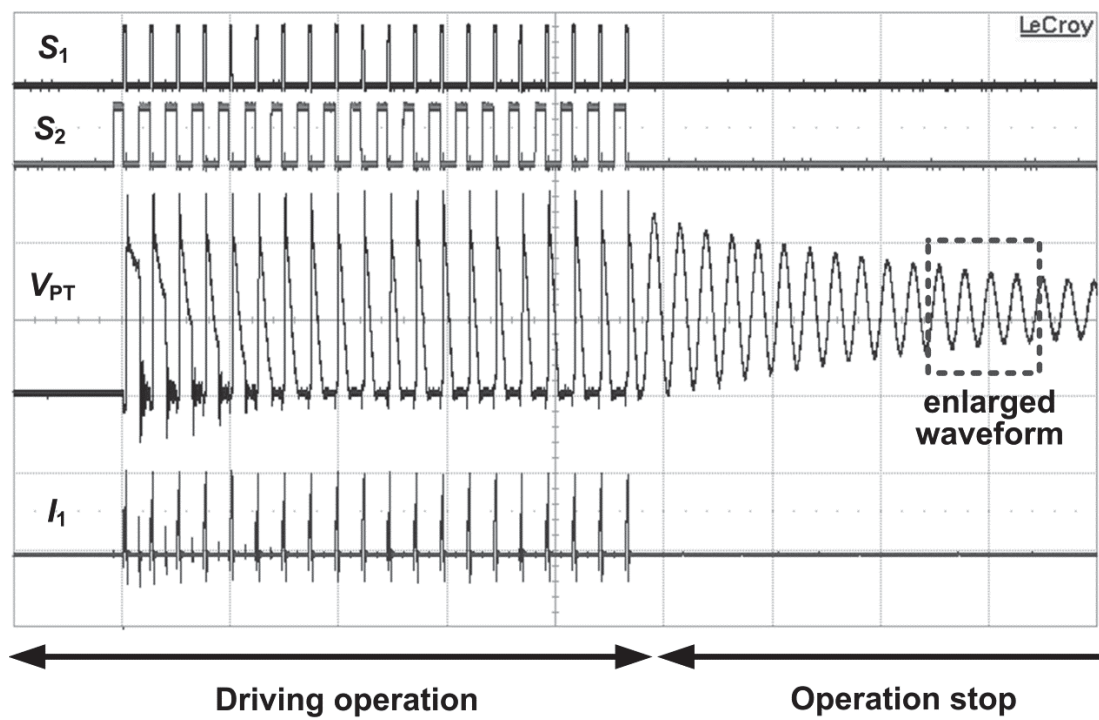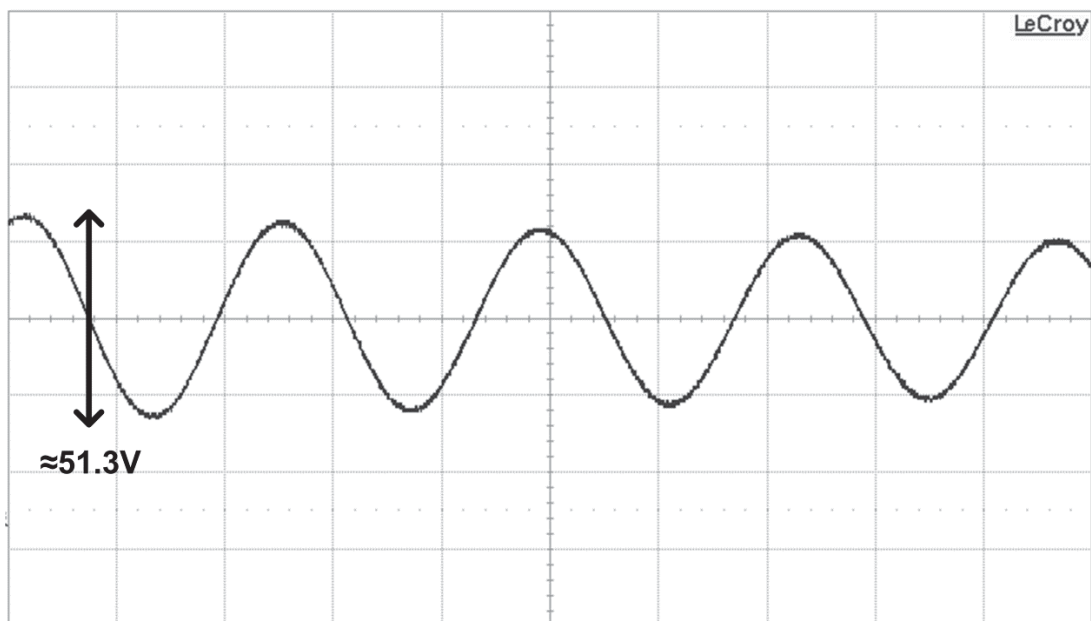
(a)

(b)

Fig. 7.11. (a) Waveforms in transmitting operation without active damping.

(vertical: S_1, 20 V/div; S_2, 20 V/div; V_{PT}, 50V/div, I_1, 1 A/div, horizontal: 100 μs/div)

(b) Enlarged waveform of V_{PT}. (vertical: 5 V/div; horizontal: 10 μs/div)

101

The waveforms of the whole operations for transmitting ultrasound are shown in Fig. 7.10 and 7.11. In Fig. 7.10(a), the operation with active damping control consists of three steps. At the beginning, the PT is driven by the converter for twenty cycles to reach its steady-state. Then, the active damping control is applied for ten cycles to accelerate the decay rate of the mechanical vibration. Finally, the converter stops operating, and the PT stayed in open-circuit. On the other hand, the operation without active damping control is shown in Fig. 7.11(a). It only consists of two steps. The converter stops operating after the first twenty cycles.

Regarding the effectiveness of the active damping control, the amplitude of V_{PT} with active damping is compared with the one with only passive damping. Fig. 7.10(a) and 7.11(a) are enlarged and are provided in Fig. 7.10(b) and 7.11(b). Fig. 7.10(b) shows the waveform of V_{PT} with active damping, and Fig. 7.11(b) shows the one without active damping. Those waveforms of V_{PT} were measured after the PT stopped being driven for a period of time, which is about 400 μs. Thus, the active damping operation had been also stopped before those waveforms were measured, and then the PT was in open-circuit in both Fig. 7.10(b) and 7.11(b). Moreover, the maximum amplitude of V_{PT} is 12.9 V in Fig. 7.10(b) and is 53.1 V in Fig. 7.11(b). The amplitude of V_{PT} without active damping is approximately threefold larger than the one with active damping.
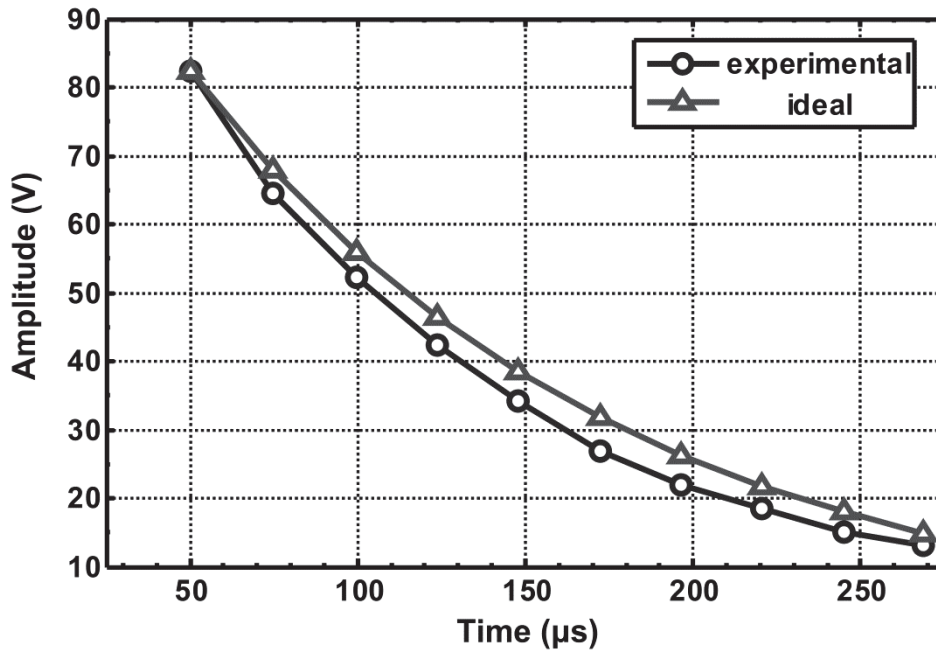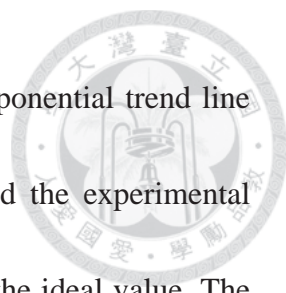
Fig. 7.12. Measured amplitude of V_{PT} with active damping control.

The measured results of the decay rate of the voltage amplitude crossing the PT are shown in Fig. 7.12 to compare with the theoretical effectiveness of applied active damping control. These data was acquired by measuring the amplitude of V_{PT} on the first cycle after the active damping operation was stopped, and the number of times for which the active damping operation was applied was set from one to ten. The effectiveness of the decay rate can be presented by the time constant of the V_{PT}. The ideal value of time constant with active damping and can be calculated by (7.6) and (7.7) from the specification displayed in Table 7.1, and the value is 128.16 μs. Still, from (3.4), the time constant without active damping is 368.86 μs, which is three time longer than the one with active damping. The experimental value of time constant can be

known by the exponential trend line of the measured data. This exponential trend line can be formed by mathematical software such like MATLAB, and the experimental value of the time constant is 117.37 µs, which is little shorter than the ideal value. The reason for why the experimental value is shorter than the ideal value may be caused by the forward voltage of the diode on the secondary-side of the converter. The mechanical current of the PT will flow through this diode for half of the operating cycle. This may contribute to additional energy loss and increasing the decay rate.

7.5   Summary

In this chapter, an active damping control method for a driving circuit of a PT has been proposed. This method is based on the SECE technique and is realized with a bi-directional flyback converter. By driving with narrow current pulses at the resonant frequency, the phase of I_m can be known. Thus, the timing at which maximum terminal voltage occurs can be predicted, and the active damping can be realized without any sensing circuit. Furthermore, the theoretical time constant for V_{PT} of the proposed active damping method has also been derived, and the effectiveness for the PT which applied active damping could be evaluated.

A bi-directional flyback converter was constructed to verify the proposed approach. The experimental results suggest that the decay rate of the vibration, which could be

presented from the terminal voltage crossing the PT, can be improved with active

damping, and the time constant of the decay rate approaches the proposed theoretical

value. Meanwhile, the amplitude of the terminal voltage reduced to approximately

one-fourth of the one without active damping. As a result, the transition time will be

shortened, and the minimum detectable length of a distance measurement system with a

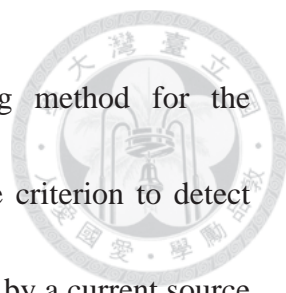single PT could be enhanced with the proposed control method.
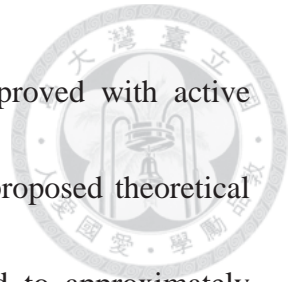
Chapter 8

Conclusions and Future Work

8.1   Dissertation Conclusions

This dissertation proposes control methods to realize active damping control on the driving circuit of the PT which is usually applied on ultrasonic distance measurement system. These control methods include how to track the serial and parallel resonance frequencies of a PT and how to determine the operating frequency of the driving circuit of the PT from its resonant frequencies. In addition, the energy is transferred between the PT and the driving circuit in the form of narrow current pulse, and thus the phase of the mechanical current in the PT can be properly predicted during the operation of transmitting an ultrasound pulse. To verify the proposed control methods, three prototype circuits were implemented in the chapter 5, chapter 6, and chapter 7.

In chapter 5, a novel frequency tracking method was proposed to detect the serial resonance frequency of the PT with a low-coupling-coefficient. By replacing the conventional sinusoidal driving voltage with square voltage waveform, the influence of the parallel capacitor of the PT can be compensated, and the phase of the mechanical current can be known. This method was verified with a half-bridge converter. The experimental results indicate that the detected frequency is about 0.4 kHz lower than the ideal value of serial resonance frequency.

Chapter 6 provided a parallel-resonance-frequency tracking method for the current-fed converter. This method used zero-voltage-switch as the criterion to detect the parallel resonance frequency of a PT. Moreover, the PT is driven by a current source instead of a conventional voltage source. As a result, the maximum transmitting gain and the maximum receiving gain of the ultrasound can locate as the same frequency of a PT. A current-fed full-bridge converter was built to confirm the proposed control methods. According to the experiments, the tracked operating frequency is 0.04 kHz away from the ideal parallel resonance frequency, and the tracked value is not highly dependent on the value of the parallel capacitor of the PT.

The proposed active damping method was realized in Chapter 7. In this chapter, the PT was driven and damped with current pulse train, and the technique about SECE was utilized. Meanwhile, the operating frequency for the driving operation and for the damping operation was determined from the configuration of the PT in one operating cycle. A bi-directional flyback converter implemented the proposed control. The experimental results showed that the amplitude of the voltage crossing the PT can decrease from 53.1 V to 12.9 V with the proposed active damping control, and the time constant for the decay rate can be improved from 368.86 μs to 117.37 μs.
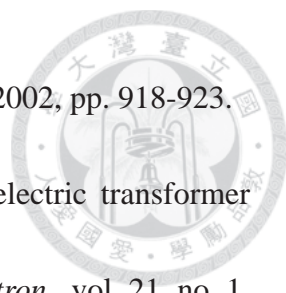
8.2　Future Work

The proposed active damping control for the PT was analyzed and verified in this dissertation. However, the proposed approaches of tracking the serial and parallel resonance frequencies were fulfilled with individual prototypes circuit. Therefore, it is worthwhile to develop a prototype circuit which can both detect these two resonant frequencies and can drive the PT with narrow current pulse. Then, the active damping control can be realized with the adaptability of environmental variation.
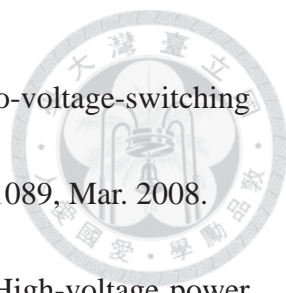
Furthermore, according to the introduction in this dissertation, a complete ultrasonic distance measurement should contain a driving circuit and a receiving circuit. The voltage level of the driving circuit may be much higher than the receiving circuit. Thus, how to connect these two circuits with a single PT would be another challenge when the PT is used as a transceiver.

REFERENCE

[1] M. H. Westbrook, "Automotive electronics," *Inst. Elect. Eng. Proc. A,*, vol. 133, no. 4, pp. 241-258, Jun. 1986.

[2] A. Chong, "The Growth of Automotive Electronics in APAC, the Next Frontier," in *Driving Asia: As Automotive Electronics Transforms a Region*, Singapore: Infineon Technologies Asia Pacific Pte Ltd, 2011.

[3] S. Nelson (2010), Automotive Market and Industry Update. [Online]. Avalible: http://www.freescale.com/files/ftf_2010/Americas/WBNR_FTF10_AUT_F0747_PDF.pdf

[4] Germany Trade & Invest (2014/2015). Industry Overview: The Automotive Electronics Industry in Germany. [Online]. Avalible: http://www.gtai.de/GTAI/Content/EN/Invest/_SharedDocs/Downloads/GTAI/Industry-overviews/industry-overview-automotive-electronics-industry-en.pdf

[5] W. J. Fleming, "Overview of automotive sensors," *IEEE Sensors J.*, vol. 1, no. 4, pp. 296-308, Dec. 2001.

[6] W. J. Fleming, "New automotive sensors-a review," *IEEE Sensors J.*, vol. 8, no. 11, pp. 1900-1921, Nov. 2008.

[7] S. Nakashima, T. Ninomiya, H. Ogasawara, and H. Kakehashi, "Piezoelectric-transformer inverter with maximum-efficiency tracking and

dimming control," in *Proc. IEEE Appl. Power Electron. Conf.*, 2002, pp. 918-923.

[8] S. Ben-Yaakov and S. Lineykin, "Maximum power of piezoelectric transformer HV converters under load variations," *IEEE Trans. Power Electron.*, vol. 21, no. 1, pp. 73-78, Jan. 2006.

[9] C.-H. Lin, Y. Lu, H.-J. Chiu, and C.-L. Ou, "Eliminating the temperature effect of piezoelectric transformer in backlight electronic ballast by applying the digital phase-locked-loop technique," *IEEE Trans. Ind. Electron.*, vol. 54, no. 2, pp. 1024-1031, Apr. 2007.

[10] W.-C. Su and C.-L. Chen, "ZVS for PT backlight inverter utilizing high-order current harmonic," *IEEE Trans. Power Electron.*, vol. 23, no. 1, pp. 4-10, Jan. 2008.

[11] Y. Mizutani, T. Suzuki, J. Ikeda, H. Yoshida, and S. Shinohara, "Frequency control of MOSFET full bridge power inverter for maximizing output power to megasonic transducer at 3 MHz," in *Proc. IEEE IAS Annu. Meeting*, 1998, vol. 3, pp. 1644-1651.

[12] S.-Y. Chen and C.-L. Chen, "ZVS considerations for a phase-lock control DC/DC converter with piezoelectric transformer," *in Proc. IEEE Ind. Electron. Conf.*, 2006, pp. 2244-2248.

[13] J. M. Alonso, C. Ordiz, and M. A. Dalla Costa, "A novel control method for

piezoelectric-transformer based power supplies assuring zero-voltage-switching operation," *IEEE Trans. Ind. Electron.*, vol. 55, no. 3, pp.1085-1089, Mar. 2008.

[14] J. Alonso, C. Ordiz, M. D. Costa, J. Ribas, and J. Cardesin, "High-voltage power supply for ozone generation based on piezoelectric transformer," *IEEE Trans. Ind. Appl.*, vol. 45, no. 4, pp. 1513-1523, Jul./Aug. 2009.

[15] H.-J. Dong, J. Wu, G.-Y. Zhang, and H.-F. Wu, "An improved phase-locked loop method for automatic resonance frequency tracking based on static capacitance broadband compensation for a high-power ultrasonic transducer," *IEEE Trans. Ultrason. Ferroelectr. Freq. Control*, vol. 59, no. 2, pp. 205-210, Feb. 2012.

[16] H.-L. Cheng, C.-A. Cheng, C.-C. Fang, and H.-C. Yen, "Single-switch high-power-factor inverter driving piezoelectric ceramic transducer for ultrasonic cleaner, " *IEEE Trans. Ind. Electron.*, vol. 58, no. 7, pp. 2898-2905, July 2011.

[17] C. Richard, D. Guyomar, D. Audigier, and H. Bassaler, "Enhanced semi passive damping using continuous switching of a piezoelectric device on an inductor," in *Proc. SPIE Smart Struct. Mater. Conf.*, *Passive Damping and Isolation*, 2000, pp. 288-299.

[18] A. Badel, G. Sebald, D. Guyomar, M. Lallart, E. Lefeuvre, C. Richard, and J. Qiu, "Piezoelectric vibration control by synchronized switching on adaptive voltage sources: Towards wideband semi-active damping," *J. Acoust. Soc. Amer.*, vol. 119,

no. 5, pp. 2815-2825, 2006.

[19] E. Lefeuvre, A. Badel, L. Petit, C. Richard, and D. Guyomar, "Semipassive piezoelectric structural damping by synchronized switching on voltage sources," *J. Int. Mater. Syst. Struct.*, vol. 17, no. 8-9, pp. 653-660, May 2006.

[20] Y.-P. Liu, D. Vasic, F. Costa, W.-J. Wu, and C.-K. Lee, "Velocity-controlled switching piezoelectric damping based on maximum power factor tracking and work cycle observation," in *Proc. Int. Conf. on Adaptive Structures and Technol.*, 2008.

[21] D. Guyomar, A. Badel, E. Lefeuvre, and C. Richard, "Towards energy harvesting using active materials and conversion improvement by nonlinear processing," *IEEE Trans. Ultrason. Ferroelectr. Freq. Control*, vol. 52, no. 4, pp. 584-595, 2005.
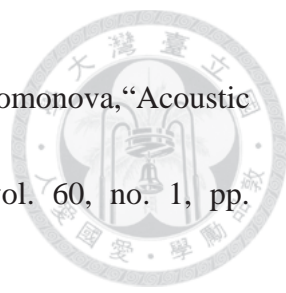
[22] Y. K. Tan, J. Y. Lee, and S. K. Panda, "Maximize piezoelectric energy harvesting using synchronous charge extraction technique for powering autonomous wireless transmitter," in *Proc. Int. Conf. Sustainable Energy Technol.*, 2008, pp. 1123-1128.

[23] M. Lallart, L. Garbuio, L. Petit, C. Richard, and D. Guyomar, "Double synchronized switch harvesting (DSSH): A new energy harvesting scheme for efficient energy extraction," *IEEE Trans. Ultrason. Ferroelectr. Freq. Control*, vol. 55, no. 10, pp. 2119-2131, Oct. 2008.

[24] L. Garbuio, M. Lallart, D. Guyomar, C. Richard, and D. Audigier, "Mechanical energy harvester with ultralow threshold rectification based on SSHI nonlinear technique," *IEEE Trans. Ind. Electron.*, vol. 56, no. 4, pp. 1048-1056, Apr. 2009.

[25] S. Mehraeen, S. Jagannathan, and K. A. Corzine, "Energy harvesting from vibration with alternate scavenging circuitry and tapered cantilever beam," *IEEE Trans. Ind. Electron.*, vol. 57, no. 3, pp. 820-830, Mar. 2010.

[26] H. Shen, J. Qiu, H. Ji, K. Zhu, and M. Balsi, "Enhanced synchronized switch harvesting: A new energy harvesting scheme for efficient energy extraction," *Smart Mater. Struct.*, vol. 19, no. 11, pp. 1-14, Nov. 2010.

[27] M. Laliart, Y.-C. Wu, and D. Guyomar, "Switching delay effects on nonlinear piezoelectric energy harvesting techniques," *IEEE Trans. Ind. Electron.*, vol. 59, no. 1, pp. 464-472, Jan. 2012.

[28] G. D. Szarka, B. H. Stark, and S. G. Burrow, "Review of power conditioning for kinetic energy harvesting systems," *IEEE Trans. Power Electron.*, vol. 27, no. 2, pp. 803-815, Feb. 2012.

[29] J. Liang and W.-H. Liao, "Improved design and analysis of self-powered synchronized switch interface circuit for piezoelectric energy harvesting systems," *IEEE Trans. Ind. Electron.*, vol. 59, no. 4, pp. 1950-1960, Apr. 2012.

[30] N. Kong and D.-S. Ha, "Low-power design of a self-powered piezoelectric energy

harvesting system with maximum power point tracking," *IEEE Trans. Power Electron.*, vol.27, no.5, pp. 2298-2308, May 2012.

[31] J. Dicken, P. D. Mitcheson, I. Stoianov, and E. M. Yeatman, "Power-extraction circuits for piezoelectric energy harvesters in miniature and low-power applications," *IEEE Trans. Power Electron.*, vol. 27, no. 11, pp.4514-4529, Nov. 2012.

[32] A. Romani, M. Filippi, and M. Tartagni, "Micropower design of a fully autonomous energy harvesting circuit for arrays of piezoelectric transducers," *IEEE Trans. Power Electron.*, vol. 29, no. 2, pp.729-739, Feb. 2014.

[33] B. Ducharne, L. Garbuio, M. Lallart, D. Guyomar, G. Sebald, and J.-Y. Gauthier, "Nonlinear technique for energy exchange optimization in piezoelectric actuators," *IEEE Trans. Power Electron.*, vol. 28, no. 8, pp. 3941-3948, Aug. 2013.

[34] Ballato, "Piezoelectricity: old effect, new thrusts," *IEEE Trans. Ultrason. Ferroelectr. Freq. Control*, vol. 42, no. 5, pp. 916-926, Sep. 1995.

[35] A. Arnau, "Fundamental of piezoelectricity," in *Piezoelectric Transducers and Application*, 2nd ed., Spain: Springer-Verlag, 2008.

[36] *IEEE Standard Definitions and Methods of Measurement for Piezoelectric Vibrators*, IEEE Std. No. 177 , 1966.

[37] *IEEE Standard on Piezoelectricity*, IEEE Std. No. 176, 1987.

[38] M. G. L. Roes, J. L. Duarte, M. A. M. Hendrix, and E. A. Lomonova,"Acoustic Energy Transfer: A Review," *IEEE Trans. Ind. Electron.,* vol. 60, no. 1, pp. 242-248, Jan. 2013.

[39] M. K. Kazimierczuk and D. Czarkowski, *Resonant Power Converter*, 1st ed., Canada: John Wiley & Sons, 1995.

[40] L. Zhu, K. Wang, F. C. Lee, and J.-S. Lai, "New start-up schemes for isolated full-bridge boost converters," *IEEE Trans. Power Electron.*, vol. 18, no. 4, pp. 946-951, Jul. 2003.

[41] L. Zhu, "A Novel Soft-Commutating Isolated Boost Full-Bridge ZVS-PWM DC-DC Converter for Bidirectional High Power Applications," *IEEE Trans. Power Electron.*, vol. 21, no. 2, pp. 422-429, Mar. 2006.

[42] S. Jalbrzykowski and T. Citko, "Current-fed resonant full-bridge boost DC/AC/DC converter," *IEEE Trans. Ind. Electron.*, vol. 55, no. 3, pp. 1198-1205, Mar. 2008.

[43] U. R. Prasanna and A. K. Rathore, "Extended range ZVS active-clamped current-fed full-bridge isolated DC/DC converter for fuel cell applications: Analysis, design, and experimental results," *IEEE Trans. Ind. Electron.*, vol. 60, no.7, pp.2661-2672, Jul. 2013.

[44] H. S.-H. Chung, W.-L. Cheung, and K. S. Tang, "A ZCS bidirectional flyback DC/DC converter," *IEEE Trans. Power Electron.*, vol. 19, no. 6, pp. 1426-1434,

Nov. 2004.

[45] T. Bhattacharya, V. S. Giri, K. Mathew, and L. Umanand, "Multiphase Bidirectional Flyback Converter Topology for Hybrid Electric Vehicles," *IEEE Trans. Ind. Electron.,* vol. 56, no. 1, pp. 78-84, Jan. 2009.

[46] P. Thummala, Z. Zhang, and M. A. E. Andersen, "High voltage Bi-directional flyback converter for capacitive actuator," in *Proc. European Power Electronics Conference (EPE)*, 2013, pp. 1-10.